UNIVERSITY OF OKLAHOMA

GRADUATE COLLEGE

HIGH RESOLUTION XRF-SCHMIDT HAMMER BASED SEQUENCE AND GEOMECHANICAL STRATIGRAPHY OF THE LEONARDIAN BONE SPRING FORMATION, SHUMARD CANYON, GUADALUPE MOUNTAIN NATIONAL PARK

A THESIS

SUBMITTED TO THE GRADUATE FACULTY

in partial fulfillment of the requirements for the

Degree of

MASTER OF SCIENCE

By

ANDREW LAYDEN
Norman, Oklahoma
2020

HIGH RESOLUTION XRF-SCHMIDT HAMMER BASED SEQUENCE AND GEOMECHANICAL STRATIGRAPHY OF THE LEONARDIAN BONE SPRING FORMATION, SHUMARD CANYON, GUADALUPE MOUNTAIN NATIONAL PARK

A THESIS APPROVED FOR THE
SCHOOL OF GEOSCIENCES

BY THE COMMITTEE CONSISTING OF

Dr. John D. Pigott, Chair

Dr. Brett Carpenter

Dr. Matthew Pranter

This thesis is dedicated to my parents. Without their love and support none of this would have been possible.

Acknowledgements

There are a number of people I would like to thank, without whom the successful completion of this project would most likely still be in question. I would like to thank my family for all of their support. I would also like to thank my chair, Dr. Pigott for being there to guide me through both academic and non-academic problems I faced during this project. Without your help and support, this would not be possible, and I will be forever grateful for your help in helping me grow as a geologist and as a person. I would also like to thank Dr. Pranter and Dr. Carpenter for their advice, edits, and support.

I would also like to thank Dr. Jonena Hearst and the staff of Guadalupe Mountains National Park service for permitting me to conduct my research in the park. Additionally, I would like to thank all of my peers who helped me in the field: Travis Moreland, Travis Plemons, Matt Lynch, and Sam Berg. This project would not have been possible without their help. I will never forget our time in the field.

Table of Contents

List of Tables

List of Figures

Abstract

A high-resolution sequence and geomechanical stratigraphic investigation was conducted on one of the most prolific formations in the Delaware Basin: the Permian, Leonardian aged, shelf to proximal slope Bone Spring formation, Shumard Canyon, Guadalupe Mountain National Park. This work incorporates a detailed X-Ray Fluorescence survey with outcrop observations to analyze a 5th- order sequence, the Leonardian 5 (L5) high-frequency cycle (HFS), and establish a 6th- order sequence framework for the classic Leonardian aged Bone Spring formation of Shumard Canyon in Guadalupe Mountain National Park. This location offers access to the stratigraphically highest units of the Bone Spring Formation which represent the updip portion of these basin fed systems, which laterally grades into the up-dip Victorio Peak Formation. Two detailed outcrop sections along slope and basin sections reveal that the L5 is divided into at least nine 6th order system tracts. Depositional settings and paleoenvironments sensitive to oscillations in sea level show pronounced differences in the study area. A hierarchical cluster analysis of 25 different elements shows seven major clusters, or chemostratigraphic packages, which served a major role in the detailing of the 6th order sequences. Redox proxies were used in order to determine that the foreslope was mostly developed under oxic to suboxic environments whereas toe-of-slope and basinal sections were mostly developed under suboxic to anoxic environments. The changes in redox conditions were mainly associated with relative sea level changes and circulation access to the Panthalassa Sea by the Hovey Channel.

In addition to geochemical data, geomechanical data were recorded along the two sections using a SilverSchmidt N-type Schmidt rebound hammer by Proceq. These data provided an opportunity to compare changes in the mechanical properties of the changing lithologies.

These mechanical properties were tied to the 6th order sequences delineated with the geochemical data. This method is possible since the sedimentological changes that occurred in response to fluctuations in sea level result in varying lithologies. Using the 6th order sequence, a prediction of a unit's brittleness is possible. In general, increased siliciclastic material results in more brittle lithology owing to the higher Young's Moduli of quartz, while increased carbonate and clay can result in more ductile lithology. The TST and HST deposits identified in this study show lower overall hardness values than the LST and RST deposits. This change in mechanical properties is due to the high levels of carbonate material and lower amount of silica being transported into the basin, and results in a more ductile lithology. There are, however, higher amounts of chert present in the TST and HST deposits, which show very high hardness values and are very brittle due to the high silica content. The LST deposits identified in this study showed mid-range hardness values, owing to the increased levels of silica and decreased levels of carbonate paired with increased clay content. However, the RST deposits show the highest overall bulk hardness values, which is attributed to the increased deposition of siliciclastic silts without an increase in clay or carbonate material, resulting in more brittle lithology. The higher brittleness is paired with spikes Ni, Cu, and Zn, supporting the idea that there was an increase in organic matter rain at the time of deposition. These properties, in addition to other petrographic properties such as increased micro-porosity, make these RST deposits good sweet spots for unconventional targets.

Chapter 1: Introduction

Located in West Texas and Southeastern New Mexico, the Permian Basin is home to world-class outcrops of geologic formations that date back as early as the Ordovician. These exposures have been the site of geologic investigations for over 130 years, and continue to this day. The discovery of oil in the early 1920s by W.H. Adams added economic viability to the basin, which further sparked interest in understanding the complex geologic systems in place (Keller et al., 1980). This basin contains world-class conventional and unconventional petroleum systems which, as of 2013, have provided over 18% of U.S. total crude production. Owing to its size, complexity, and proven economic potential, there are still many active areas of investigation in order to fully understand and utilize the basin to its full potential. Today, it is one of the world's most prolific producers of oil and gas (EIA, 2014).

The Delaware Basin is the western-most sub-basin of the Permian Basin. It is the second largest of a series of northwest-southeast trending sub-basins and platforms and is famous for its large reserves of oil (Budzik, 2014). It contains many petroleum systems of interest including many major plays in the Bone Spring formation. The Leonardian aged Bone Spring Formation is one of the dominant oil and gas producing formations in the Northern Delaware Basin, with new plays still arising to this day. It can be sourced from the underlying Wolfcamp formation or be self-sourced and serves as a major source rock within the basin proper (Montgomery, 1997). Producing reservoirs from these units include up-slope carbonate debris flows derived from the Northwest Shelf Bone Spring equivalents, the Abo and Yeso Formations, updip clastic pinch-outs, and mixed clastic and carbonate basin floor deposits (Hart, 1997). The Bone Spring Formation provides at present one of the most active unconventional plays in the Permian Basin today (EIA, 2014). Therefore, optimizing the sweet spots where extractable oil occurs by preservation in anoxic environments and where it is most brittle is critical to its economic exploitation (Enderlin et al., 2011). Understanding the reason for its heterogeneity of lithology and oil occurrence owing to changes in paleo-oceanography would also greatly impact the unconventional exploration in similar basins elsewhere. Nonetheless, understanding the stratigraphy and lithologic variation of the Bone Spring and how it relates to changes in sea level are best viewed at the updip portion of the slope facies.

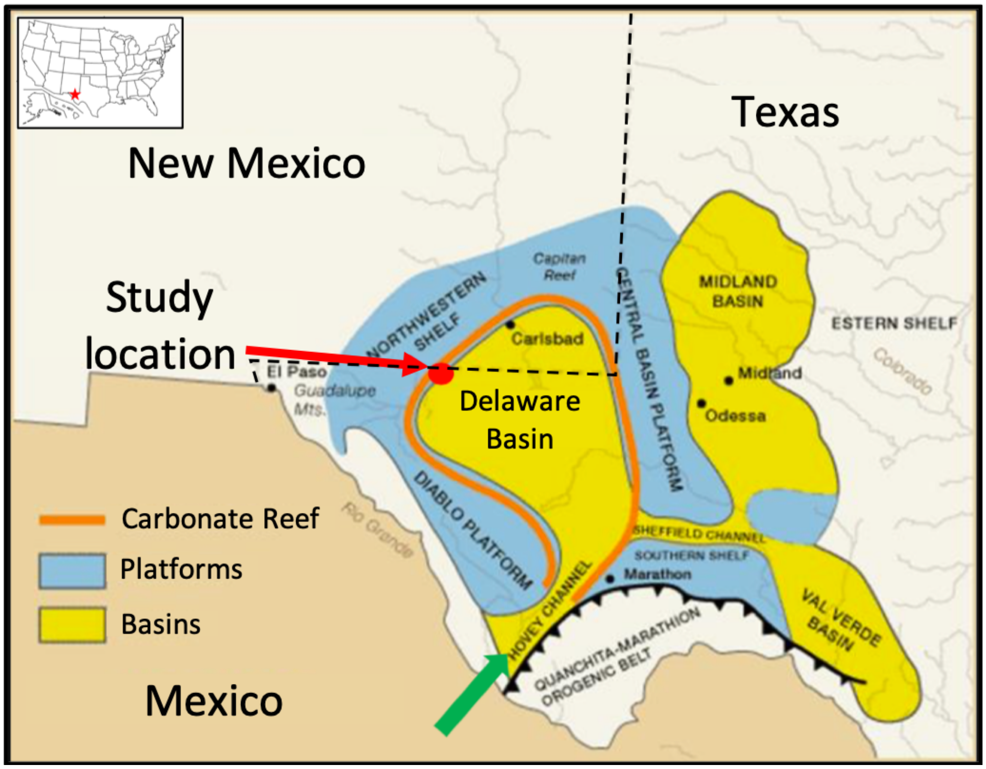

Figure 1. Map of the Permian Basin, with major sub basins and platforms highlighted. The study location in Guadalupe Mountain National Park is marked by the red dot. Edited from Murchison Oil and Gas, Inc. (2014).

1.1 Study Location

As Figure 1 shows, the Guadalupe Mountains can be found at the Northwestern border of the Delaware Basin, dividing the broad carbonate shelf margin to the North and Northwest (Northwest Shelf), and deep intracratonic basin to the South and Southeast (Delaware Basin). The western escarpment of the Guadalupe Mountains is marked by a large boundary fault and was formed by the abrupt termination of the carbonate banks by heavy erosion of the shelf edge during Cenozoic block faulting (Harris, 1987). The escarpment is over two miles wide and has a relief of up to 1000 feet. Today, it is comprised of multiple canyons exposing up-dip slope deposits of mixed lithologies such as basin margin carbonates and siliciclastic wedges of the toe-of-slope and basin (Harris, 1987).

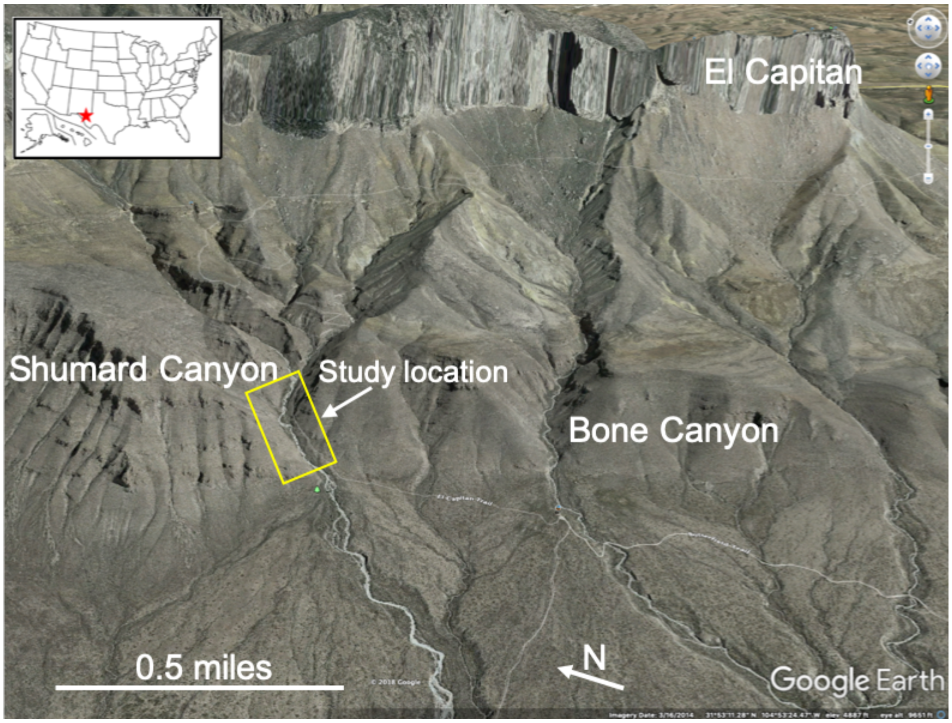

Figure 2. Map showing Shumard Canyon in relation to Bone Canyon and El Capitan. The study location can be found within the yellow box. Image taken from Google Earth.

Shumard Canyon is located in the William' Ranch area of the National Park. It has been chosen for this study as it contains the stratigraphically highest units of the Bone Spring

Formation which represents the updip portion of these basin fed systems, which laterally grades into the up-dip Victorio Peak formation. These deposits are topped by the heavily eroded Cutoff Formation and is overlain by the Brushy and Cherry Canyon Formations as shown in Figure 3 (Harris, 1987). It is stratigraphically higher than Bone Canyon and is much more accessible than Shirttail Canyon. It is for these reasons that Shumard Canyon was chosen for this study.

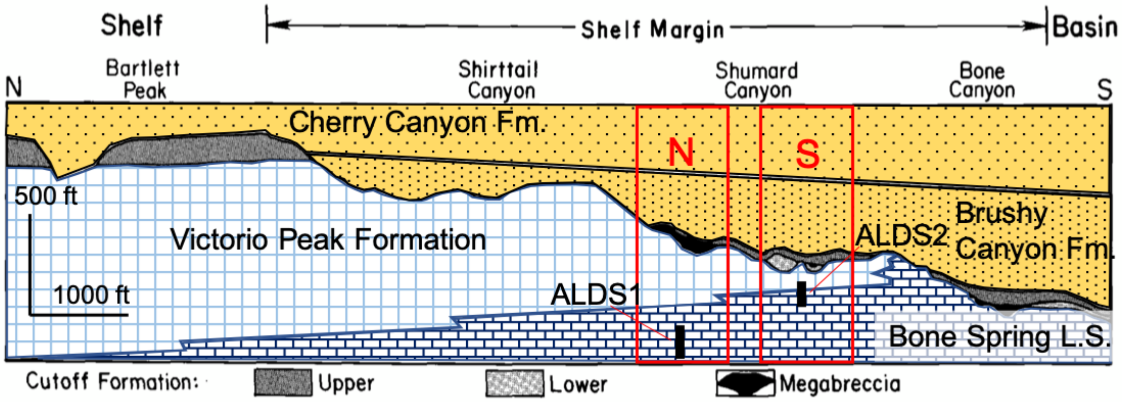

Figure 3. Stratigraphic facies relationships of the strata that make up the canyons along the western escarpment of the Guadalupe Mountains. The north and south walls of Shumard Canyon are outline by the red boxes, and include approximate stratigraphic position of the two sections in this study. Modified from Harris (2000).

1.2 Previous Work

The studies conducted previous to this work in the basin have been immensely relied upon for understanding the various stratigraphic, lithologic, depositional, and structural issues related to the target formations. The single most important foundational work conducted for understanding the Delaware Basin was led by P.B. King in 1942 and 1948. He outlines the issues and challenges of basin-wide stratigraphic divisions, facies changes, and lateral discontinuity in the basin and identifies the excessive previous attempts of naming units based on lithology alone as a hindrance (King, 1942). He later went on the subdivide the basin based on chronological evidence to form a more meaningful geologic, process-based system of units, and subdivided the

Wolfcampian, Leonardian, Guadeloupian, and Ochoan (King, 1942). However, before King, it was G.G. Shumard who first identified the Bone Spring Formation in the study area as the "black basal limestone" (King, 1948). The type location of the Bone Spring can be found in Bone Canyon, with Shumard Canyon, named after G.G. Shumard, located just a half a mile northwest (Glenister et al., 1991). P.B. King's complete analyses of these units here, and around the basin, include the Bone Spring Limestone, the Cutoff Formation, and the Victorio Peak Limestone, and are still widely used today (Hill, 1996).

Since then, many other studies have been conducted on these strata both regionally and locally in the canyon. The outcrop-based studies by Harris (1982, 1987, 2000), have attempted to shed some light on the complex Cutoff Formation in the area, and has outlined and clarified the boundaries and sequences between the Bone Spring Limestone, Victorio Peak Limestone, and the Cutoff Formation within the canyons. He proposes the further subdivisions of the Cutoff Formation in Shumard Canyon based on lithology and process sedimentology and maps each within the canyon and surrounding area (Harris, 2000). In addition to Harris, the fieldwork of McDaniel and Pray (1967) has outlined the lateral facies changes of the area from bank to margin to basin. These were mapped across the basin and multiple stratigraphic columns were created and correlated (McDaniel and Pray, 1967).

Wiggins and Harris (1985) conducted a diagenetic and geochemical analysis of the Bone Spring Formation on core extracted from the Airstrip Field, in the northeastern portion of the Delaware Basin. The study looked at shelf-derived and slope-derived dolomite bearing carbonate debris flows and dolomudstones. The dolomitization mechanisms and geochemical analyses serve as an analogous representation of what should be expected in the outcrop. Their primary findings with regard to the diagenesis showed that the dolomitization occurred almost syndepositionally, and in stages. They also infer that the high presence of organic matter in the basin bears a causative correlation to the formation of dolomite (Wiggins and Harris, 1985). In addition, they were able to correlate their geochemical analyses to other wells in the area, which shows the effectiveness of this kind of study and correlation across the field or ultimately the basin. They correlated the type II kerogen tendencies, TOC levels (on average greater than 2%), and through burial history analyses saw proper oil generation window within the Bone Spring Formation up to 200 ma and remains there today.

Other more recent studies on the formation include studies by Basset (2008) and Nance and Rowe (2015). Basset (2008) completed a thesis that analyzed chemostratigraphic packages on the uppermost Bone Spring shales and correlated them across 11 wells. The shale is closer stratigraphically to the Bone Spring Limestone and lays a framework for conducting this type of geochemical analysis using major, trace, and rare-earth elemental proxies to delineate distinct packages as well as paleoenvironmental reconstruction.

Nance and Rowe (2015) have conducted an ongoing study on the 3rd Bone Spring carbonate and sandstone/shale intervals on the core from Reeves County, Texas in the deeper, southern portion of the Delaware Basin. They use chemostratigraphic methods to analyses a mudrock rich section using X-Ray diffraction, X-Ray fluorescence, and total organic carbon to further define facies relationships with shifts in both inorganic and organic relationships with the depositional environment. This method is useful as it provides a simple yet meaningful workflow on similar rocks and depositional environments.

1.3 Problem Statement

What is the relationship between observed changes in chemostratigraphy and geomechanical properties to changes in the Leonardian sea level on the Shelf Break? This question will be addressed through the outcrop-based observations of the Bone Spring and Victorio Peak Formations in Shumard Canyon conducted through the analysis of X-Ray Fluorescence (XRF) data, Schmidt Hammer data, and thin section analyses to generate a process interpretation of Leonardian deposition as it transitions from a basinal to slope environment, and delineate sequence stratigraphic interpretations based off of said data and observations. The combination of these methods has been proven a meaningful strategy for characterizing the sweet spots where extractable oil occurs by preservation in anoxic environments and where it is most brittle (Plemons et al., 2019), which is critical to its economic exploitation. Understanding the reasons for heterogeneity of lithology and oil occurrence owing to changes in paleoceanography and the incipient process sedimentology would also greatly impact the unconventional exploration in similar basins elsewhere.

Chapter 2: Geologic Background

2.1 Geologic Evolution

The development of the Delaware Basin is closely intertwined with the development of the Permian basin as a whole. Lasting from the Precambrian to the early Mississippian, weak crustal extension accompanied by low sedimentation rates and low rates of subsidence laid the foundation for the development of the basin in a passive margin. There was primarily deposition of shallow marine carbonates and minor siliciclastic deposition (Pigott et al., 2015). This foundational deposition led to the formation of the Permian Basin's ancestral basin, the Tobosa Basin.

From the late Mississippian to the Pennsylvanian, the tectonic collision of the Hercynian Orogeny led to the development of the two sags which are now the Delaware and Midland Basins. This time was characterized by rapid sedimentation which greatly increased subsidence, which deepened the Delaware and Midland basins and elevated the Central Basin Platform by means of flexural lithospheric uplift (Pigott et al., 2016). It also altered the basin structurally by reactivating high-angle basement faults in conjunction with the formation of the Ouachita – Marathon fold belt to the south (Horak, 1985). This compression resulted in further uplift of the Central Basin Platform. (Yang and Dorobek, 1995).

Orogenic compression ceased as the basin entered the Permian. Sedimentation rates and subsidence continued to increase during this time, depositing roughly 12,000 feet of sediment (King, 1948). The Permian is generally divided into four main depositional periods: the Wolfcampian, Leonardian, Guadeloupian, and Ochoan. During the Wolfcampian, the increased clastic sedimentation and subsidence, in conjunction with global sea level rise, continually increased accommodation. However, as time went on, carbonate margins slightly restricted the basin circulation. By the late Wolfcampian, these carbonates outcompeted siliciclastic input and led to the deposition of thousands of feet of carbonate beds (Hill, 1984).

The Mid-Permian or Leonardian deposition is characterized by a further increase in sedimentation and subsidence. As they did before, carbonate shelves thrived, and in conjunction with global sea level fall, restricted basinal water circulation (Blakey, 2013). This meant that the Hovey Channel to the south was the only direct conduit from the Panthalassa Ocean to the basin at this time (Hill, 2000). It was not until the late Leonardian that tectonic uplifting to the north directly increased siliciclastic input to the basin. (Hill, 1984).

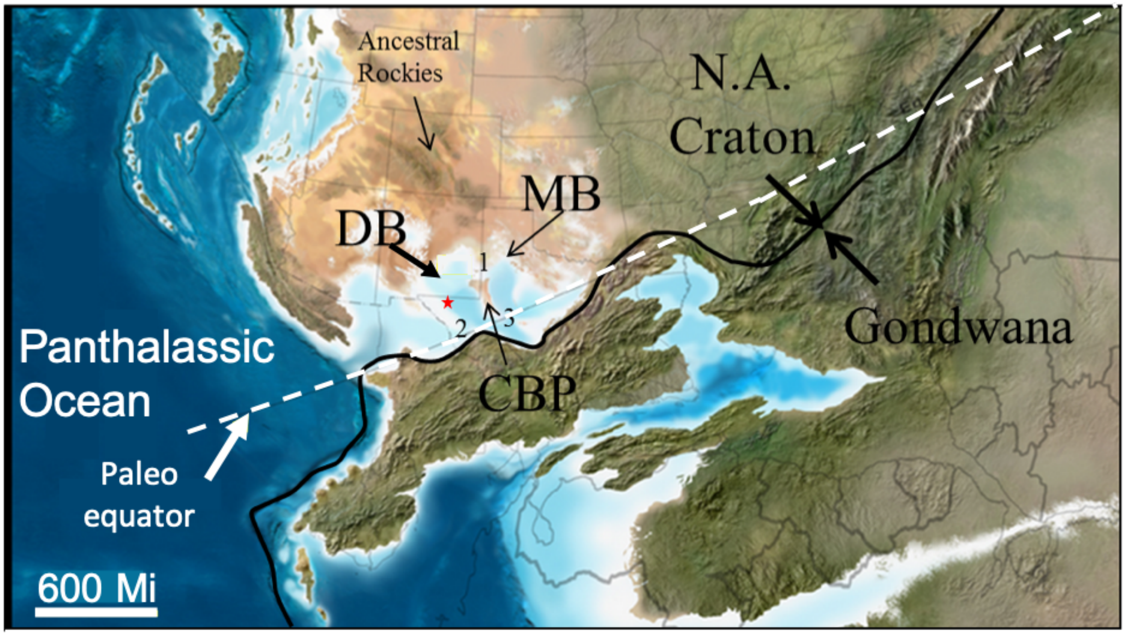

Figure 4. Paleogeography map of the Leonardian (~282-275 Ma) showing the Ouachita-Marathon (Variscan) orogenic belt (black line) between North America and Gondwana in the formation of Pangea. The approximate study area is marked by the red star. Modified after Blakey, 2013.

During the Guadeloupian, tilting toward the east and regional subsidence owing to Wolfcampian and Leonardian deposition continued (Adams, 1965). It is characterized by relatively inactive tectonics which allowed for shallow platforms and deep basinal deposits of siliciclastics up to 4000 feet thick. This depositional episode eventually slowed down, however, as the carbonate margin buildups grew and decreased sedimentation rates into the basin, which slowed subsidence rates greatly, increasing basin restriction (Mazzulo, 1981). During the Ochoan, and the conclusion of the Permian, further basinal restriction and evacuation of the basinal waters allowed over 2000 feet of evaporites to accumulate.

As the basin entered the Mesozoic, it entered a stable platform phase characterized by low mobility. It was not until the Laramide Orogeny in the late Cretaceous that the basin was uplifted above sea level, followed by basin and range tectonism and low sedimentation rates in the Cenozoic that eventually formed the modern geographic features of the Permian Basin (Hills, 1984).

2.2 Stratigraphic Setting

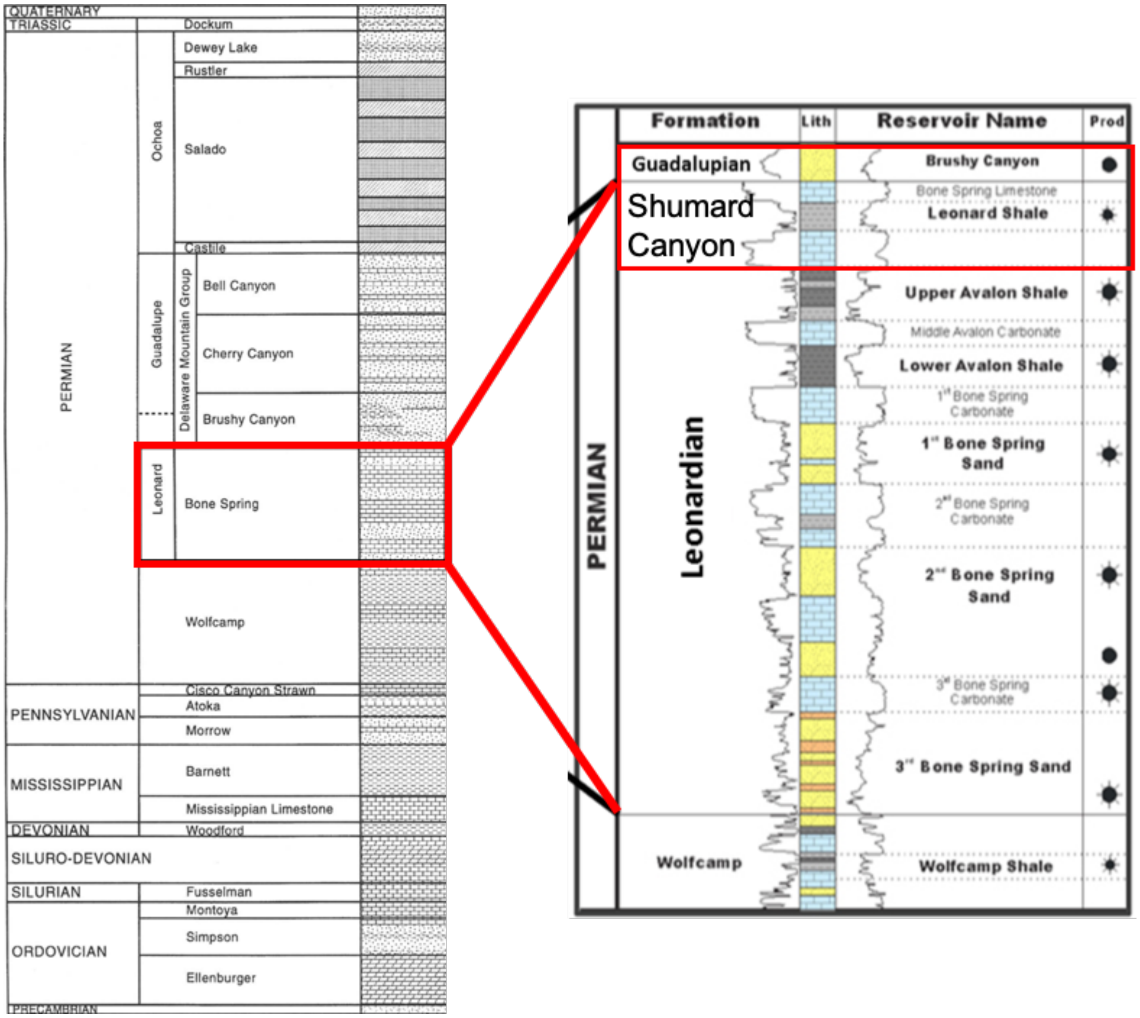

Figure 5. General stratigraphic column of the Delaware Basin. The Bone Spring Formation is highlighted in red and to the right is a more detailed stratigraphic section showing lithological variation throughout the formation. The red box in the zoomed section shows potential lithologies found in Shumard Canyon. Modified from Hardage et al., 1998 and Concho Resources via Core Laboratories, 2014.

2.2.1 Permian Deposition

Deposition during the Permian began in the early Wolfcampian times when uplifts to the northwest, west, and southwest allowed for clastic deposition into the basin (Adams, 1965). As time went on through the Wolfcampian, the pendulum between clastics and carbonates began to swing back as carbonate ramps grew and outcompeted clastic deposition (Hills, 1984). This switch led to the deposition of extensive pelagic mudstones and carbonates characteristic of the Wolfcamp formation in a nutrient-rich, partially restricted basin.

Leonardian aged Bone Spring deposition lasted from 284.8 to about 270.6 Ma and is characterized by further growth of carbonate shelf margins and the restriction of deep basinal waters (Henderson et al., 2012). It is the downdip, slope to basin formation which is stratigraphically equivalent to up-dip Abo and Yeso shelf-margin carbonates, which grade into the Victorio Peak Limestone. Shallow waters during this time remained oxygenated as the Hovey, San Simon, and Sheffield channels maintained communication to the Panthalassa Ocean (Hills, 1984), and the development of carbonate margins did not interfere with channel connectivity (Montgomery, 1998). It consists of four main couplets up to a total maximum 3,000-4,500 feet thick including the Bone Spring Limestone and Avalon Complex, the 1st Bone Spring carbonate and sandstone group, the 2nd Bone Spring carbonate and sandstone group, and the 3rd Bone Spring carbonate and sandstone group (Hart, 1997).

According to Silver and Todd (1969), the alternation between carbonate and sandstone units is the result of reciprocal sedimentation, in which the dominant lithology corresponds to sea level fluctuations. The carbonates, concentrated to the north and east, were debris flows resultant of subaqueous erosion of biota during highstand intervals. These carbonates consist of slope and detrital carbonates, allochthonous packstones, and mega breccias owing to density currents and mass wasting (Montgomery, 1998). During the lowstand intervals, carbonate growth shut down and clastic deposits dominated with the primary deposition mechanism being a submarine channel and slope to basin floor fan systems (Montgomery, 1998). These clastics consist of fine-grained sandstone and siltstone turbidites and laminated dark mudstone and siltstones (Saller et al., 1989).

The Guadeloupian is characterized by high siliciclastic input and the deposition of the Delaware Mountain Group, consisting of the Brushy, Cherry, and Bell Canyon formations. Large channel sands and toe-of-slope to slope limestone wedges dominated. (Adams, 1965). In addition to siliciclastic input, carbonate rimmed shelf margins continued their ever-increasing development. Increase wave action led to massive talus deposits, such as the famous Rader Limestone formation, and the development of forestepping reefs (Adams, 1965). Eventually, carbonate margins outgrew the basin, restricting the channels in communication with the Panthalassa Ocean, which marked the end of the Guadeloupian.

The Ochoan began by the restriction of the basin by Guadeloupian carbonate margins and sea level fall led to evaporation of basinal waters and the deposition of extensive evaporite deposits. These are known as the Castile, Salado, and Rustler Formations, and are capped by late Permian regression by the progradation of terrestrial red beds into the basin (Adams, 1965).

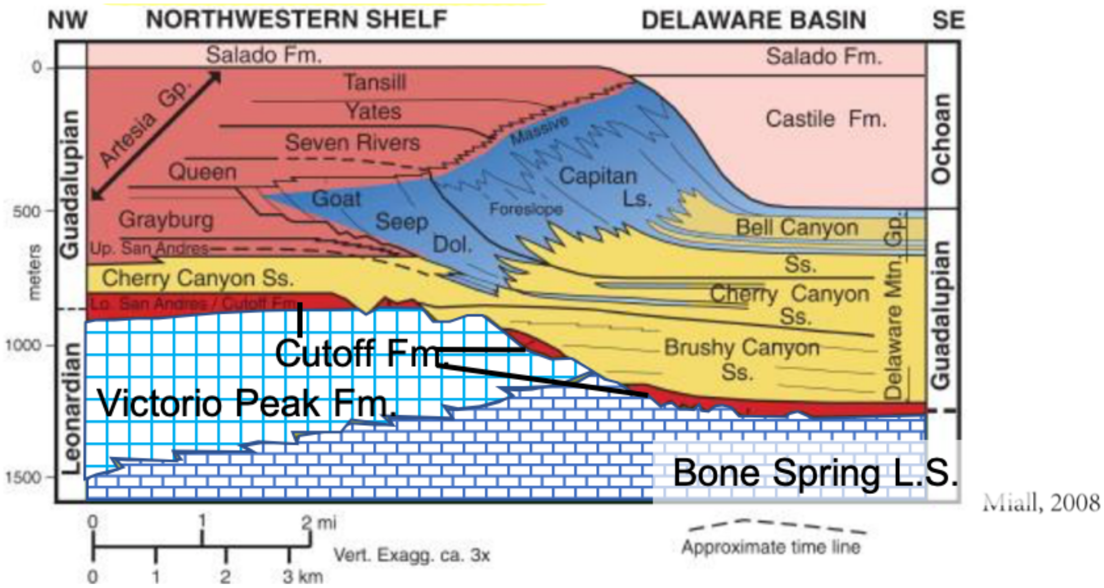

Miall, 2008

Figure 6. Stratigraphic facies relationships of the strata that make up the Delaware basin from the shelf, to slope, to basin. Modified from Miall, 2008.

Chapter 3: Methods

3.1 Field Methods

Two main stratigraphic sections were made for this study. The first stratigraphic section began near the mouth of the Canyon against the stratigraphically lower north wall, as seen in Figure 7. It is made up of four smaller measured sections, each going as far up the canyon wall as possible. The highest bed in each section was then traced along dip until contact with the creek bed, where the next section began. This technique allowed for a continuous section with no missing data, and was used again about 400 feet further into the canyon, along the stratigraphically higher south wall. The south wall section is comprised of two smaller measured sections. Each measured section contains a start and end GPS reading, detailed lithologic description, description of bed geometry, an XRF measurement, and a Schmidt Hammer measurement at every foot in the true vertical direction to the beds.

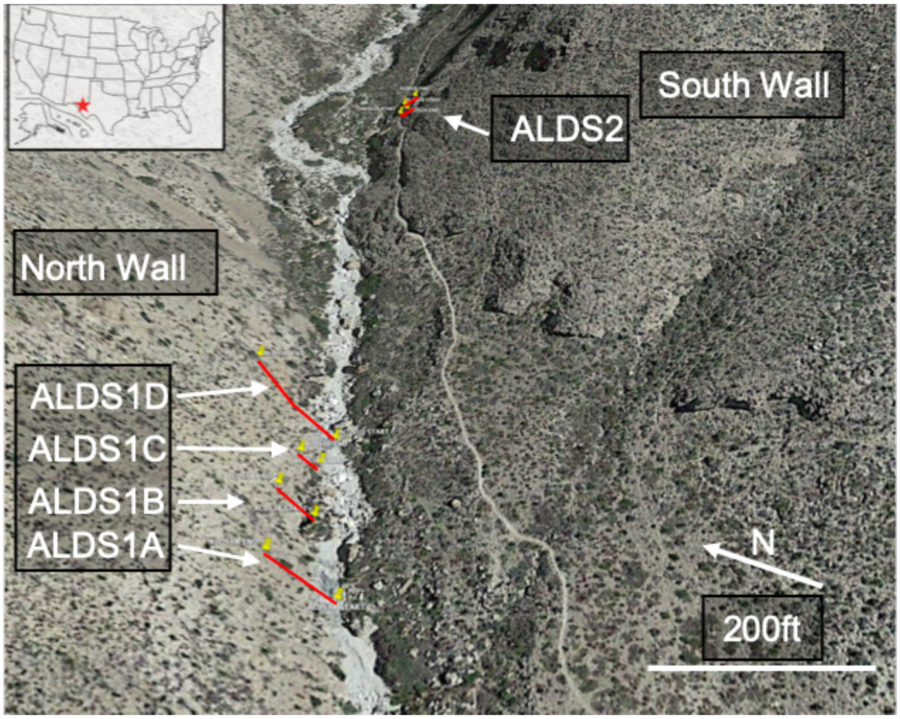

Figure 7. Map within Shumard showing measured section locations marked by the red lines and start and end points in yellow. Image taken from Google Earth.

3.1.1 Energy Dispersive X-Ray Fluorescence (XRF)

Figure 8. Niton ™ XL3t GOLDD+ XRF Analyzer by Thermo Fisher Scientific used in this study. Image from Thermo Fisher Scientific.

XRF measurements were made using a Thermo Fisher Scientific Niton XL3t GOLDD+ Analyzer, shown in Figure 8. The XRF uses high energy X-rays which are shot into the sample, knocking electrons out of their respective orbital, causing outer shell electrons to drop into a subsequently lower orbital to fill the new void. The jumping electrons release energy that is detected by the analyzer. The magnitude of energy that is released is proportional to the number of orbitals traversed by the electron. This orbital change produces a unique energy signature which can be used to calculate both the element type and abundance (Turner, 2016). The deepest the XRF can penetrate and detect elements is generally up to a couple of millimeters, and covers a surface diameter of about 8mm (Brown and Davis, 2016).

Sample preparation is very important when analyzing directly on an outcrop surface. The surface needs to be very smooth, as energy attenuation through the air can prove to be detrimental to the lightest elements, such as Si, Al, and Mg. It has been shown by Brown and Davis (2016) that just a single millimeter of relief between the analyzer and sample surface caused by roughness can cause attenuation of 3% by Si, 11% by Al, and potentially up to 20% of Mg (Brown and Davis, 2016). Since these are the lightest elements detected by the XRF, any element heavier than Si is not considered greatly at risk of attenuation around one millimeter. In order to reduce this risk, each sample location was chosen on the flattest surface possible. Then, it was sanded down first with a coarse grit, followed by fine grit sand paper, then dusted off with dusting rags.

In order to detect all desired elements, every element filter had to be activated and ran under TEST ALL GEO mode. These filters consist of the “high range” filter for detection of barium (Ba) through silver (Ag), the “main range” filter for detection of manganese (Mn) through bismuth (Bi), the “low range” for detection of titanium (Ti) through chromium (Cr), and “light range” for the detection of remaining light elements through magnesium (Mg). The filter times used for these were 30 seconds for the high, main, and low ranges and 120 seconds for the light range, bringing the total sampling time used for each measurement to 210 seconds. Each sample was recorded in parts per million (ppm) or converted to weight percent when necessary.

The results were used to create elemental profile logs and used as geochemical proxies for paleoenvironmental conditions, lithologic composition, provenance, high resolution sequence stratigraphy, and chemofacies analyses which were used for further characterizing rocks of deceptively similar characteristics in hand sample. This is a useful technique in this study area as many of the lithofacies types appear to be very similar visually, and further characterization is necessary rather than visual indicators alone.

3.1.2 Schmidt Rebound Hammer

To make in-situ measurements of rock mechanical properties, the SilverSchmidt N-type Schmidt rebound hammer by Proceq was used in this study. This device uses a spring-loaded mass attached to a plunger to send compressional waves with an impact energy of 2.207 Nm into the sample. The distance in which the plunger rebounds after contact, known as the rebound intensity, is then recorded by the device. This number is then corrected for gravitational variations internally by dividing the rebound velocity by the inbound velocity and reported as Q.

Each measurement was made on the same sanded and dusted surface used for XRF measurements, both for data quality and consistency. A total of ten measurements per data point were recorded and averaged in order in to increase the quality of measurement. Once these average Q values were obtained, they can be converted to R values, or traditional Schmidt hardness, which is just the height of the rebounded mass which is directly dependent on the hardness of the tested rock. Finally, the R values can be used in a series of empirically derived equations to calculate multiple rock mechanical attributes, such as unconfined compressive strength (UCS), Young's Modulus (E), density (ρ), and p-wave velocity (Vp). The following empirical equations were used:

$R = 1.0182*Q - 9.7625$ [Winkler and Matthews, 2014]

$E\ (GPA) = e^{(-8.967+3.091*Ln(R)}$ [Katz et al., 2000]

$UCS\ (MPA) = e^{(0.792+(0.067*R))}$ [Katz et al., 2000]

$\rho\ (kg\ m^{-3}) = -2874+1308*Ln(R)$ [Katz et al., 2000]

$Vp\ (m/s) = (2.7796+(0.0541*R))*1000$ [Altindang et al., 2005]

These values were collectively used and clustered in order to create a heat map of the hardness of the rocks in the stratigraphic column. This heat map is then used to compare the strength of the rock to the mineralogy (program provided by J.D. Pigott, personal communication, 2020), chemofacies, mineralogically derived brittleness index, and nickel (Ni), Copper (Cu), and Zinc (Zn) TOC proxies, in an attempt to identify most brittle and organic-rich sweet spots.

Chapter 4: Elemental Geochemistry

Elemental geochemistry is an important aspect of a wide variety of geological analyses. It has been proven useful to establish a chemostratigraphic framework, inferring variations in the depositional environment through geochemical proxies (Pigott et al., 2004; Pigott et al., 2005), organic paleo-productivity analysis, water column chemistry, and even mechanical interpretations (Smith and Malicse, 2010). It has also been shown to serve as an extremely valuable tool by C.F. Slatt et al. (2012) and Slatt and Rodrigues (2012) in obtaining stratigraphic control in monotonous sequences with difficult to distinguish lithologic characteristics. Apparent homogeneous sequences can be shown containing significant chemical heterogeneity, and a chemostratigraphic analysis can readily identify these heterogeneities (Nance and Rowe, 2015; Turner et al., 2015).

4.1 Elemental Proxy Analyses

Mixed source, fine-grained lithologies offer an excellent window into geologic history (Sageman and Lyons, 2004). The rocks preserved in these sedimentary realms will contain components from the terrigenous, biogenic, and authigenic inputs (Sageman and Lyons, 2004). This makes the Bone Spring Formation a prime candidate for geochemical proxy analysis, owing to its mixed origin and known sedimentary responses to relative sea level fluctuation, subsidence and tectonics, climate, sediment supply, basin physiography, environmental energy, and biota (Catuneanu et al., 2009). These sequence stratigraphic implications will prove useful and allow for sequence stratigraphic interpretation with relative lowstands represented by dominant siliciclastic intervals and relative highstand represented by dominant carbonate intervals (Nance and Rowe, 2015).

In this analysis, similar procedures as used by Crosby (2015) and Hornbuckle (2017) will be employed, as these studies were conducted in the Bone Spring and Rader Formations, respectively, which have similar transport mechanisms and lithologies as the stratigraphy in Shumard Canyon. The following elements have been selected for this study owing to their reliability as proxies and abundances as shown by Sageman and Lyons (2004), K.L Pigott et al. (2007), Parra-Galvez et al., (2009), Crosby (2015), and Hornbuckle (2017): silicon (Si), iron (Fe), titanium (Ti), zirconium (Zr), aluminum (Al), potassium (K), phosphorous (P), calcium (Ca), strontium (Sr), magnesium (Mg), manganese (Mn), molybdenum (Mo), vanadium (V), cobalt (Co), nickel (Ni), copper (Cu), thorium (Th), and uranium (U). Elements will be grouped by proxy type and used as a suite in order to reduce the risk of interpreting post-depositional overprinting such as diagenetic alterations (Sageman and Lyons, 2004), (Parra-Galvez et al., 2009) (Tuner et al., 2014).

4.1.1 Pearson Correlation Coefficient

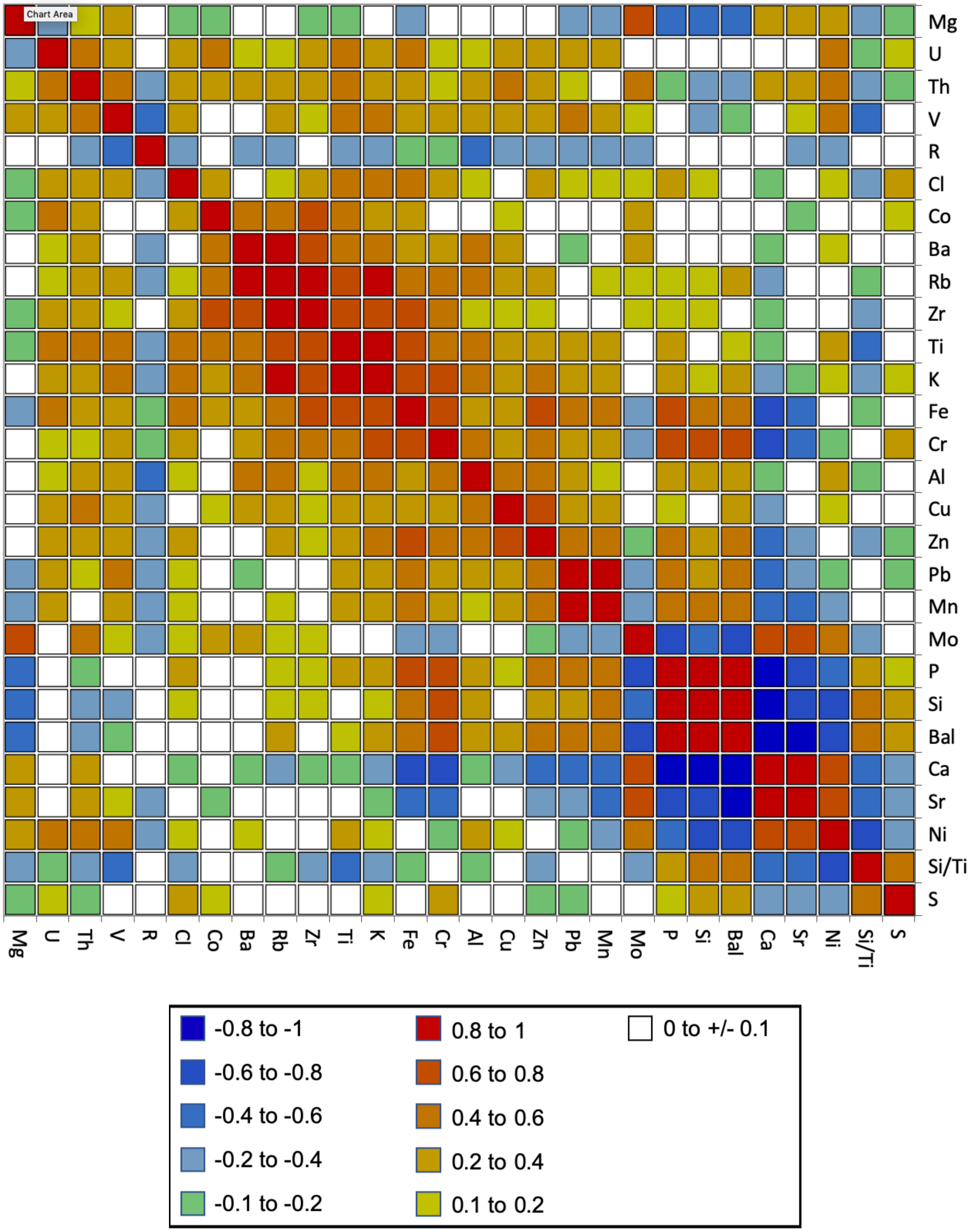

Figure 9. Pearson's Correlation Coefficients for all analyzed elements, plotted as a heat map. The cool colors represent negative correlations and the warm colors represent positive correlations, with the intensity of the colors representing the strength of the correlation. Generated with XLSTAT by Addinsoft.

A useful and necessary tool for evaluating the origin and phase of elemental proxies is to compare them to one another using and analyzing the linear relationships. The Pearson's Correlation Coefficient (r) method was applied to this study as it is a simple methodology that measures the degree of which two variables are linearly related. The coefficient, r, defines how far away the data points from a calculated line of best fit. These values will range from -1 to 1, with values closer to zero representing weak correlations and values closer to -1 or 1 representing values of strong correlation. Using the program XLSTAT, the correlation coefficients across the whole dataset were calculated and plotted in the heat map shown in Figure 9 above.

4.1.2 Terrigenous Proxies

The terrigenous proxies utilized in this study include Si, Ti, and Zr. Detrital sands and silts contain Ti and Zr, which are closely tied with continentally derived clastic processes and origin (Treaton, 2014) (Turner et al., 2015). They are also mostly immobile and diagenetically resistant, which increases their reliability as a proxy. Parra-Galvez et al., (2009) and Turner et al. (2015) interpret decreases in Ti and Zr trends as a retrogradational successions and an increase in trends as a progradational succession. Si, being the main constituent in quartz, can have both terrigenous and biogenic origins (Treaton, 2014). In order to distinguish the terrigenous fraction of Si versus Si from the biogenic source, the Si/Ti ratio will be used (Sageman and Lyons, 2004; McCullough, 2014). Spikes in the Si/Ti trend will indicate biogenic silica owing to the lack of terrigenous material, and low values will indicate terrigenous material as it will have higher Ti present.

In addition to the proxies above, K and Al will be used as terrigenous clay content proxies. These must be used in conjunction as Al can be associated with detrital and authigenic feldspar (Treaton 2014; Crosby, 2015; Hornbuckle, 2017). They show a good positive correlation, suggesting some similarity in origin. Nance and Rowe (2015) interpret clay-rich intervals as the late phase of deposition or as a result of a shift in depositional axes. They further elaborate that in the absence of turbidity currents or other depositional mechanisms, or simply in periods of slow sedimentation rates, that clay will most likely settle and accumulate in the sediment (Nance and Rowe, 2015).

4.1.3 Carbonate Proxies

In order to identify carbonate material, Ca, Sr, Mg, P, and Mn will be used as proxies. The most representative and reliable for carbonate identification include Ca and Sr (Turner et al., 2016). Ca as it is the main constituent in carbonates and Sr as it tends to replace Ca. Mg is included in this study owing to the presence of syn-depositional dolomite. It is necessary to include P, as both Ca and Sr can be present in phosphate accumulations. However, it will be shown to be uncommon in this area, as this study shows a strong negative correlation of P with Ca and Sr ($r = -0.896$, $r = -0.688$), as it did for Crosby (2015) and Hornbuckle (2017). P may also be an indicator of upwelling, high oceanic productivity and thus oxic conditions, and increased flux in organic matter (Tribovillard et al., 2006). In this study it shows a strong positive correlation with Si ($r = 0.917$) and a medium correlation with Si/Ti ($r = 0.346$). This correlation suggests that it is present in the cherts, meaning they are phosphatic and indications of high organic productivity. However, it is not necessarily a straightforward or reliable proxy (Tribovillard et al., 2006). Mn is included as it can form in carbonate accumulations, however, its enrichment and depletion are highly sensitive to paleo-redox conditions (Madhavaraju and Lee, 2009). In this study, it is seen showing mostly negative correlation to Ca and Sr ($r = -0.555$, $r = -0.451$).

4.1.4 Redox Sensitive Proxies

In order to characterize paleoredox and paleoproductivity conditions, a suite of Mo, V, Co, Ni, Cu, Mn, U, Th, S, and Cr were analyzed after K.L. Pigott et al. (2007), Crosby (2015), Hornbuckle (2017), Ifunanya (2017). This analysis is possible because certain trace elements are more soluble under oxidizing conditions and less soluble under reducing conditions and thus results in authigenic enrichments in oxygen-depleted sediments (Tribovillard et al., 2006). Identifying paleoenvironmental oxygenation conditions is crucial for understanding organic matter preservation because organic matter is best preserved under anoxic conditions, or when oxygen demand is greater than supply in the sediments (Tribovillard et al., 2006).

Trace elements can be sequestered in sediments along with organic carbon, sedimentary pyrite (Huerta-Diaz and Morse, 1992; Tribovillard et al., 2006; Gregory et al., 2015), clay minerals (Large et al., 2011), and in other cases forming its own sulfide (i.e. CuS, ZnS, etc.). They can be incorporated in Fe-Mn oxyhydroxide particle shuttles in the water column and delivered to the sediment. The consumption of trace elements is also possible through biotic processes, where they can serve as micronutrients for phytoplankton (Tribovillard et al., 2006). In conducting paleoenvironmental analyses, it is important to determine which of these phases the trace element is sequestered.

Pyrite precipitation can occur in the water column or within sediment pore waters under euxinic conditions (Lyons et al., 2003). A study conducted by Yu et al. (2015) has shown a close relationship between TOC and pyrite in deep water-reducing environments. Hydrogen sulfide (H_2S), which is produced from the decomposition of organic matter by sulfate-reducing bacteria, reacts with reduced iron (Fe^{2+}) to form pyrite. This process shows that organic matter is a factor in the formation of pyrite and that there should be a positive correlation between Fe and S and other pyrite inclusions (Yu et al., 2015). Some of these elements that can be included within pyrite are Cu, Ni, Zn, Co, V, and Mo (Gregory et al., 2015).

Ni, Cu, and Zn can be delivered to sediment in association with organometallic complexes (OM) and can serve as markers of high organic matter input into the basin (Tribovillard et al., 2006). Ni shows little to no correlation with Fe or S, showing it may not be in phase with pyrite. It does, however, show a positive correlation with Al and K, showing possible clay association (r = 0.354, r =0.180). It also shows no correlation to Zn but a small positive correlation to Cu (r = 0.103), meaning there may be little to no association with these elements. It is not thoroughly sampled throughout the section which may be the result of depletion in the water column or concentrations below the limit of detection. This makes Ni a weak redox indicator for this study.

Cu shows no correlation with S but a medium correlation to Fe and Mn (r = 0.349, r = 0.299). Zn shows a slight negative correlation to S but a high positive correlation to Fe and Mn. (r = 0.671, r = 0.524). Zn also shows a positive correlation with Cu (r = 0.602) suggesting a similar form, which is likely from either pyrite association or Fe-Mn oxyhydroxide association, and not in the form of Cu or Zn sulfides. However, there is also a medium positive correlation between Zn and Cu with Al and K, suggesting some clay association, slightly lowering the value of these as paleo-redox indicators.

As suggested by Tribovillard et al. (2006), Co should be used with caution as it tends to show strong detrital influence. Although it shows low and medium correlations with S and Fe (r = 0.187, r = 0.335), it also shows a good correlation with detrital proxies (r = 0.616 at highest). Although it may exist in association with other forms, this lowers its dependability as a paleo redox proxy. In addition, its low consistency in sampling makes it unsuitable for this analysis.

Under anoxic conditions, Cr can be absorbed by Fe-Mn oxyhydroxides or strongly detrital by incorporation into clay and ferromagnesian minerals (Tribovillard et al., 2006). However, Cr is not easily taken up by Fe-sulfides, and upon mineralization of OM can become immobile and lost through diffusion into the water column. (Tribovillard et al., 2006). In this analysis, Cr shows medium positive ($r = 0.395$) and high positive ($r = 0.757$) correlations to Mn and Fe, respectively, suggesting absorption into Fe-Mn oxyhydroxides. It also shows a positive correlation across the detrital proxies ($r < 0.724$) and with other redox proxies. However, it also shows a strong negative correlation with Ca and Sr. This suggests multiple origins and phases, lowering the value of Cr as a redox proxy.

V can be transferred from the water column to the sediment through adsorption into OM, precipitated as a solid oxide or hydroxide, and Fe-Mn oxyhydroxide shuttles. It does not, however, readily form sulfides, and can be incorporated into clays through substitution of Al, and incorporated into phosphate nodules (Tribovillard, 2006; Turner, 2016). In this study, it does not correlate with P but does show medium correlations with both redox and detrital proxies across the board, and interpretations of redox conditions with V should be done with caution.

U, carbon rain rates, and TOC have been shown to correlate strongly in anoxic facies (Algeo and Maynard, 2004; Tribovillard et al., 2006; K.L. Pigott et al., 2007). U peaks can indicate bottom water anoxia, higher production or accumulation of in-situ organic matter, or both (Brumsack, 2006). However, an increase in oxygen penetration depth in the sediments can cause remobilization of U, causing a migration of the initial U peak to another location (Tribovillard et al., 2006). Owing to its inconsistent sampling, U will be used sparingly in this analysis. However, the U/Th ratio will be used where possible, as it has been shown by (Jones and Manning, 1994) to be a quantifiable indicator of oxygenation conditions. It was shown that in general, values less than 1.25 tend to be more oxic, values near 1.25 tend to be suboxic, and values greater than 1.25 tend to be anoxic. In addition, a pseudo-Gamma Ray API was calculated where possible, as it has been shown by Xu (2018), Hornbuckle (2017) and Crosby (2015) to be very strongly correlated with SGR measurements. Gamma Ray serves as a reliable indicator of shaliness and therefore process energy.

In euxinic conditions, enrichment of authigenic Mo can occur. It can also be delivered to the sediment by organic detritus and Fe-Mn oxyhydroxide shuttles (Tribovillard et al., 2012). Owing to these circumstances, and its lack of detrital influence, Mo has been widely used to analyze the degree of water mass restriction in basins (Tribovillard et al., 2006; Algeo et al., 2007; Algeo and Maynard, 2008; Algeo and Tribovillard, 2009; Smith and Malicse, 2010; Harris et al., 2013). However, Algeo and Rowe (2012) indicate that lack of Mo and even V enrichment can also indicate the basin reservoir effect, where increasing restriction results in low deep-water Mo concentrations as a result of Mo removal to the sediment in excess of resupply from ocean waters, and not as a result of reducing conditions. Therefore, these proxies need to be used in conjunction with other paleoredox indicators.

Mn can also be associated with suboxic to anoxic conditions. Mn concentrations are found elevated in oxygen-minimum zones in present-day basins (Brumsack, 2006). It has also been shown by Madhavaraju and Lee (2009) that fluctuating concentrations of Mn is a response to changing paleo-oxygenation conditions in the basin. They argue that Fe and Mn show similar cycling patterns across redox boundaries at the sediment water interface and has implications on paleoredox conditions. Madhavaraju and Lee proposed the Mn* proxy that normalizes measured Mn and Fe sample readings to PAAS values (McLennan, 2001) of the same elements, and then takes the log of the ratio of these values as shown:

$$Mn^* = \log [(Mn_{sample}/Mn_{PAAS})/(Fe_{sample}/Fe_{PAAS})]$$

This proxy provides a relatively simple way to look into redox potential, with negative values implying redox potential or anoxic conditions, low positive values representing sub-oxic conditions, and values greater than one suggesting productive, oxic conditions (Madhavaraju and Lee, 2009; Crosby, 2015; Hornbuckle, 2017).

4.2 Lithologic Conversion

The elemental data extracted from the XRF analysis were used in this study in order to generate a lithologic composition by converting the main elemental constituents into its respective mineralogy. An unpublished Microsoft Excel program written by Dr. John D. Pigott was used for this conversion (personal communication). The program calculates the seven basic mineral families common to Leonardian carbonate dominant lithologies of West Texas - New Mexico (Siderite, Gypsum-Anhydrite, K-spar, Dolomite, Calcite, Albite-Clay, and Quartz). The procedure is based upon the elemental concentrations principal to each mineral (Fe, S, K, Mg, etc.) which are determined in standards and then calculated from measurement by subtracting in succession the percentage of each element of each mineral (removing the inter-elemental interference of each mineral's characteristic spectrum). Then the percentages are normalized to 100% and output. Error using standards, artificial mixtures, and comparison to XRF results for mineral assemblages common to the region reveal accuracies generally not exceeding 5%.

In this study, albite-clay and k-feldspar are combined as there is a rare amount of detrital or authigenic feldspar, and the mineral's elemental constituents are fairly indiscernible. The main clay minerals found in the Bone Spring Formation tend to be illite and minor kaolinite, in which a simple K/Al ratio can be used to estimate the percentage of each present (Crosby, 2015).

4.3 Chemostratigraphic Facies Definition

Defining chemofacies is a proven technique in order to reveal information not previously evident in analyzing outcrop or core alone, or even within the geochemical proxies (Nance and Rowe, 2015; Turner et al., 2015; Turner, 2016). This method is especially helpful in outcrops such as those in the study area, which contain a large amount of seemingly homogeneous strata (C.F. Slatt et al., 2012; Slatt and Rodrigues, 2012). They will provide an opportunity for better characterization of paleo depositional and paleo oxygenation conditions of the Bone Spring Formation and Leonardian times just before the transition to the Guadeloupian (Riquier et al., 2005), as well as characterization of rock properties as well.

4.3.1 Hierarchical Cluster Analysis

In order to generate chemostratigraphic packages, a hierarchical clustering algorithm was used. A combination of 25 major, minor, and trace elements was used, in addition to the Si/Ti biogenic indicator ratio, the XRF "Bal" number (estimation of remaining element mass lighter than Mg not counted by the device), and the R Schmidt Hammer hardness value. The statistical program used was XLSTAT by Addinsoft.

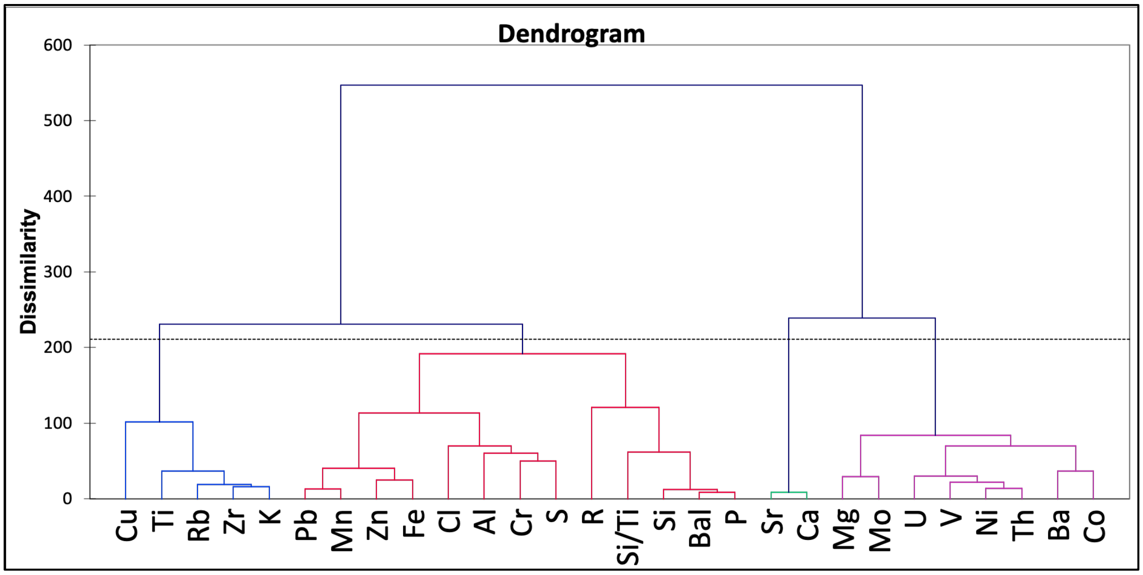

Figure 10. Dendrogram clustering elements analyzed, showing four main groups split by the dotted black line and a total of nine sub-groups split by the blue line. Generated with XLSTAT by Addinsoft.

Clustering was computed both across columns and across rows. Clustering across rows produces a dendrogram as shown in Figure 10. The function of this analysis is to perform a secondary correlation analysis and can be used to validate the elements chosen for each proxy study by showing the similarity of occurrence. The dendrogram in Figure 10 has created four main clusters. The blue cluster has grouped related redox and terrigenous proxies, the left leg of the red cluster has grouped a set of redox and clay proxies, the right leg of the red cluster has grouped biogenic chert proxies along with the Schmidt R value, the green group has clustered carbonate proxies, and the purple group has clustered mostly redox proxies.

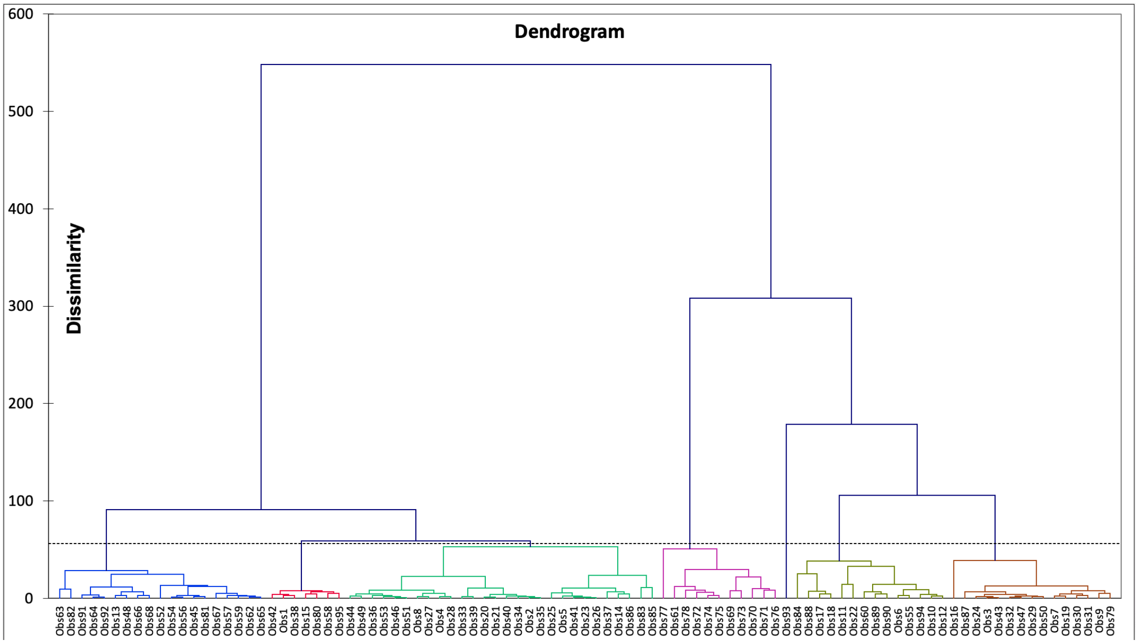

Figure 11. Dendrogram showing the clustering of every observation. The dotted black line shows the division used to create a total of seven chemofacies used in this study. Generated with XLSTAT by Addinsoft.

In order to generate meaningful chemostratigraphic packages, clustering across columns must be done. This assigns each observation point a cluster in which it is most similar. In this case, seven clusters were generated to best represent the lithology present, as shown in Figure 11. The lithologic composition of each package is described in Table 1, while the composition of redox proxies is described in Table 2.

Chemostratigraphic Packages	Si	Ti	Zr	Si/Ti	Al	K	P	Ca	Sr
🟦 Package 1	Low terrigenous, low biogenic, low clay, medium to high carbonate								
🟦 Package 2	Medium terrigenous, very low biogenic, low to medium clay, very high carbonate								
🟦 Package 5	Low to medium terrigenous, low to medium biogenic, low to medium clay, medium to high carbonate								
🟫 Package 6	High terrigenous, low biogenic, high clay, low carbonate								
⬛ Package 4	Low to medium terrigenous, medium to high biogenic, medium clay, low carbonate								
🟨 Package 3	Low terrigenous, very high biogenic, low clay, low carbonate								
🟧 Package 7	Low to medium terrigenous, low biogenic (but high phosphatic), medium to high clay, low carbonate								

Table 1. This table shows a non-quantitative description of lithology determining proxies. Note that the packages have been ordered by silica and calcite levels.

Chemostratigraphic Packages	GR (API)	U/Th	Mn*	Zn	Ni	Cu	S	V	Cr	Fe	S
🟦 Package 1	NM or 63-104	0.69 to 2.5	0.45 to 1	Low Zn and Fe / low to medium Cu, S, V / medium Cr / high Ni							
🟦 Package 2	NM or about 60-70	0.95 to 1.36	0 or about 0.5 to 1.2	Low Zn and Fe / low to medium S and Cr / medium V / high to very high Ni							
🟦 Package 5	NM	NM	0 or about 0.45 to 0.75	No measured Ni or V / medium Fe and Zn / low to high S and Cr / medium to very high Cu							
🟫 Package 6	NM or 81 to 117	1.26 to 1.32	0 or 0.23 to 0.78	Low to medium Zn and Fe / medium Cu / medium to high Ni, S, V, and Cr							
⬛ Package 4	NM or 71 to 111	0.98 to 2.12	-0.1 to 1.5	Low to very high V / medium to very high Zn, Fe, Ni, Cu, S / very high Cr							
🟨 Package 3	NM or 43 to 53	1.09 to 1.52	0 or 0.44 to 1.24	Low to medium Zn, Fe, Cu, V / medium Ni, Cr / low to high S							
🟧 Package 7	NM	NM	1.86	No measured Ni or V / high Cu / very high Zn, Fe, S, Cr							

Table 2. This table shows quantitative and non-quantitative description of redox indicative ratios and redox proxies. Note that the packages remain in the previous order determined by silica and calcite levels.

Chapter 5: Observations and Results

This chapter will discuss the results and observations at outcrop locations 1A-1B, 1C-1D, and 2A-2B, moving from the basinal Bone Spring Limestone and upwards to the more proximal slope deposits. This will provide a geologically functional structure for the study and allow for proper comparison of results and observations between locations and therefore depositional environments.

5.1 Stratigraphic Section 1A-1B

5.1.1 Outcrop Characteristics 1A-1B

The accessible outcrops of the north wall of Shumard Canyon are stratigraphically lower and deeper than those found along the south wall. Section 1A, shown in Figure 12, contains 23 measurements each about one foot apart in the true vertical direction of the E-SE dipping beds. It is the stratigraphically lowest section in this study, and as expected, these units contain thin-bedded, dark grey to black, organic-rich, usually bioclastic, lime wackestone to packstones. There is an abundance of lensed to layered siliceous chert as well. The chert is pale white to light brown, mainly porcelain in texture, with thickness reflective of the thickness of the limestone bed it resides in (<1mm up to 15cm for cherts). The lithofacies is very consistent in this section. It is mostly thin-bedded with a few periodic increases in bed thickness. In addition to bed thickness, beds tend to alternate between massive, parallel laminated, low amplitude ripple laminated, and deformed (soft-sediment deformation). There are also a few low amplitude styolites near the base of the section.

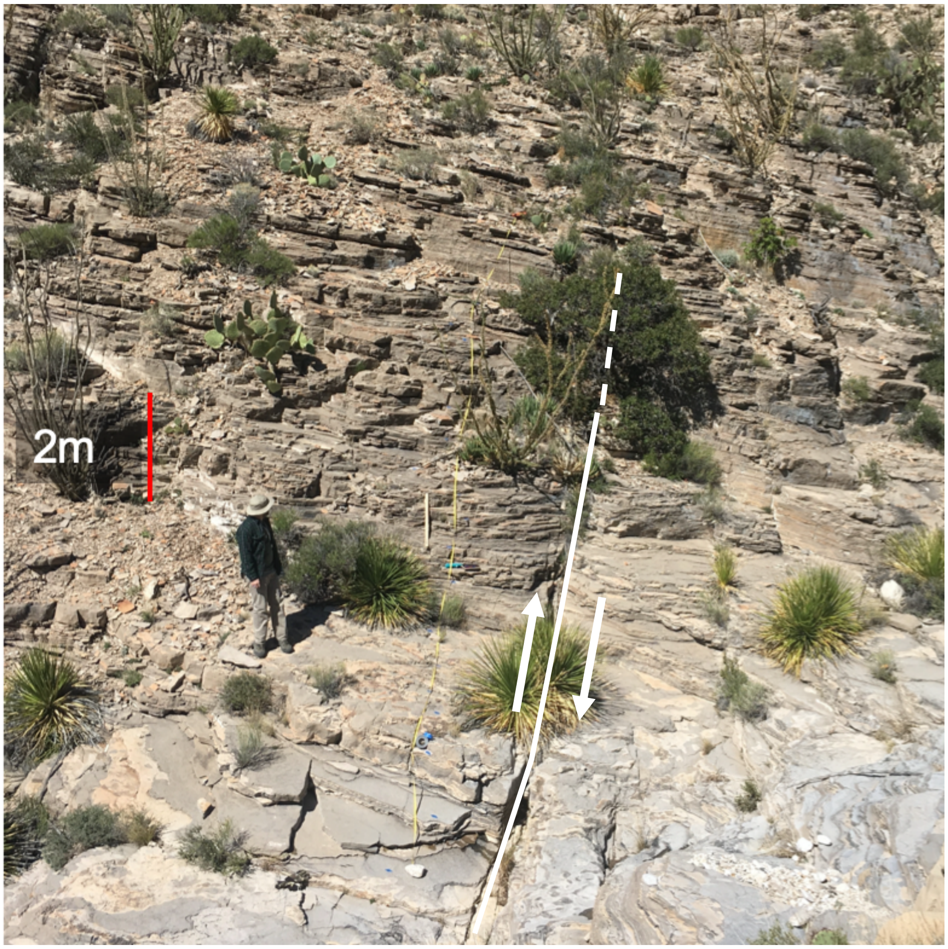

Figure 12. Outcrop photograph showing measured section ALDS 1A with meter stick for scale. Note the high levels of chert and the North- North East trending high angle normal fault. These features typify the Bone Spring Limestone outcrops in Shumard Canyon.

Shown above in Figure 12 is section ALDS 1A, the western-most section near the mouth of the canyon, as shown in Figure 7. There are multiple NE striking normal faults within the section and throughout the canyon, which have on average 75 to 89 degree fault plane dip and very small offset, such as the one pictured above in Figure 12. This offset is accounted for when tracing the highest bed in the stratigraphic section to the lowest bed of the next stratigraphic section, in this case, section 1B. Section 1B, shown in Figure 13, contains thirteen measurements each about one foot apart in the true vertical direction to the beds. These beds tend to show very similar lithologic features to the beds in 1A. Shown below in Figure 13 is section ALDS 1B, just east of ALDS 1A, as shown in Figure 7. Section 1B contains a thin-bedded portion near the base which then thickens upward through the section, then alternates between thin and thick beds. This thickening is a potential result of changing sediment supply into the basin per depositional pulse or slight shift from distal to proximal site of the deposition.

Figure 13. Outcrop photograph showing the base of measured section ALDS 1B. Note the thickening of beds moving up-section, along with the thickening of the bedded cherts, marked by the green line.

In looking at the thicker beds in the middle portion of this section, it evident that these beds tend to have thin-bedded, recessive, micritic units at their base. This, along with the alternating massive and planar laminae, local inverse and regular grading, and secondary silicification is a characteristic of calciturbidite deposition (Rupert et al., 2007). The stratigraphic column below in Figure 14 details the observations in the field for sections 1A-1B.

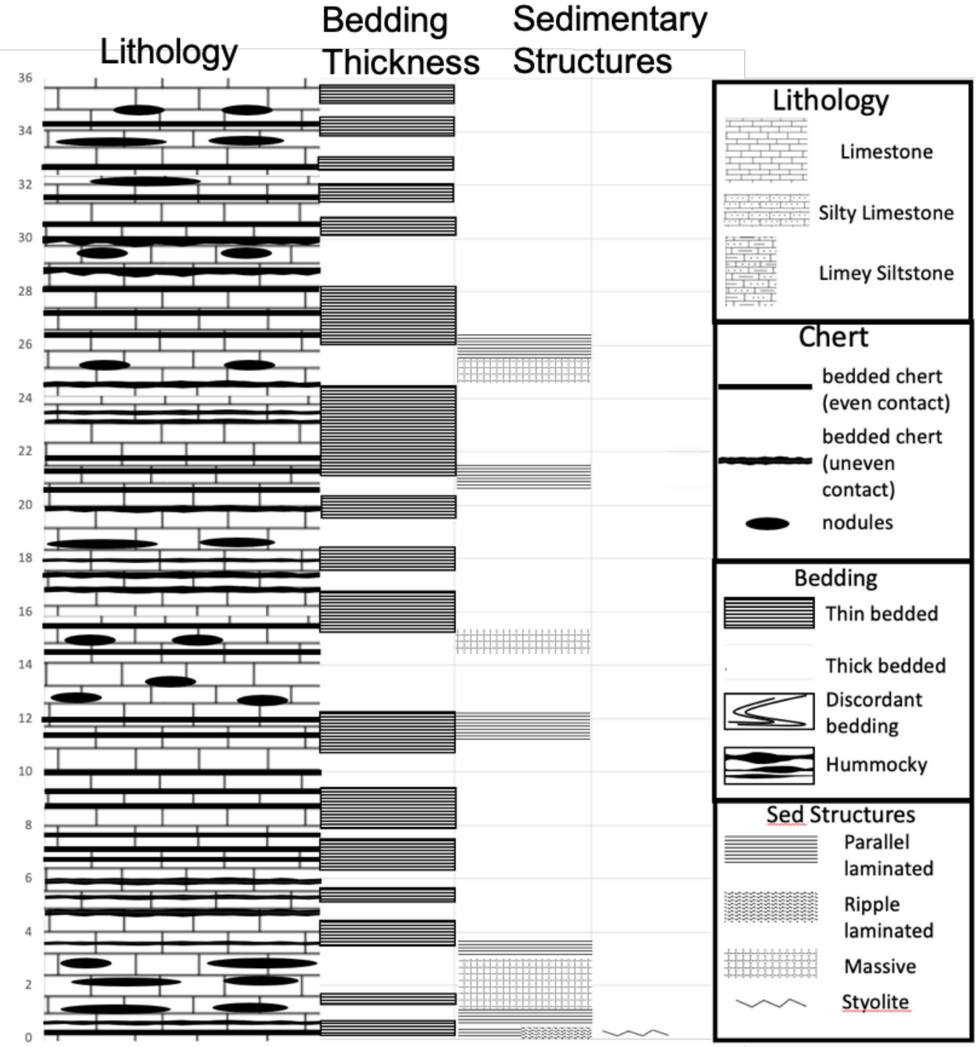

Figure 14. Combined stratigraphic section of ALDS 1A to 1B, found closest to the mouth of the canyon as shown in Figure 7. Note the slight correlation between chert nodules and thickening of chert beds with the thickening of limestone beds.

5.1.2 Petrographic Analyses 1A-1B

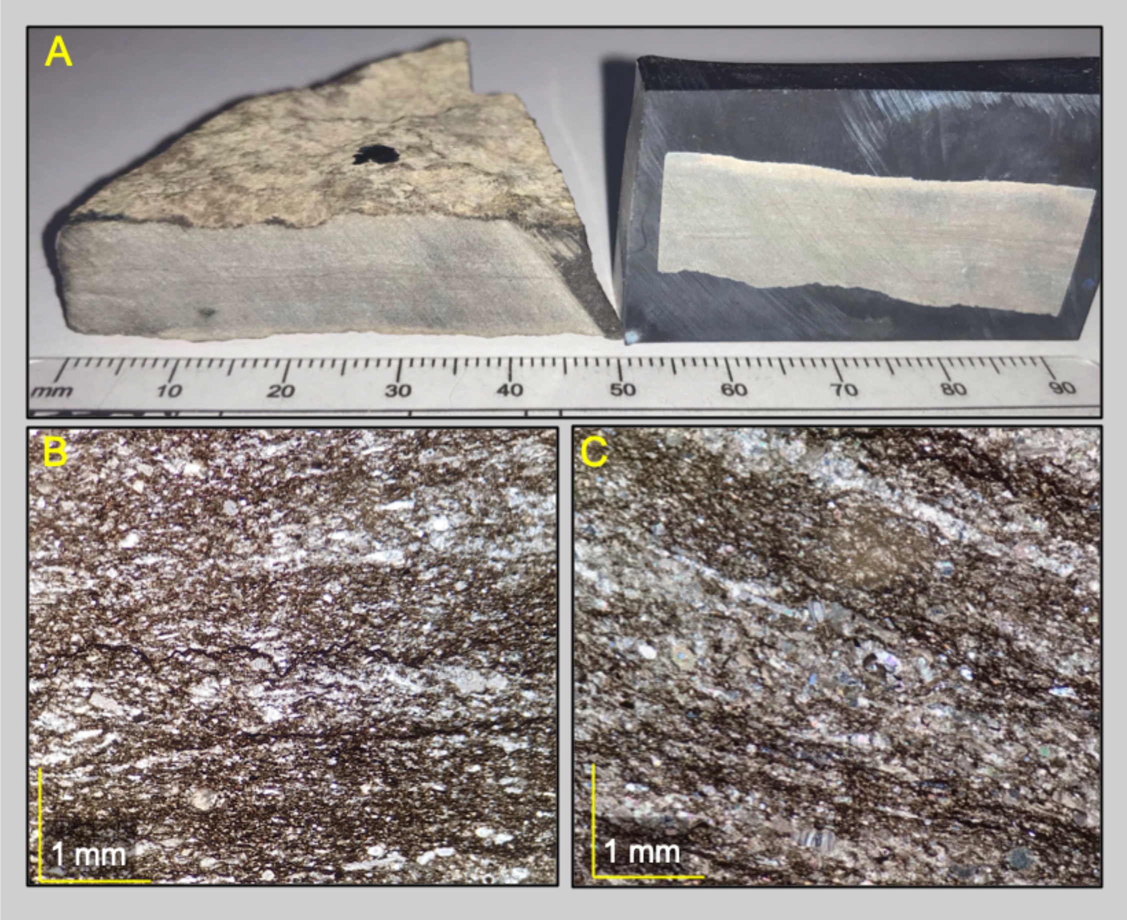

Figure 15. Petrographic analyses of sample taken at point 1A1. A) Hand sample. B) Thin section micro photograph taken in plane polarized light at 4X power. C) Thin section micro photograph taken in cross polarized light at 4X power.

Sample 1A1 is a black, lime, wackestone to packstone which is very fine-grained and well sorted. It contains tan colored planar to subtle ripple laminations, low amplitude styolites, tan to dull light grey bioclasts, and a calcite matrix. The laminae show alterations between packstone and wackestone, with the packstone containing higher levels of calcite grains and spar which has been broken and elongated with the bedding, indicating reworking of carbonate muds from the shelf into the basin (Figure 15 B and C). There is also organic matter within the styolites and throughout the rock, as well as moderate amounts of pyrite. There is a high level of bioclastic fragments that can be identified as deriving from echinoderms, brachiopods, bivalves, trilobites, and foraminifera. Radiolaria, sponge spicules, detrital quartz, dolomite, intraclasts, authigenic feldspar and calcite-healed fractures are also present but very sparse throughout this sample.

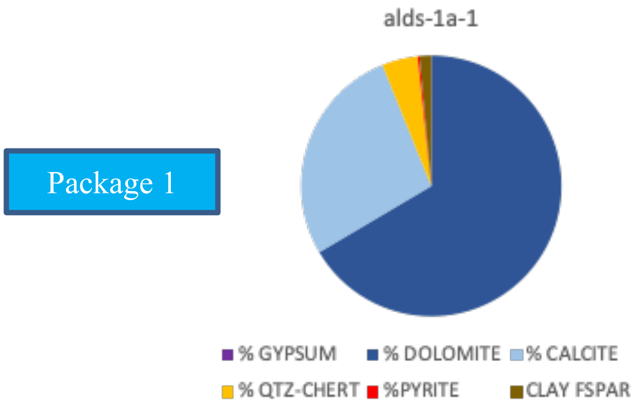

Figure 16. XRF-derived minerology and chemostratigraphic package for sample 1A-1.

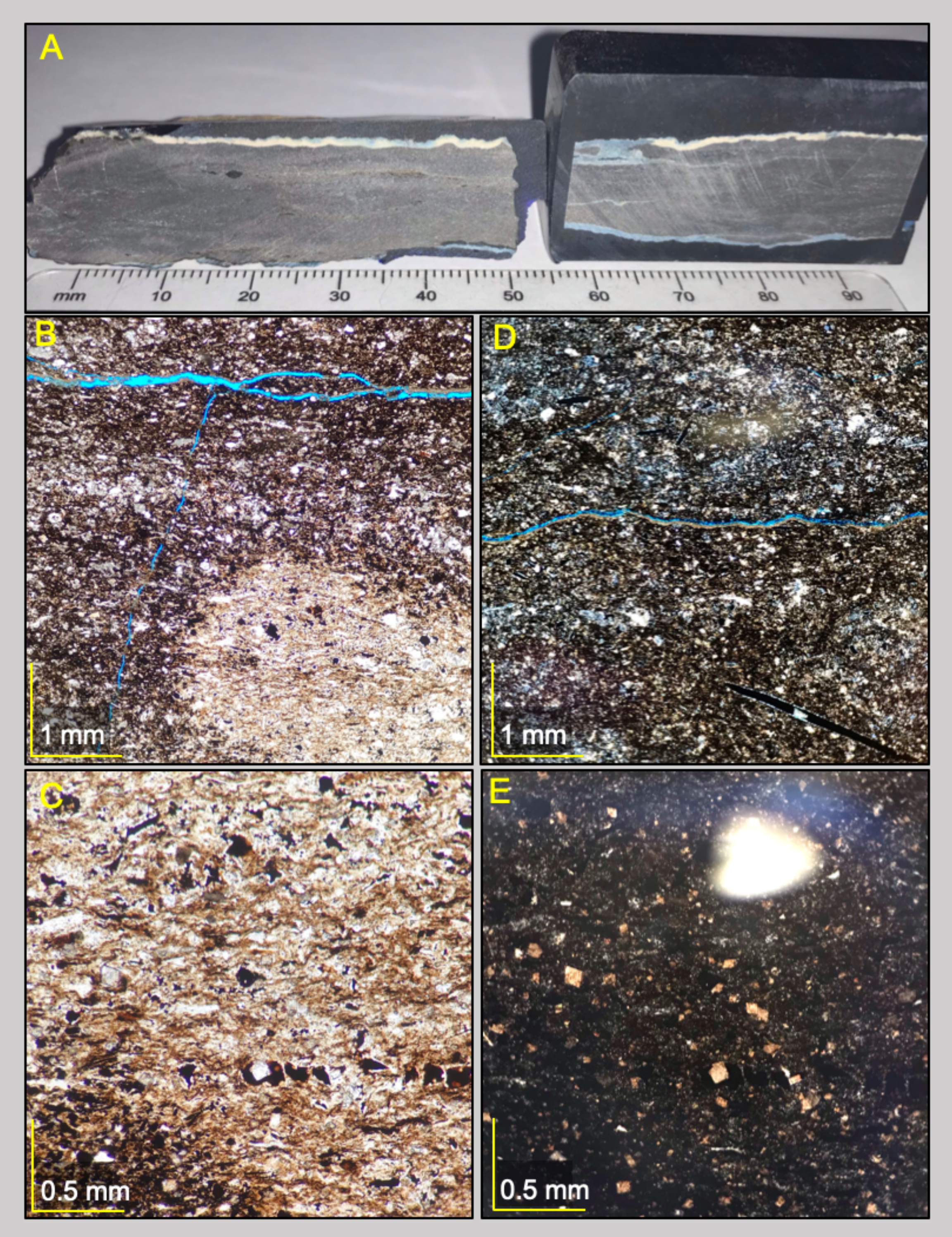

Figure 17. Petrographic analyses of sample taken at point 1A16. A) Hand sample. B) Thin section micro photograph taken in plane polarized light at 4X power. C) Thin section micro photograph taken in cross polarized light at 10X power. D) Thin section micro photograph taken in cross polarized light at 4X power. E) Thin section micro photograph C taken in cross polarized light at 10X power and low light.

Sample 1A16 is a black, heavily silicified limestone which is very fine-grained and well sorted. It is a massive bedded packstone with minor zones of wackestone, contains white (silicified) bioclastic material, and irregularly shaped silicification characterized (Figure 17, A and B) by the light grey color in hand sample and is slightly porcelain. In the thin section, there are few bioclasts and high levels of radiolaria and spicules present to supply biogenic silica for silicification. These constituents, in addition to the bioclasts, can be seen partially preserved or completely replaced with silica or filled with organic matter. There are moderate to high levels of organic matter, pyrite, dolomite, and natural fractures throughout the rock. The dolomite is rhombohedral and mostly found in the heavily silicified zones, as seen in Figure 17 C and E. It is also worth noting the style of the fractures. They are mixed open and healed. The open fractures are either clean or contain slightly gouged zones and incomplete calcite/dolomite healing. They tend to follow bedding planes and stairstep at angles of either 100-120 degrees and 60-80 degrees.

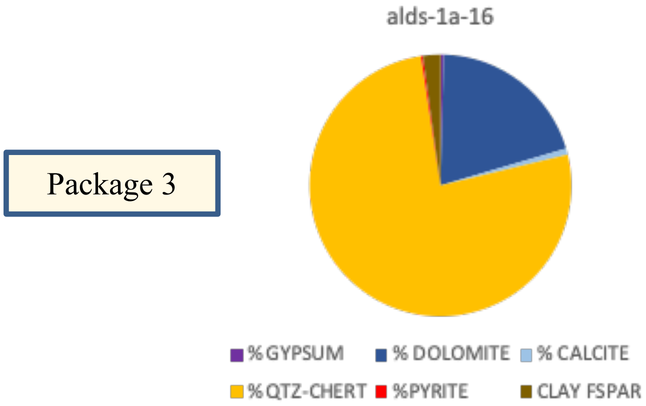

Figure 18. XRF-derived minerology and chemostratigraphic package for sample 1A-16.

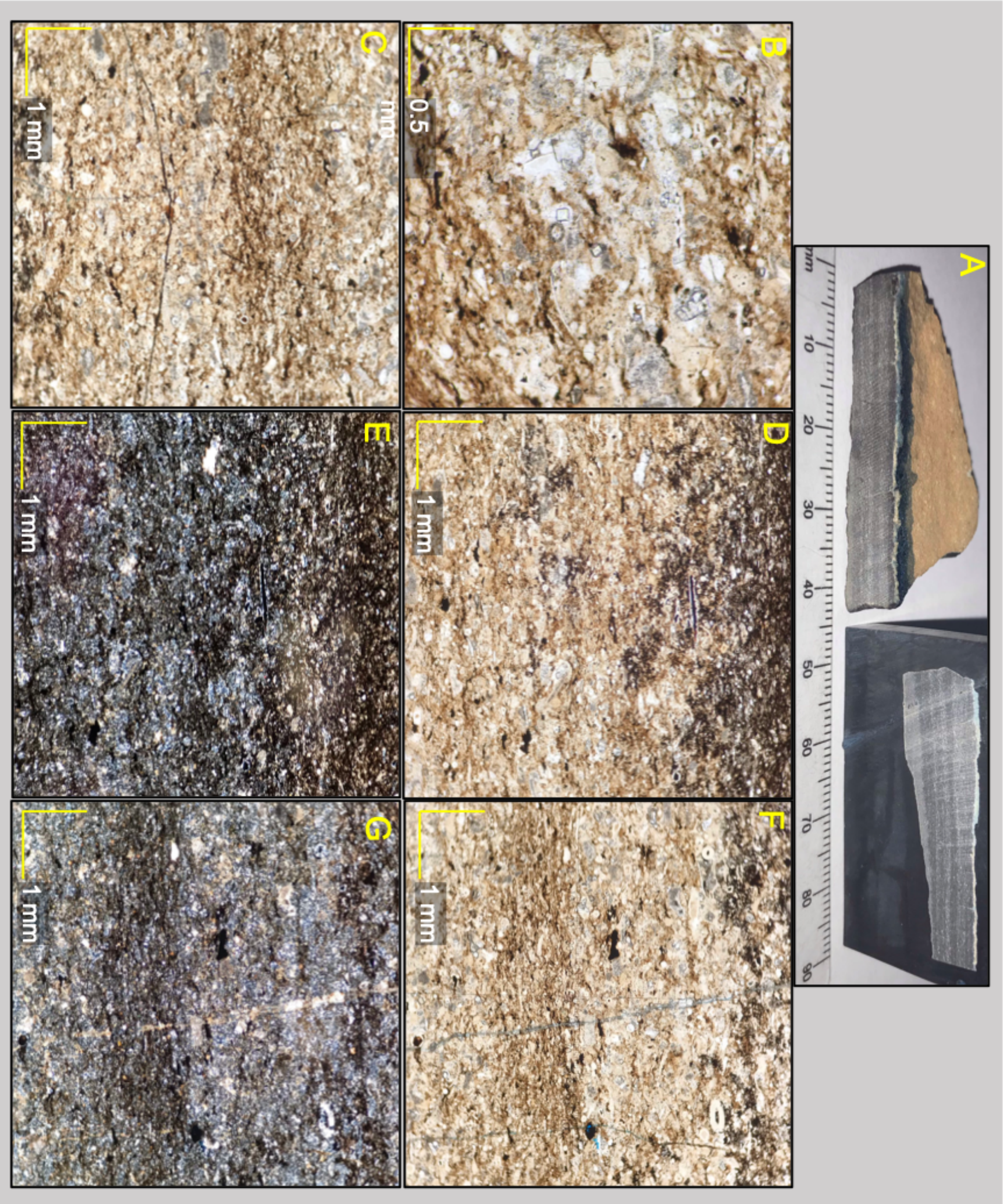

Figure 19. Petrographic analyses of sample taken at point 1A22. A) Hand sample. B) Thin section micro photograph taken in plane polarized light at 10X power. C) Thin section micro photograph taken in plane polarized light at 4X power. D) Thin section micro photograph taken in plane polarized light at 4X power. E) Thin section micro photograph D taken in cross polarized light at 4X power. F) Thin section micro photograph taken in plane polarized light at 4X power. G) Thin section micro photograph F taken in cross polarized light at 4X power.

Sample 1A22 is a black laminated limestone which is very fine-grained and well sorted. Laminations are mostly planar and alternate between un-silicified and silicified packstone and minor interbedded wackestone, as indicated by the white (silicified) bioclastic material and light grey matrix in hand sample. Calcite grains and spar can be seen broken and elongated with the bedding, indicating the reworking of carbonate muds from the shelf into the basin. There are few bioclasts and high levels of radiolaria and spicules present to supply biogenic silica for silicification. These constituents, in addition to the bioclasts, can be seen partially preserved or completely replaced with silica as micro quartz and chalcedony or filled with organic matter. There are moderate to high levels of organic matter, pyrite, intraclasts, and natural fractures throughout the rock. There is a low to moderate level of dolomite which is rhombohedral and mostly found in the heavily silicified zones, as seen in Figure 19 B. The fractures are mixed open and healed, while the open fractures are generally hairline and the larger fractures are generally healed (Figure 19 C, F, G).

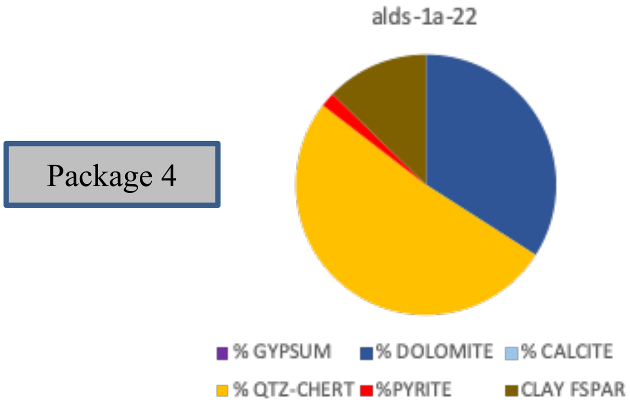

Figure 20. XRF-derived minerology and chemostratigraphic package for sample 1A-22.

5.1.3 Geochemical Proxy Results 1A-1B

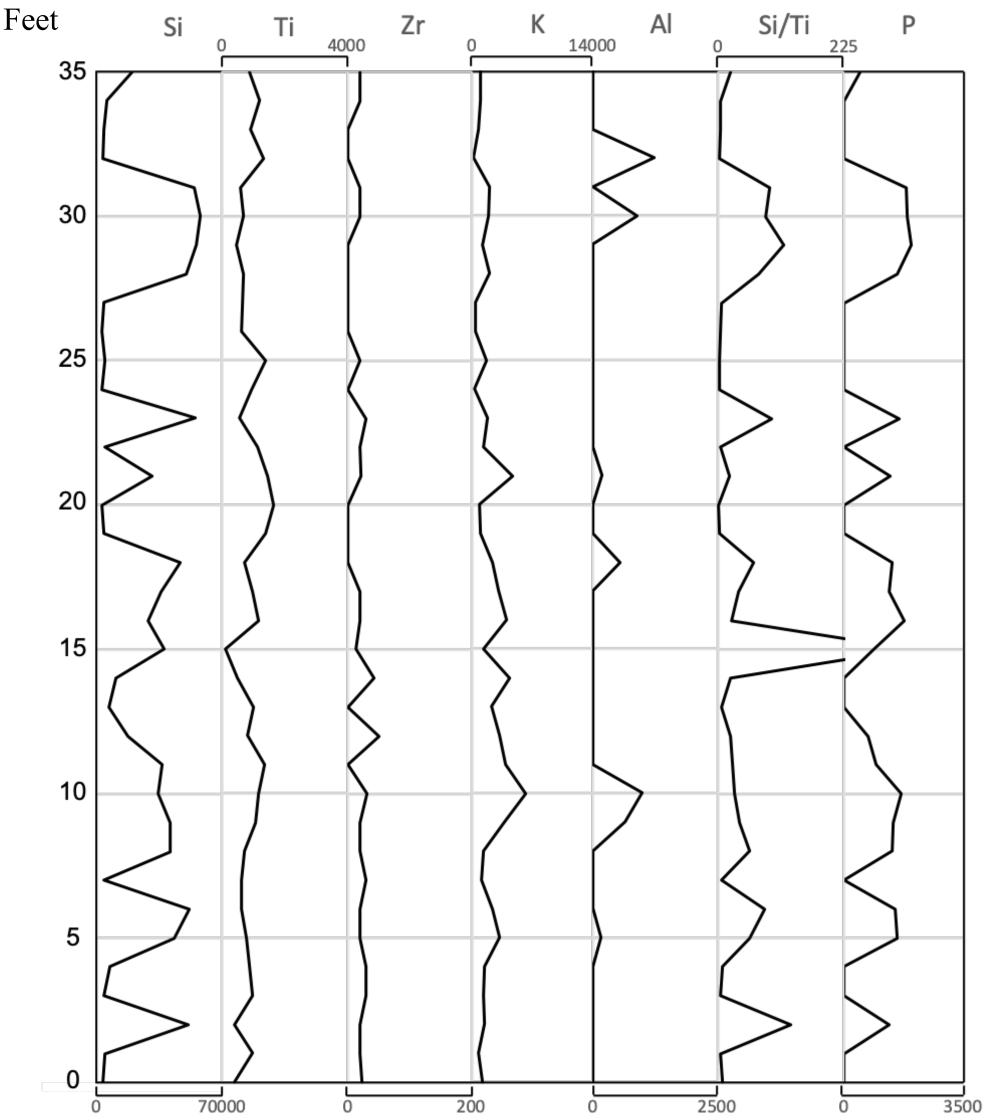

Figure 21. Siliciclastic elemental suite (ppm) for measured sections 1A-1B.

As displayed in Figure 21, Si, Si/Ti, and P show significant covariation, indicating that trends in silica alone must be interpreted with caution due to the large abundance of biogenic, siliceous cherts in this section. Ti, Zr, K, Al show decent covariation and will serve as the main indicator of terrigenous material (sands, silt, and clay). Most large spikes in Si can be attributed to biogenic chert; however, as thin section evidence has shown, some units show zones of partial silicification to varying degrees, in either non-structured zones or along bedding planes. This silicification can be seen in data points at 9-11 feet, 22 feet, and 35 feet, where a medium spike in silica is met with a slight increase in Ti, Zr, K, and Al, and low Si/Ti values and generally medium to high P.

There is a subtle increase in clay proxies (K and Al) from about four feet to ten feet, followed by a decrease throughout the rest of the section. The clay material that has made it could be aeolian in origin or resulted from slow background deposition owing to slow fallout rates in the water column.

Other than these points and variation between biogenic cherts, siliciclastic proxies remain low in this section and do not show great changes in trends. These low levels of terrigenous proxies indicate sea level highstand and that the terrigenous material was either not being delivered from the intracratonic environment or it was being choked off by carbonate shelves.

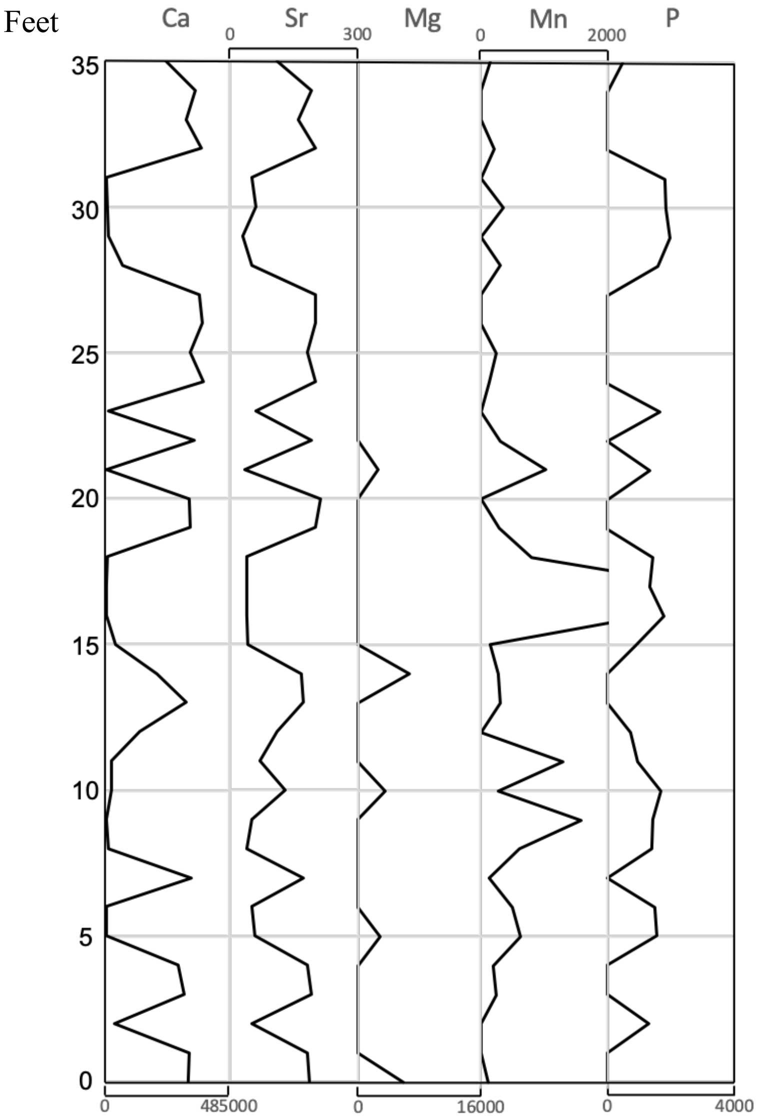

Figure 22. Carbonate elemental suite (ppm) for measured sections 1A-1B.

The carbonate elemental suite for section 1A to 1B is shown above in Figure 22. Section 1A to 1B shows significant covariation between Ca and Sr, no covariation with Mg, and slight covariation between Mn and P. Mg most likely shows little covariation owing to its extremely light atomic weight and difficulties in outcrop-based detection. P and in some cases, Mn can be used as identification of biogenic silicification, which shows a high negative correlation with Ca as discussed in chapter 4.1.1. Peaks in Ca and Sr show a very subtle decrease from zero feet to about 15 feet, and a subtle increase from 19 feet to 32 feet, followed by another slight decrease until 35 feet. Since Mn is not associated with carbonates, it is most likely representative of paleoproductivity and ocean oxygenation conditions owing to its sensitivity to redox environments.

This constant high in carbonate proxies and biogenic chert abundance is characteristic of a slope environment of a high stand sea. The presence of Ca and Sr along with the carbonate material seen in the thin section further support this and indicate active carbonate production on the shelf and the delivery of carbonate debris to the slope.

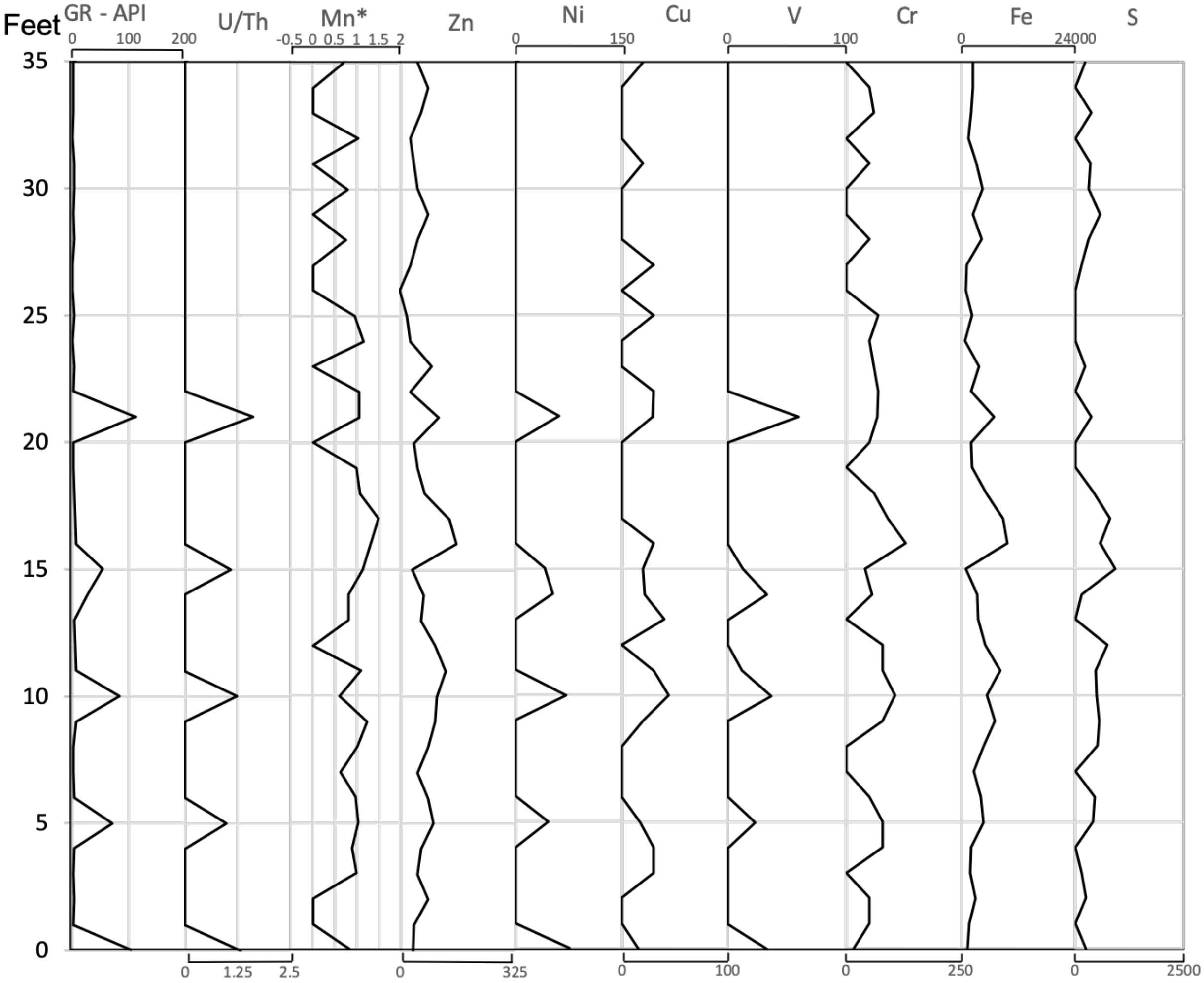

Figure 23. Redox ratios and paleoenvironmental indicators for measured sections 1A-1B. Individual elements plotted in ppm.

The redox profile for section 1A to 1B is shown above in Figure 23. It shows good covariation between Fe, S, and Zn, and minor covariation with Cu, Cr, and Mn*. These show an increasing trend from zero to about 11 feet, then a drop from 11 to 15 feet. This drop is followed by a jump at 16 feet and then a decreasing trend until about 26 feet. These trends then raise a small amount and continue on at stasis through the rest of the section. The sparse U and Th data are worth noting, as gamma values at zero feet and 21 feet are above 100 API, and between 50 to 85 API at 5, 10, and 15 feet. The points above 100 API have U/Th just around or slightly above 1.25, which is indicative of a sub-oxic to possibly anoxic environment. The points below 100 API are just around or slightly below 1.25 U/Th ratio, indication sub-oxic to possibly oxic environment.

The higher level of Mn* from zero to 22 feet suggests a slightly oxic environment, with a few dips into a suboxic and possibly anoxic environment. The covariation with the high Zn, Ni, Cu, Fe, and S, suggests high levels of organic matter input and release of Zn, Ni, Cu from organic matter and the subsequent sequestering within syn-depositional pyrite and other sulfides. The pyrite can be seen in thin section and is described in the previous section.

5.2 Stratigraphic Section 1C-1D

5.2.1 Outcrop Characteristics 1C-1D

Section 1C, shown in Figure 24, contains just seven measurements each about one foot apart in the true vertical direction of the E-SE dipping beds. It is a stratigraphic continuation of section 1B. It contains a thick-bedded, dark grey to black, organic-rich, bioclastic lime wackestone to packstones. There are two main lithofacies in this section, characterized by sorting and color. The first is a characteristically black, very fine-grained, well-sorted wackestone/packstone. The second is a dark grey, very fine to medium-grained, moderately to poorly sorted, bioclastic wackestone to packstone. The main constituents varying in size are the bioclasts. There remains an abundance of lensed to layered siliceous chert as well, of similar characteristics as before. The section contains mostly thick beds with a few periodic decreases in bed thickness. In addition to bed thickness, beds tend to alternate between massive, parallel laminated, low amplitude ripple laminated, and rare deformed (soft-sediment deformation).

Figure 24. Outcrop photograph showing measured section ALDS 1C. Note the thick hummocky bed in the upper center part of the photo with thin, recessive micrite layers above and below. These features are relatively common throughout Shumard Canyon.

Shown above in Figure 24 is section ALDS 1C, located just east of section 1B as shown in Figure 7. As Figure 24 shows, some thicker beds in the canyon exhibit morphology similar to that of the upper bed behind the bush (also seen more clearly in Figure 25). This appears to be a large hummocky structure, with thin recessive, micritic layers above and below, and could be indicative of up-slope catastrophic failure resulting in a higher flow regime, massive release of debris, paired with high rates of sedimentation, as discussed in similar units by Hornbuckle (2017) and Moreland (2019) in the Rader formation. Therefore, it is possible that this high energy calciturbidite is a tsunamite. It is also worth noting that the siliceous replacement in the unit, in addition to the thin, recessive micrite under-beds, is characteristic of calciturbidites. In looking at Figure 24, it also appears that the units above the hummocky bed follow the morphological trends, meaning it was deposited along with this as inherited topography, suggesting this feature is syn-depositional.

Figure 25. Outcrop photograph showing transition of measured section ALDS 1C to 1D. Note the thick hummocky bed in the lower center part of the photo, top of which is picked with white-dashed line. These features are relatively common throughout Shumard Canyon. Also note the silty limestone unit near the top of the photo outlined in white.

Shown above in Figure 25 is section ALDS 1C and 1D, located just east of section 1B as shown in Figure 7. Section 1D starts in the unit just above the large hummocky bed, which was traced further over until measurements could be made starting from the creek bed. Section 1D contains 35 measurements, each about one foot apart in the true vertical direction of the E-SE dipping beds, and is a stratigraphic continuation of section 1C. There are three main lithofacies in this section. The first is a characteristically black, very fine-grained, well-sorted wackestone/packstone. The second is a dark grey, very fine to medium-grained, moderately to poorly sorted, bioclastic wackestone to packstone. The third is a thin-bedded, light tan to grey, well-sorted, calcareous siltstone showing mostly massive or rare parallel laminated sedimentary structure. There remains an abundance of lensed to layered siliceous chert as well, of similar characteristics as before, mostly within the limestone beds. The section contains mostly thin beds with a few periodic increases in bed thickness. In addition to bed thickness, beds tend to alternate between massive, parallel laminated, low amplitude ripple laminated, and rare deformed (soft-sediment deformation).

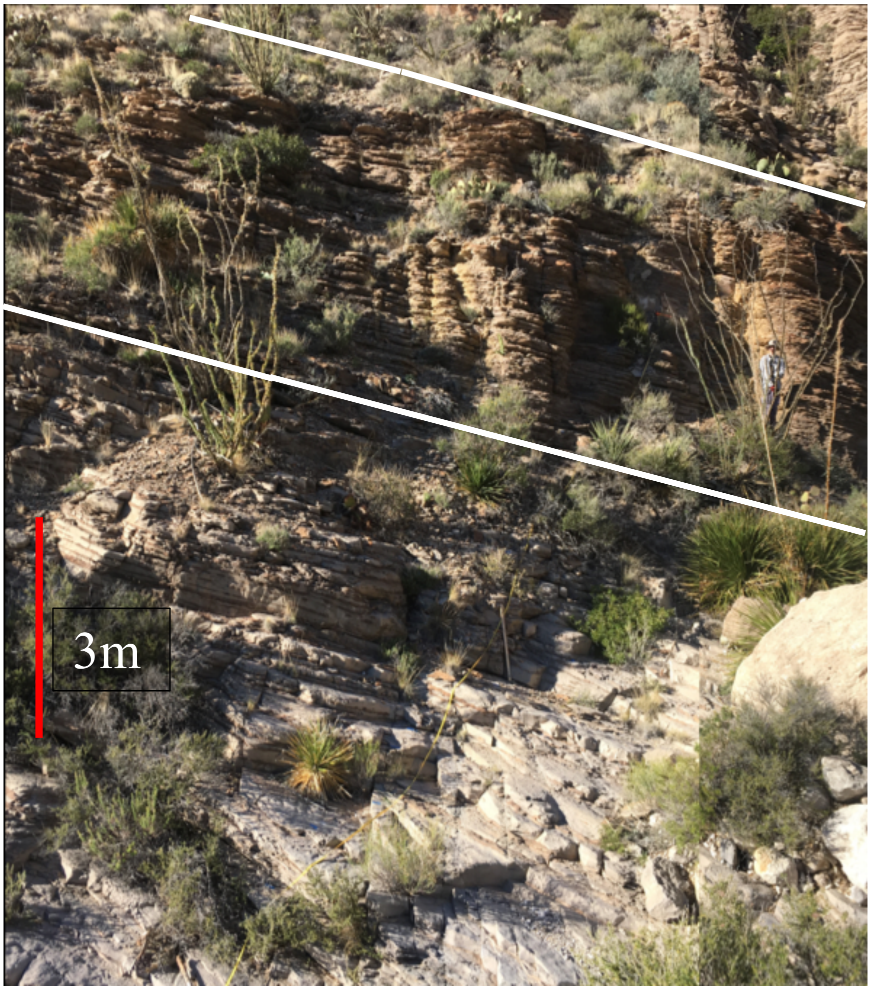

Figure 26. Outcrop photograph showing measured section ALDS 1D, the eastern-most section on the North Wall shown in Figure 7. Note the visible transition in lithology to the calcareous siltstone unit, outlined in by the white line.

As seen in Figure 26, there is a sharp contact between the upper-most limestone bed and the calcareous siltstone. This abrupt contact represents a potential rapid drop in sea level and an increase in siliciclastic input. The actual estimated thickness is about 20 feet or six meters, however, it is worth noting that measurements could only be taken about halfway into this package as the unit was too steep, and the creek-bed turns away from the outcrop allowing these units dip into the cliff-side eliminating any accessible downdip location for measurements, marking the end of this section. The stratigraphic column below in Figure 27 details the observations in the field for sections 1D-1C.

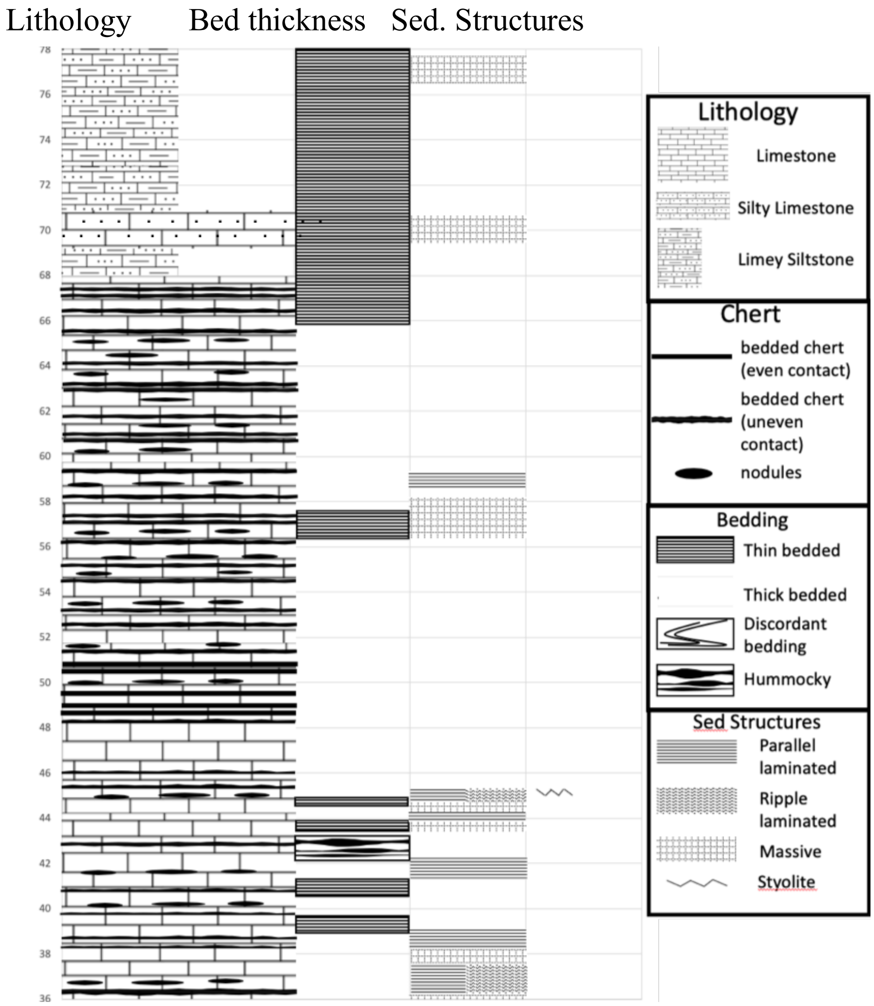

Figure 27. Combined stratigraphic section of ALDS 1C-1D. Note the sharp contact between the limestone and the siltstone. Note that the actual thickness of the calcareous (limey) siltstone is about twice that which is shown here.

5.2.2 Petrographic Analyses 1C-1D

Figure 28. Petrographic analyses of sample taken at point 1D3. A) Hand sample. B) Thin section micro photograph taken in cross polarized light at 4X power. C) Thin section micro photograph taken in plane polarized light at 4X power. D) Thin section micro photograph taken in cross polarized light at 10X power. E) Thin section micro photograph C taken in cross polarized light at 4X power. F) Thin section micro photograph taken in cross polarized light at 4X power.

Sample 1D3 is a dark grey to black limestone which is very fine-grained and well-sorted. It contains subtle light grey ripple laminations, low amplitude styolites, and tan to a dull light grey calcitic matrix. The laminae show alterations between packstones containing higher levels of calcite grains and spar which has been broken and elongated with the bedding, indicating reworking of carbonate muds from the shelf into the basin (Figure 28 B and F). There is also organic matter within the styolites and throughout the rock, as well as pyrite (Figure 28 C and F). Bioclastic fragments can be identified as deriving from echinoderms, brachiopods, bivalves, trilobites, and foraminifera. Radiolaria, sponge spicules, dolomite, intraclasts, and calcite-healed fractures are also present but very sparse throughout this sample although there is a slightly higher amount of terrigenous quartz than the previously analyzed samples. Some bioclasts are replaced will silica as the spicules in Figure 28 C and E have, however most bioclasts have calcite replacement as Figure 28 D shows.

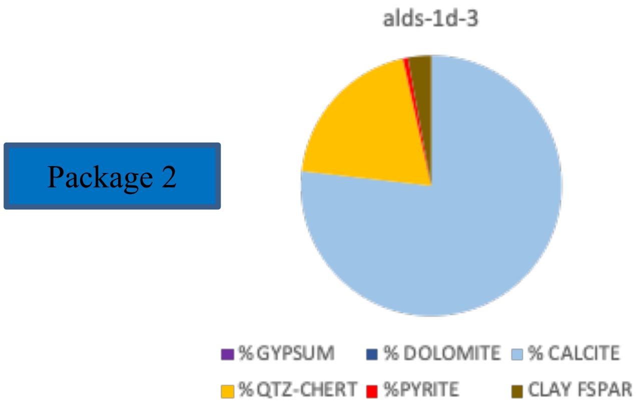

Figure 29. XRF-derived minerology and chemostratigraphic package for sample 1D-3.

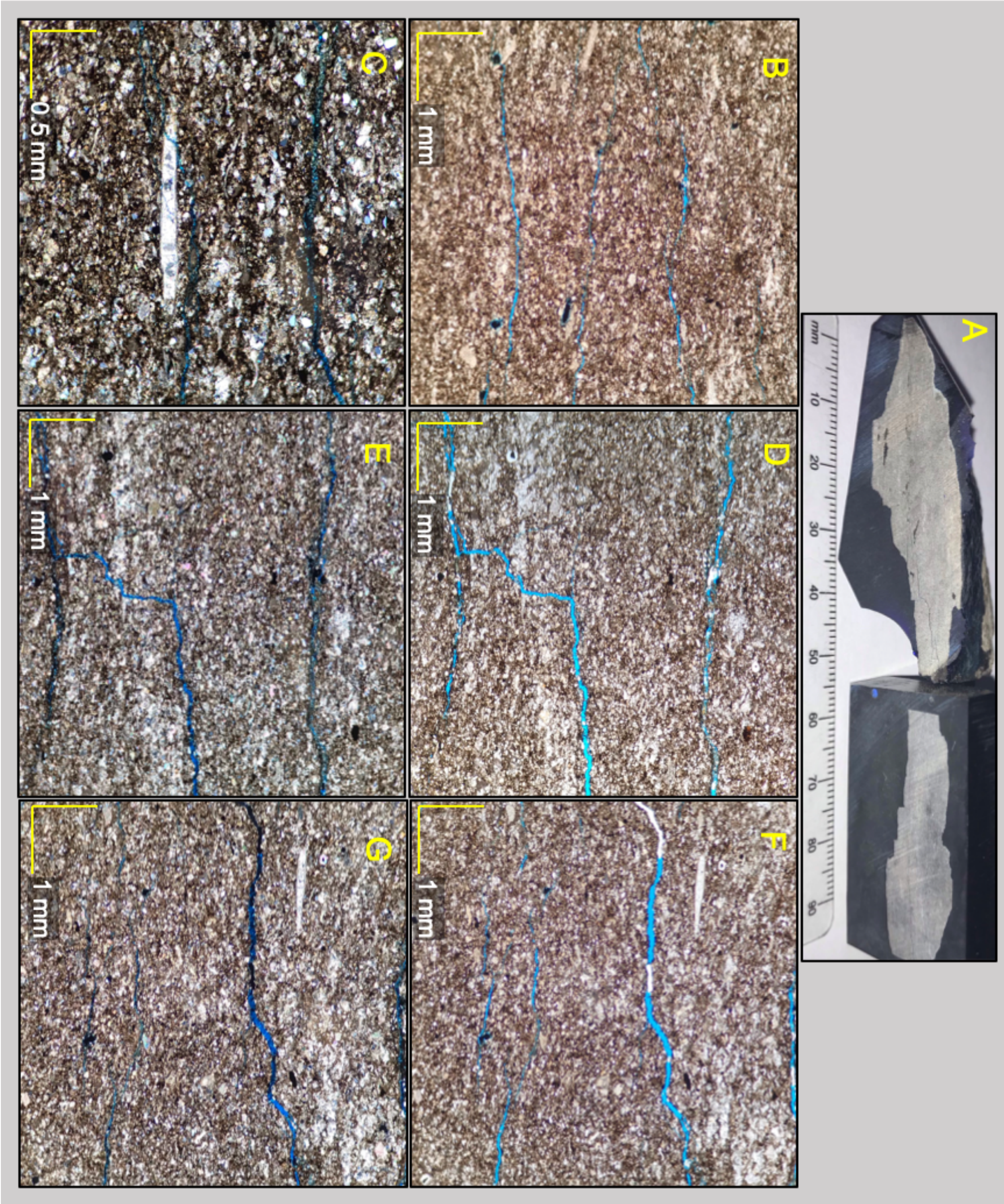

Figure 30. Petrographic analyses of sample taken at point 1D15. A) Hand sample. B) Thin section micro photograph taken in plane polarized light at 4X power. C) Thin section micro photograph taken in cross polarized light at 10X power. D) Thin section micro photograph taken in plane polarized light at 4X power. E) Thin section micro photograph D taken in cross polarized light at 4X power. F) Thin section micro photograph taken in plane polarized light at 4X power. G) Thin section micro photograph F taken in cross polarized light at 4X power.

Sample 1D15 is a grey to black limestone which is very fine-grained and well sorted. It is a thin-bedded, massive packstone and contains light grey to light tan calcite matrix and visible pyrite. Zones of high levels of calcite grains and spar which have been broken and elongated with the bedding are present, indicating the reworking of carbonate muds from the shelf into the basin. There is an abundant amount of pyrite as well as a large increase in detrital quartz, and a moderate amount of organic matter. Bioclastic fragments can be identified as deriving from echinoderms, brachiopods, bivalves, trilobites, and foraminifera. Radiolaria, sponge spicules, dolomite, intraclasts, and authigenic feldspar are also present but sparse throughout this sample. Some bioclasts are replaced with silica however the vast majority of bioclasts have calcite replacement as Figure 30 C, D, and F show. There is a moderate amount of vuggy porosity present, ranging in size from 0.1 to three millimeters in diameter, and can even be seen in hand sample (Figure 30 A). Vugs are filled with organic matter but more commonly filled with pyrite and other opaque minerals. It is also worth noting that the vugs generally have unfilled micro-porosity surrounding the original pocket of dissolution, as seen in Figure 30 A and B. The fractures in this sample are also numerous and tend to be open, ranging from hairline up to almost 0.2 millimeters openings. They tend to follow bedding planes and show stair-stepping patterns between planes, as seen in Figure 30 D and E.

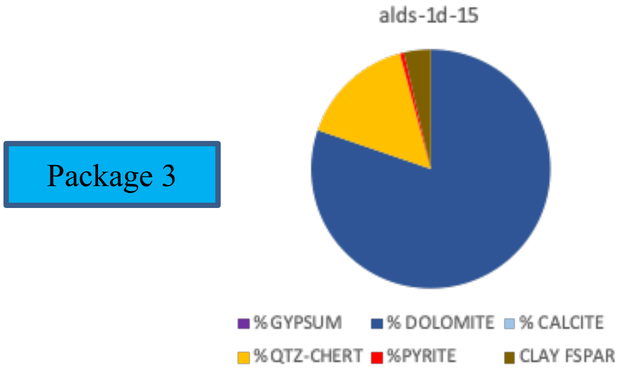

Figure 31. XRF-derived minerology and chemostratigraphic package for sample 1D-15.

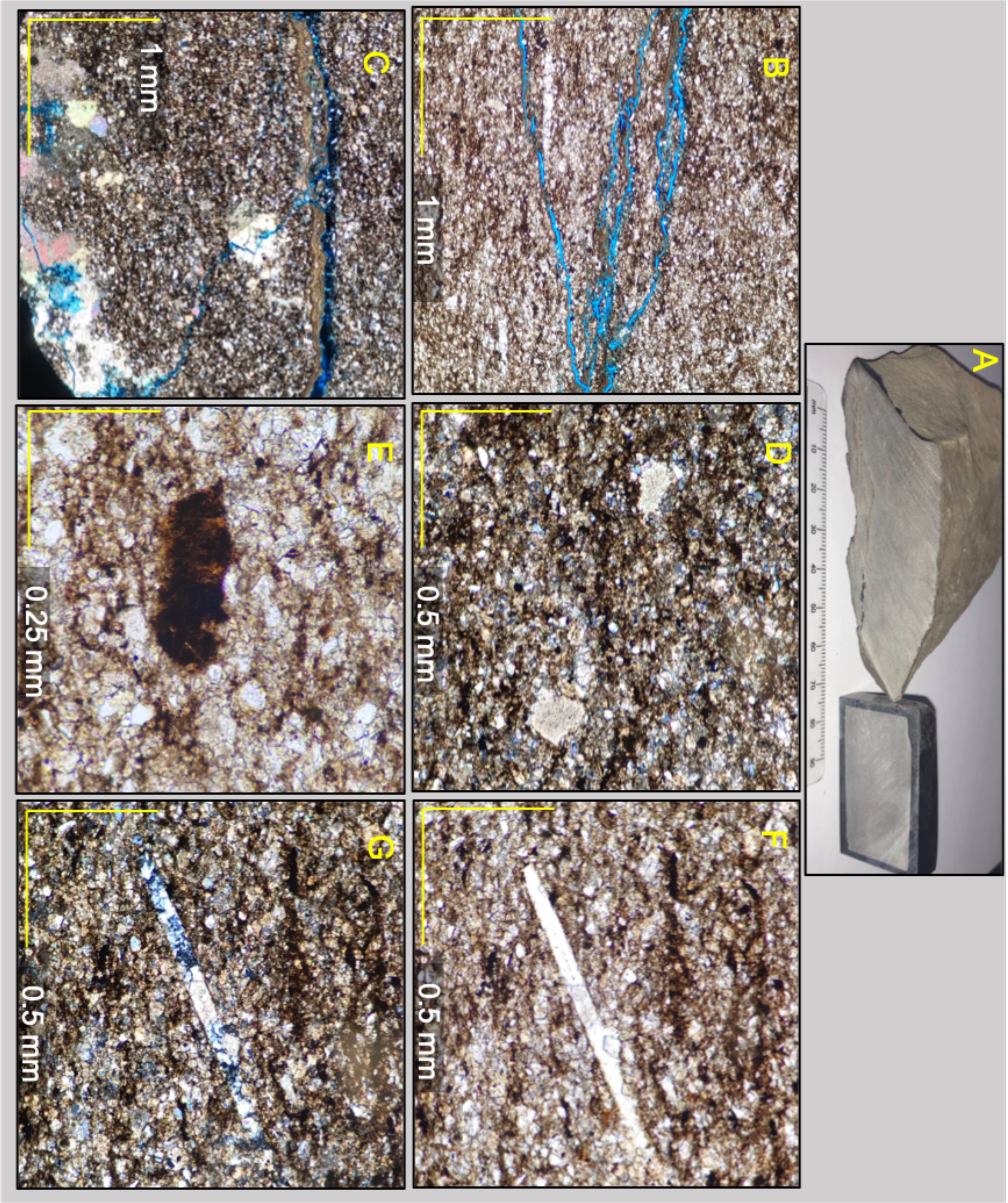

Figure 32. Petrographic analyses of sample taken at point 1D28. A) Hand sample. B) Thin section micro photograph taken in plane polarized light at 4X power. C) Thin section micro photograph taken in cross polarized light at 4X power. D) Thin section micro photograph taken in cross polarized light at 10X power. E) Thin section micro photograph taken in plane polarized light at 20X power. F) Thin section micro photograph taken in plane polarized light at 10X power. G) Thin section micro photograph F taken in cross polarized light at 10X power.

Sample 1D28 is a light tan to grey silty limestone which is very fine-grained and well-sorted. It is a massive packstone and contains light grey to light tan calcite matrix, visible pyrite, and is fractured along bedding planes in the thin bedded portion of the rock. The matrix also appears to be dolomitized in zones, as seen in Figure 32 E. There is an abundant amount of pyrite as well as a further increase in detrital quartz and organic matter. There are fewer bioclasts than previous samples, and those present tend to be heavily eroded and diagenetically altered. Bioclastic fragments can be identified as deriving from echinoderms, bivalves, and sponge spicules, as seen in Figure 32 D. Some bioclasts have calcite replacement and some are replaced with silica (chalcedony and mega-quartz) with dolomitic inclusions, as Figure 32 F and G show. The fractures in this sample are also numerous and tend to be open, ranging from hairline up to almost 0.2 millimeters openings. They are usually present in fractured zones and have minimal healing. In Figure 32 C, large calcite crystals can be seen near a fracture zone which appears to be fractured and undergoing incomplete dissolution. This indicates that these fractures could be older than the formation of these crystals, and not all factors needed for complete dissolution were present.

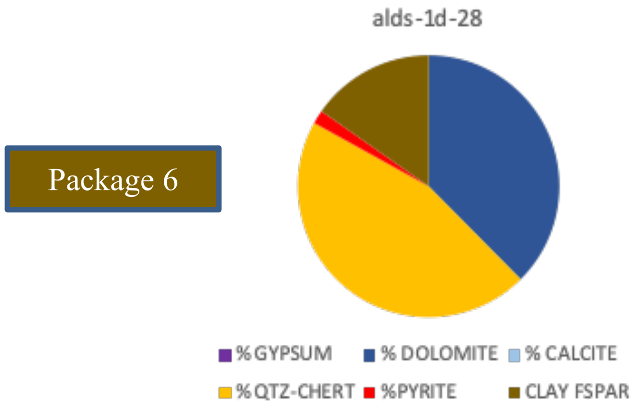

Figure 33. XRF-derived minerology and chemostratigraphic package for sample 1D-28.

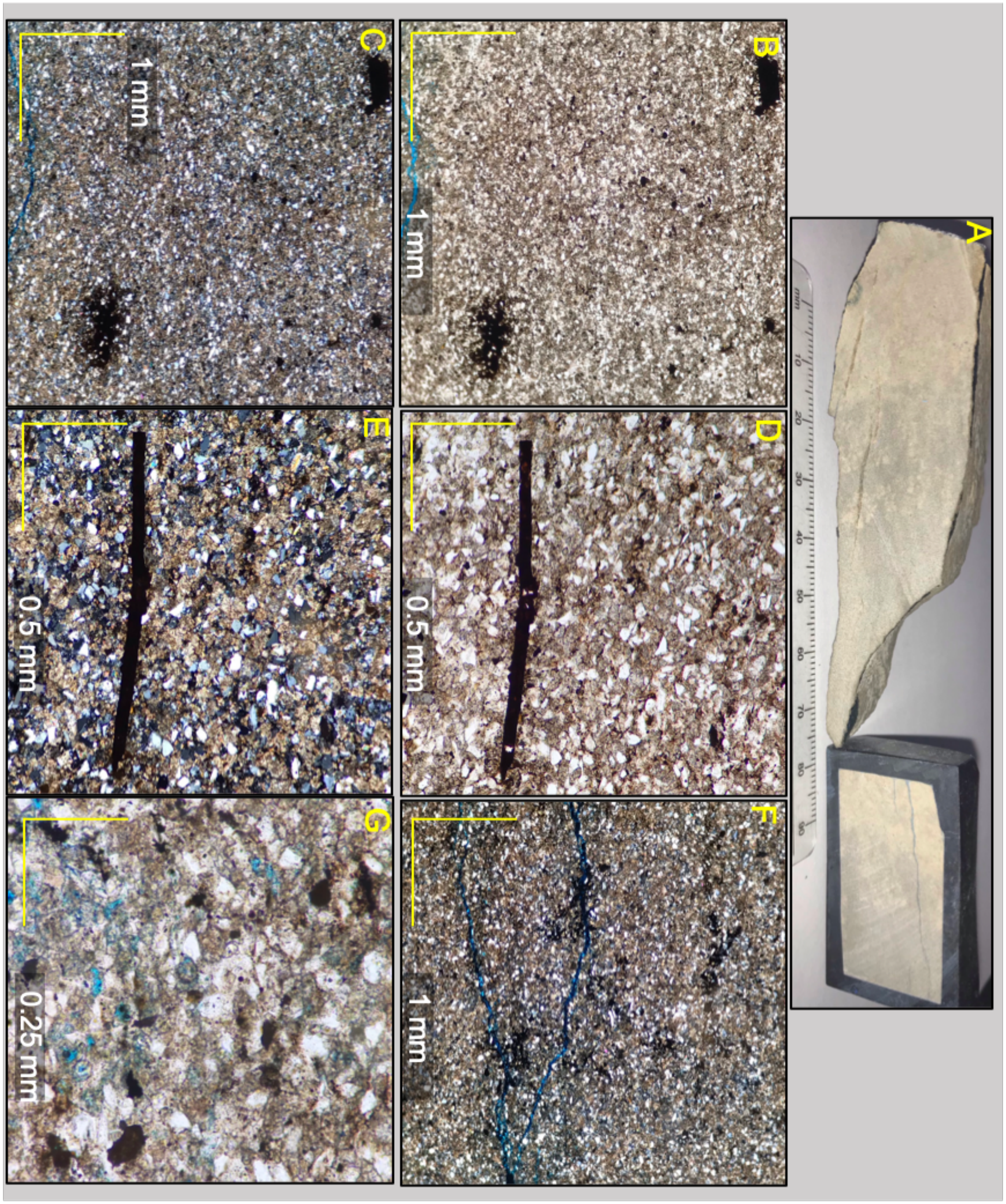

Figure 34. Petrographic analyses of sample taken at point 1D34. A) Hand sample. B) Thin section micro photograph taken in plane polarized light at 4X power. C) Thin section micro photograph B taken in cross polarized light at 4X power. D) Thin section micro photograph taken in plane polarized light at 10X power. E) Thin section micro photograph D taken in cross polarized light at 10X power. F) Thin section micro photograph taken in cross polarized light at 4X power. G) Thin section micro photograph taken in plane polarized light at 20X power.

Sample 1D34 is a light tan to grey calcareous siltstone which is very fine-grained and well-sorted. It is a massive packstone and contains light grey to light tan calcite matrix, visible pyrite, and is fractured along bedding planes in the thin-bedded portion of the rock. The matrix also appears to be partially dolomitized in some small zones. There is an abundant amount of pyrite as well as another large increase in detrital quartz and organic matter. The detrital quartz tends to be subrounded to sub-angular and moderately well sorted. There are the fewest bioclasts than any sample, and those present tend to be heavily eroded and diagenetically altered. Bioclastic fragments can be identified as deriving from echinoderms and sponge spicules, as seen in Figure 34 D. Some bioclasts have calcite replacement and some are replaced will silica (chalcedony and mega-quartz) with dolomitic inclusions, as Figure 34 F and G show. Most bioclasts, however, tend to be filled with oil, as Figure 34 B through E show. In addition, amorphous zones of micro-porosity also exist, both filled with oil or open, as seen in Figure 34 B, C, and G. The fractures in this sample are also numerous and tend to be open, ranging from hairline up to almost 0.2 millimeters openings. They are usually present in fractured zones and have minimal healing, some of which can be seen in Figure 34 F.

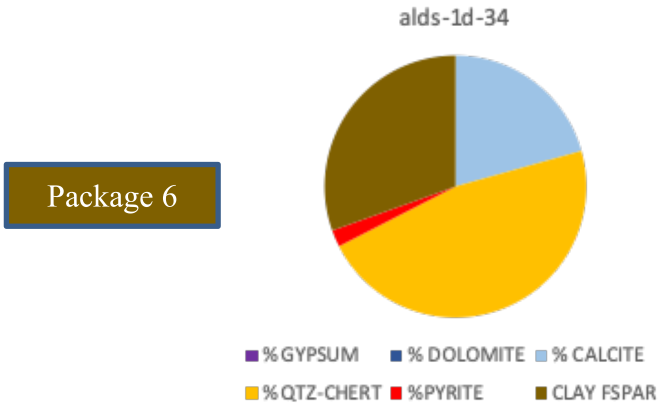

Figure 35. XRF-derived minerology and chemostratigraphic package for sample 1D-34.

5.2.3 Geochemical Proxy Results 1C-1D

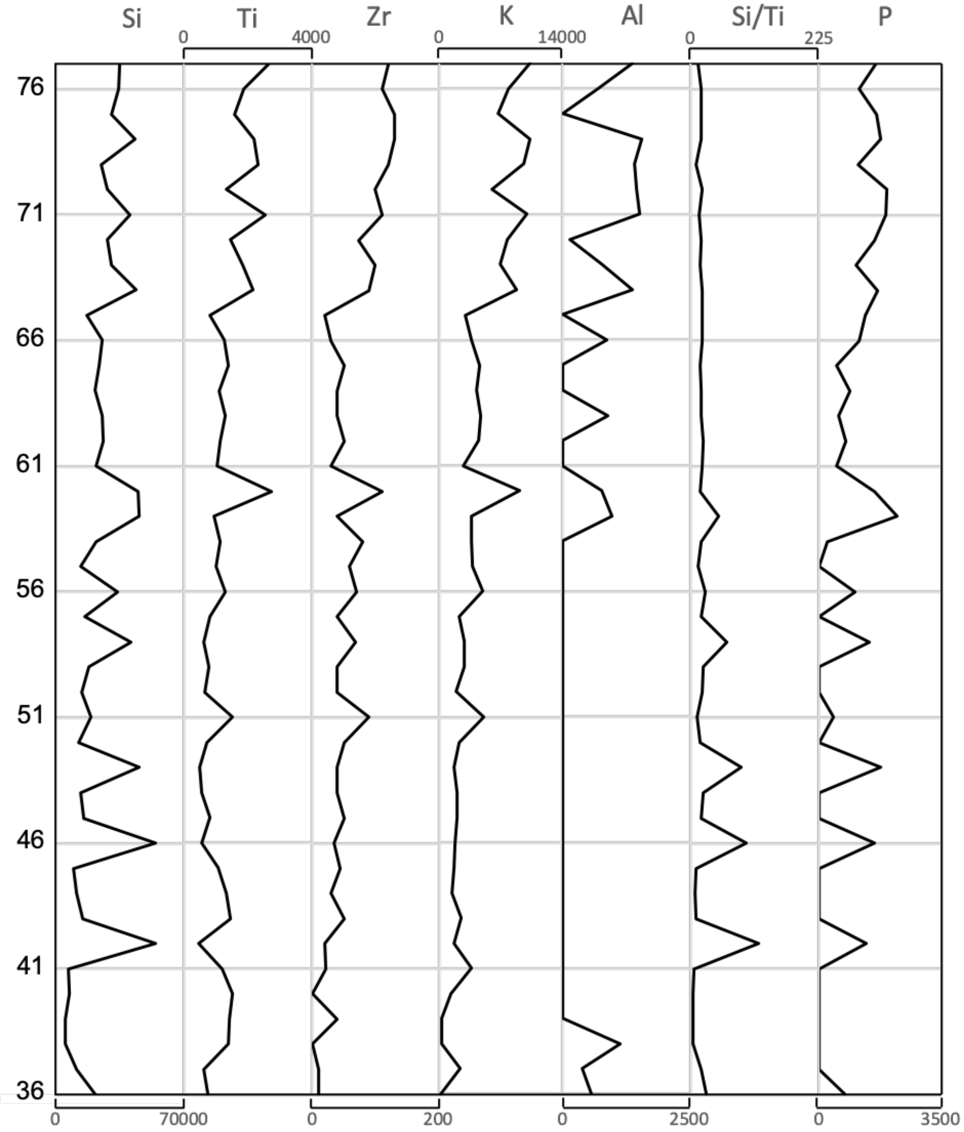

Figure 36. Siliciclastic elemental suite (ppm) for measured sections 1C-1D.

As displayed in Figure 36, Si, Si/Ti, and P show significant covariation from 36 feet up to about 59 feet, with spikes indicating biogenic, siliceous cherts in this section. Non-biogenic Si, Ti, Zr, K, and Al all show good covariation, and will serve as the main indicator of terrigenous material (Sands, silt, and clay). Since these all rise in conjunction with one another (except for Al, which does not conform until 58 feet and onward), there is an interpreted increase in all terrigenous material (sand, silt, and clay) throughout the entire section. The gap in Al detection in the lower half of the section is most likely owing to its extremely light atomic weight and difficulties in outcrop-based detection.

Owing to the steady positive gradient in siliciclastic proxies in this section, sea level will be interpreted to be in falling where proxies are increasing and in lowstand where it is steady. There is an interesting covariation between siliciclastic proxies and P, from about 59 feet to the end of the section. This covariation seems to indicate high levels of oceanic productivity in a time in which sea level was most likely falling or in low stand. This means that high stand carbonate shelf production may play a major role in basin restriction, as the increase in terrigenous material means that sea level has fallen and allowed for terrigenous material to bypass the shut off carbonate margin, and is paired with an increase in P. This increase in terrigenous material as indicated by chemostratigraphic proxies has also been shown in outcrop and in thin section as shown in previous sections.

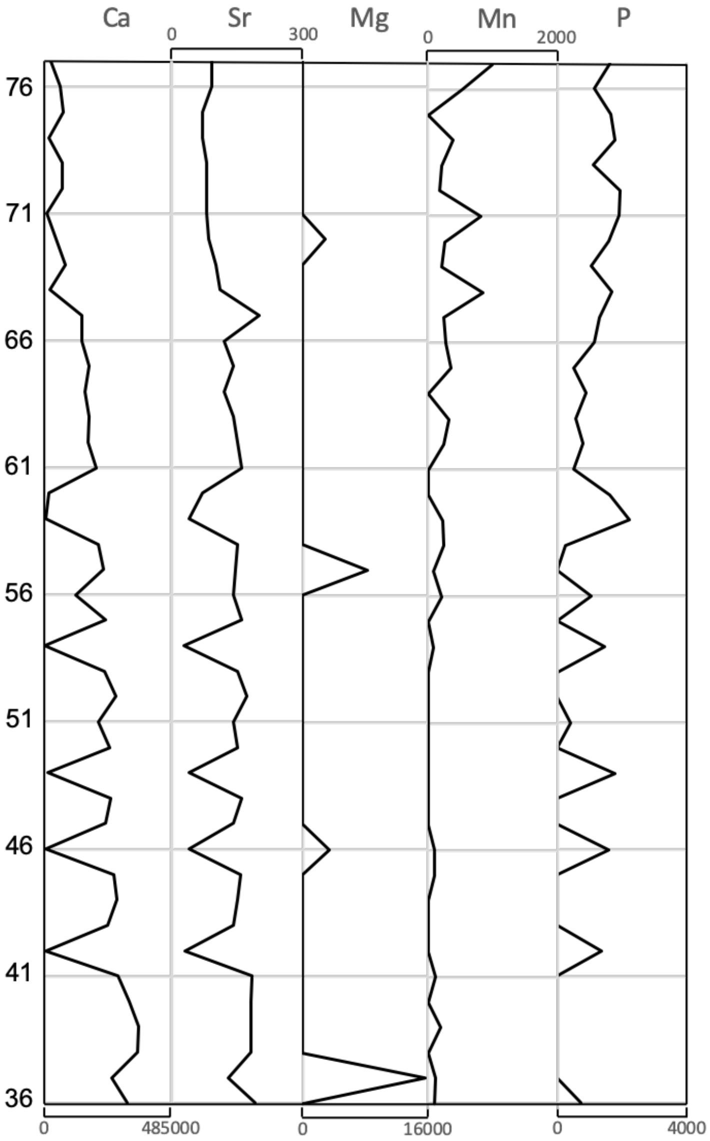

Figure 37. Carbonate elemental suite (ppm) for measured sections 1C-1D.

The carbonate elemental suite for section 1C to 1D is shown above in Figure 22. There are similar covariation trends between Ca and Sr, no covariation with Mg, and slight covariation between Mn and P. Mg again most likely shows little covariation owing to its extremely light atomic weight and difficulties in outcrop-based detection. P and in some cases, Mn can be used as identification of biogenic silicification as before, which show high negative correlation with Ca as discussed in chapter 4.1.1. However, this method is only useful up until about 59 feet, as there are much fewer biogenic cherts in this section and just some zones of a lower degree of silicification.

Ca and Sr show a constant decrease from 36 feet through the rest of the section. Since Mn is not associated with carbonates, it is most likely representative of paleoproductivity and ocean oxygenation conditions owing to its sensitivity to redox environments. Mn remains nearly around zero up until around 53 feet, where it begins a slow, upward climb. This constant, slow decrease in carbonate proxies and eventually biogenic chert abundance is characteristic of a slope environment of a regressive or low stand sea.

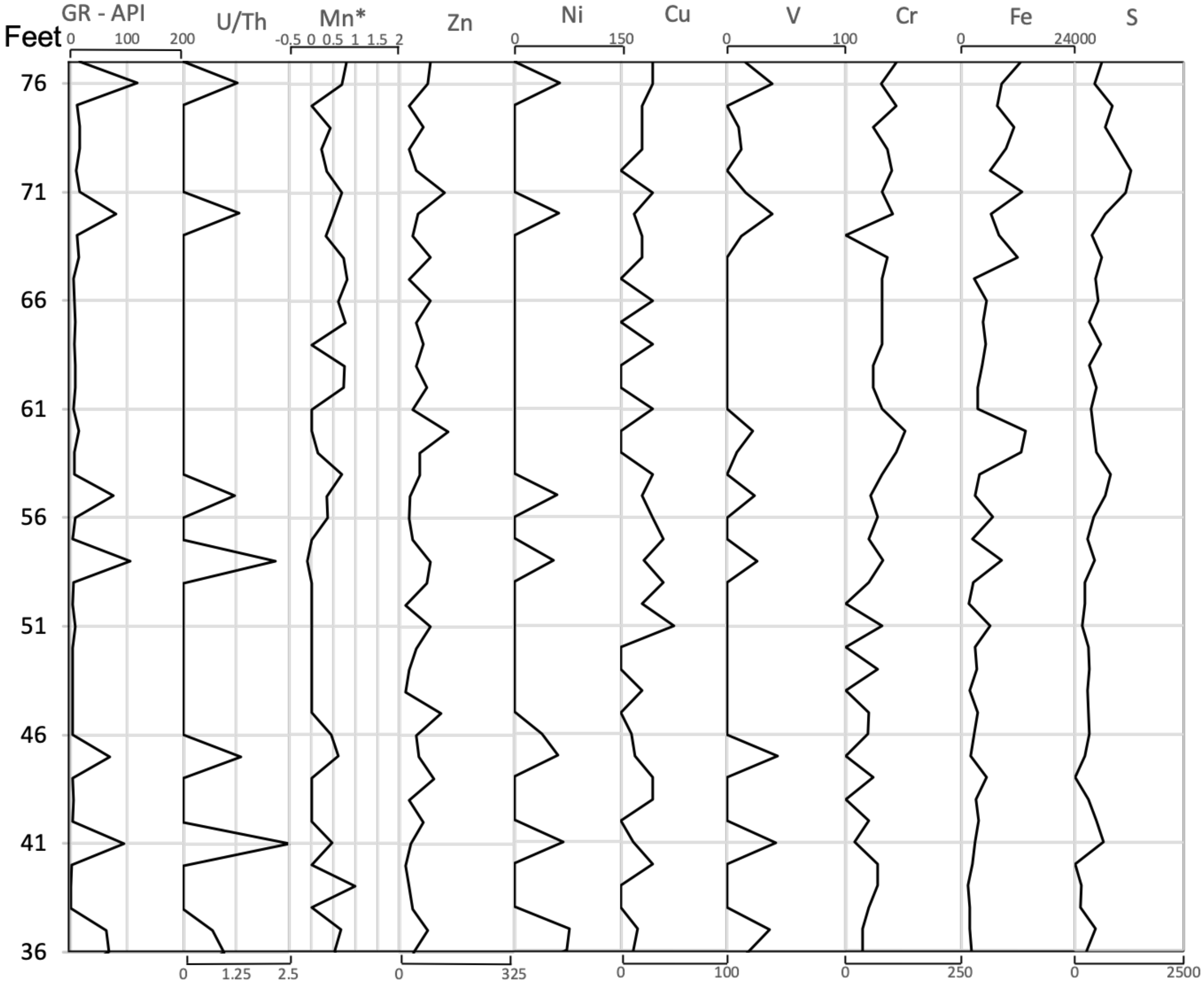

Figure 38. Redox ratios and paleoenvironmental indicators for measured sections 1C-1D. Individual elements plotted in ppm.

The redox profile shown in Figure 38 of section 1C to 1D shows good covariation between Fe, S, Cr, and Mn*. There is also minor covariation between Cu, Ni, Zn, and V. The first group (Fe, S, Cr, and Mn*) shows low stasis trend from 36 feet to about 51 feet. Then there is an increasing trend from 51 feet throughout the rest of the section, with the exception being in Mn*, which generally decreases from 69 feet through the rest of the section. The second group (Cu, Ni, Zn, and V) is mostly low and somewhat erratic throughout the section.

The pseudo gamma values that contain U and Th throughout this section are generally between 80 to 110 API. All of the points except at 36 and 37 feet, have U/Th ratios slightly above 1.25 or much higher, which is indicative to a sub-oxic to possibly anoxic environment. This is even true in some points which have generally low pseudo gamma-ray readings.

The lower levels of Mn* in this section indicate a suboxic to anoxic environment. However, the section from 47 to 53 feet Mn readings are below the limit of detection. The consistent but low levels of Zn, Ni, and Cu suggests low to medium levels of organic matter input and less sequestering within syn-depositional pyrite. The pyrite can be seen in thin section and is described in the previous section, and owing to the lack of correlation with Zn, Ni, and Cu may be diagenetic.

5.3 XRF-Derived Lithology

5.3.1 XRF-Derived Lithology – North Wall

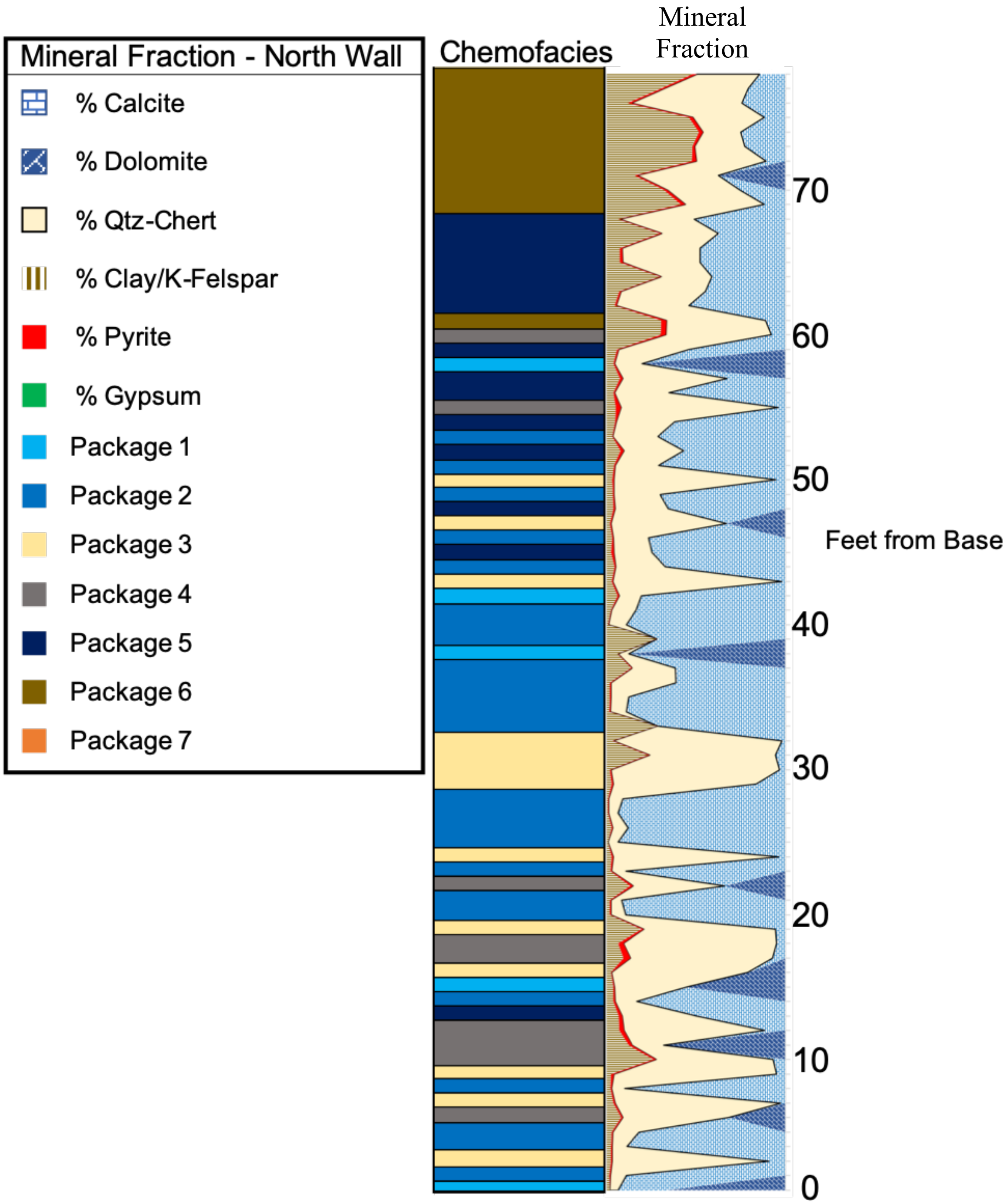

Figure 39. This figure shows the XRF derived minerology curve on the right compared to the chemofacies on the left of the combined measured sections 1A to 1D, which represent the North Wall sections shown in Figure 7. The legend on the far left shows which colors correspond to which mineral or chemofacies package.

Figure 39 shows the results from the cluster analyses on the left and the results for the major mineralogy percentages on the right under lithology. This displays the transition from cleaner carbonate with high chert abundance to a mixed carbonate and ultimately to the calcareous siltstone. Another purpose of this display is to help visualize which lithofacies are associated with each chemofacies package. This section shows consistent pairing of packages one and two with clean, high percentage calcite (clean carbonate), while package five shows a correlation with mixed calcite, silicates, and clays. Package six shows a strong association with high clay mineralogy with mixed siliceous and calcite material, and packages three and four correlate with very high silicates representing cherts.

5.4 Stratigraphic Section 2A-2B

5.4.1 Outcrop Characteristics 2A-2B

This section shows Section 2A, shown in Figure 40, and contains just six measurements each about one foot apart in the true vertical direction of the E-SE dipping beds. It is found on the south wall along the Shumard trail, a few hundred feet further into the canyon as shown in Figure 7. There are three main lithofacies in this section. The first is a thick-bedded, black and light tan to light grey bioclastic limestone which is very fine-grained and moderately sorted with thick laminations which are slightly rippled but mostly planar, and alternate between un-silicified and silicified packstone and minor interbedded wackestone. The second is a thin-bedded, dark grey, very fine-grained, moderately sorted wackestone/packstone with varying degrees of silicification and cherts. The third is a thick-bedded, light grey to black, moderately sorted, wackestone/packstone with very high levels of chert. In addition to bed thickness, beds tend to alternate between massive, parallel laminated, low amplitude ripple laminated, and deformed (soft-sediment deformation).

Figure 40 below shows a complicated series of erosion and deposition, indicating a potential change in slope steepness and/or proximity to the shelf. The beds at the base consist of the alternating thick and thin-bedded black and light tan to light grey limestone which is very fine grained and moderately sorted, with at least one erosional surface at the base. Directly below the rock hammer there are multiple beds that show multiple rapid depositional pulses which tend to erode the unit beneath it, which the first solid white line from the base shows. To the right of the rock hammer, discordant beds can be found with what appears to be a slump feature or similar MTD. All of these beds are then cut by the sloped erosive surface, followed by deposition along this newly inherited topography. The solid white line at the top indicates erosion and deposition of the original lithofacies, characterized by an increase in resistance and a sharp, flat erosive contact.

Figure 40. Outcrop photograph showing measured section ALDS 2A. Note the heavy erosion surfaces in the center of the photo with rock hammer for scale, with erosional surfaces marked by white dashed lines. The solid white lines mark facies change coupled with an erosive surface.

Figure 41. Outcrop photograph showing measured section ALDS 2B. Note the large slide/slump feature topped by discordant beds interpreted in white. This is characteristic of the cutoff formation and an indication that slope gradient has increased or distance to the shelf has decreased.

Figure 41 shows Section 2B and contains 11 measurements each about one foot apart in the true vertical direction of the E-SE dipping beds. It is found on the south wall along the Shumard trail and is a continuation of section 2A. There are the same three main lithofacies in this section, however with significant levels of deformation. In addition to bed thickness, beds tend to alternate between massive, parallel laminated, low amplitude ripple laminated, and rare deformed (soft-sediment deformation). There remains an abundance of lensed to layered siliceous chert as well, of similar characteristics as before, mostly within the limestone beds.

Starting at the base in section 2B, the dominate thick beds of black and light tan to light grey limestone which is very fine-grained and moderately sorted, with thick laminations which are slightly rippled but mostly planar, and alternate between un-silicified and silicified packstone and minor interbedded wackestone return, up until the major erosional surface marked by the first solid white line. This erosion was caused by the massive MTD feature above, and most likely a result of slumping. This feature is indicative of the steepening of the slope or increased proximity to the shelf, or a combination of both. The contorted beds show evidence that this MTD is actually comprised of the same lithofacies with serious deformation, as expected in large slumps. The second white line upward marks a second major erosional surface where hummocky MTD beds are found truncated against the slump feature. These beds show signs of similar failure mechanisms as the feature below and are of similar lithofacies. Above this lies another erosional surface followed by the third and final slump feature in this outcrop. Its height is too great for accurate sampling; however, it seems to follow a similar form as the first MTD. The stratigraphic features of sections 2A-B are further detailed in the stratigraphic column below in Figure 42.

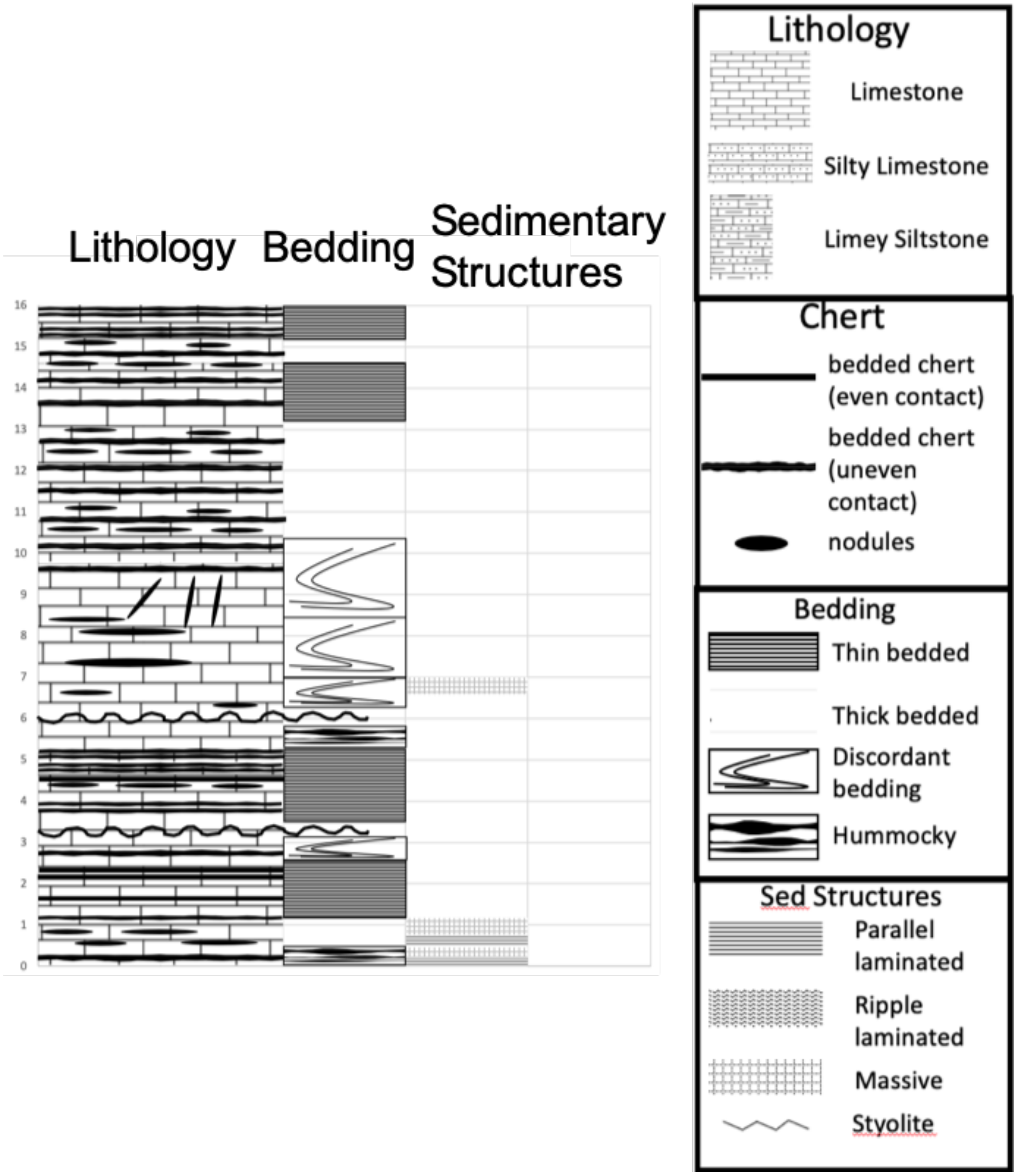

Figure 42. Combined stratigraphic section of ALDS 2A to 2B of the South Wall shown in Figure 7. Note the apparent sharp contact unconformities marking the slump/slide feature and the above discordant beds.

5.4.2 Petrographic Analyses 2A-2B

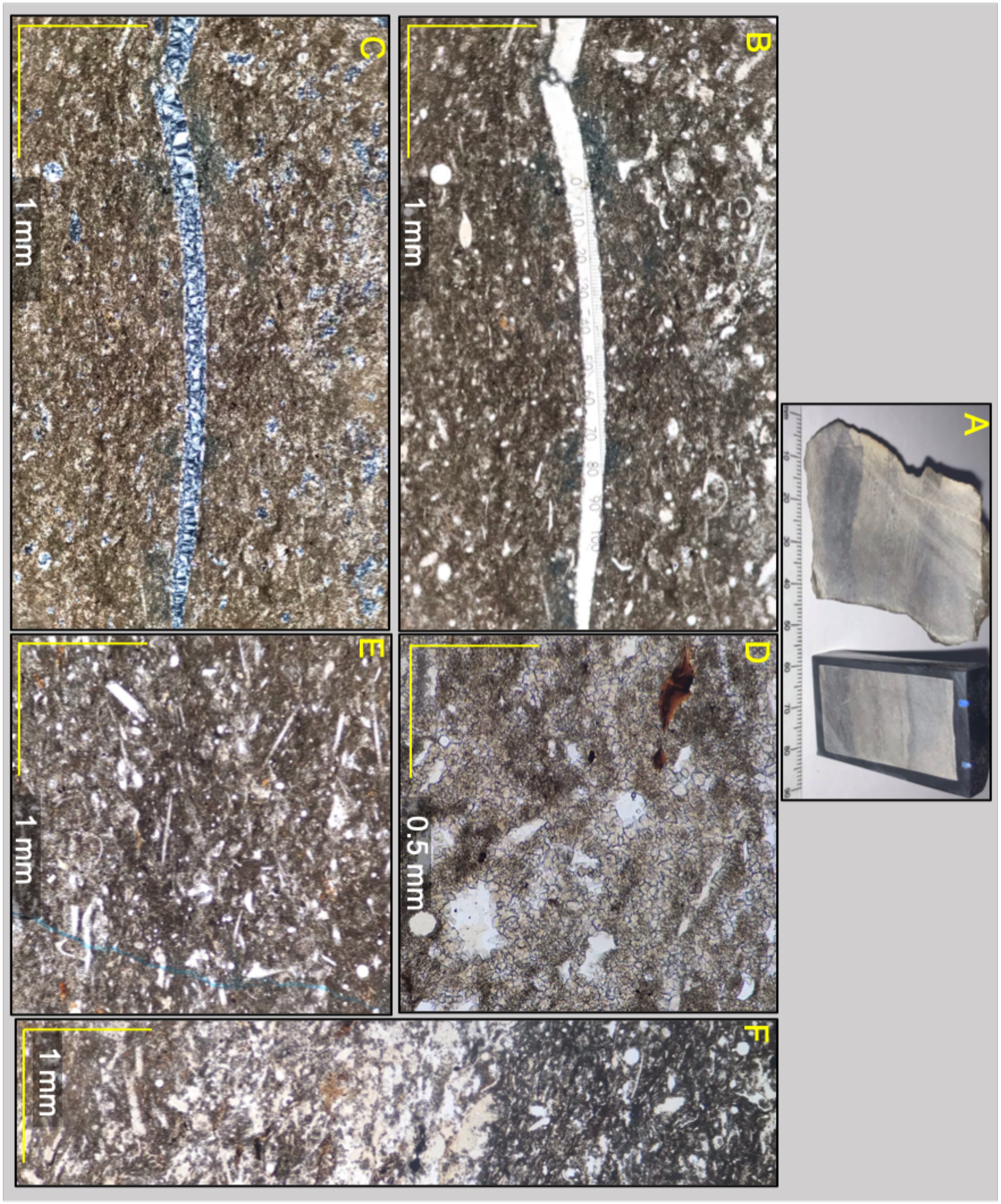

Figure 43. Petrographic analyses of sample taken at point 2A1. A) Hand sample. B) Thin section micro photograph taken in plane polarized light at 4X power. C) Thin section micro photograph B taken in cross polarized light at 4X power. D) Thin section micro photograph taken in plane polarized light at 10X power. E) Thin section micro photograph taken in plane polarized light at 4X power. F) Thin section micro photograph taken in plane polarized light at 4X power.

Sample 2A1 is a black and light tan to light grey limestone which is very fine-grained and moderately sorted. Thick laminations are slightly rippled but mostly planar, and alternate between un-silicified and silicified packstone and minor interbedded wackestone. In addition to the high levels or zones silicification, there is a very high level of dolomitization which mostly increases in the silicified zones, but persists throughout, as seen in Figure 43 D and F. There is a visible change in matrix composition vertically as seen in Figure 43 F, which is most likely an increase in organic matter or clay. There are numerous bioclasts and high levels of radiolaria and spicules present to supply biogenic silica for silicification, which can be seen throughout Figure 43, especially in E. These constituents, in addition to the bioclasts, are generally completely replaced with silica as micro quartz and chalcedony, with dolomite inclusions, as can be seen in the large bivalve shell fragment in Figure 43 B and C. Bioclastic fragments which can be identified as deriving from echinoderms, brachiopods, gastropods, bivalves, trilobites, foraminifera, radiolaria, and sponge spicules. There are moderate levels of organic matter and vertical natural hairline fractures throughout the rock, and a few zones of open micro-porosity which can be seen in Figure 43 B and C near the brake in the bivalve shell. There is little to no detrital silica and low levels of pyrite.

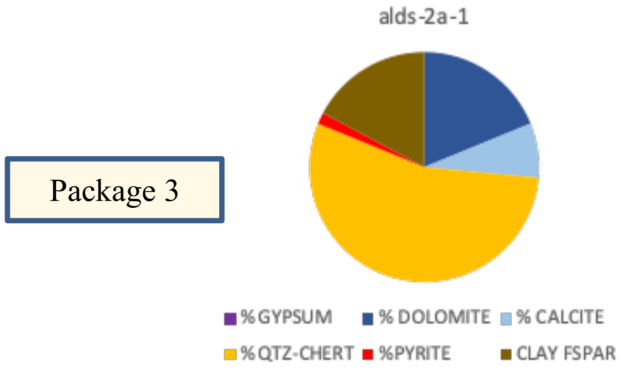

Figure 44. XRF-derived minerology and chemostratigraphic package for sample 2A-1.

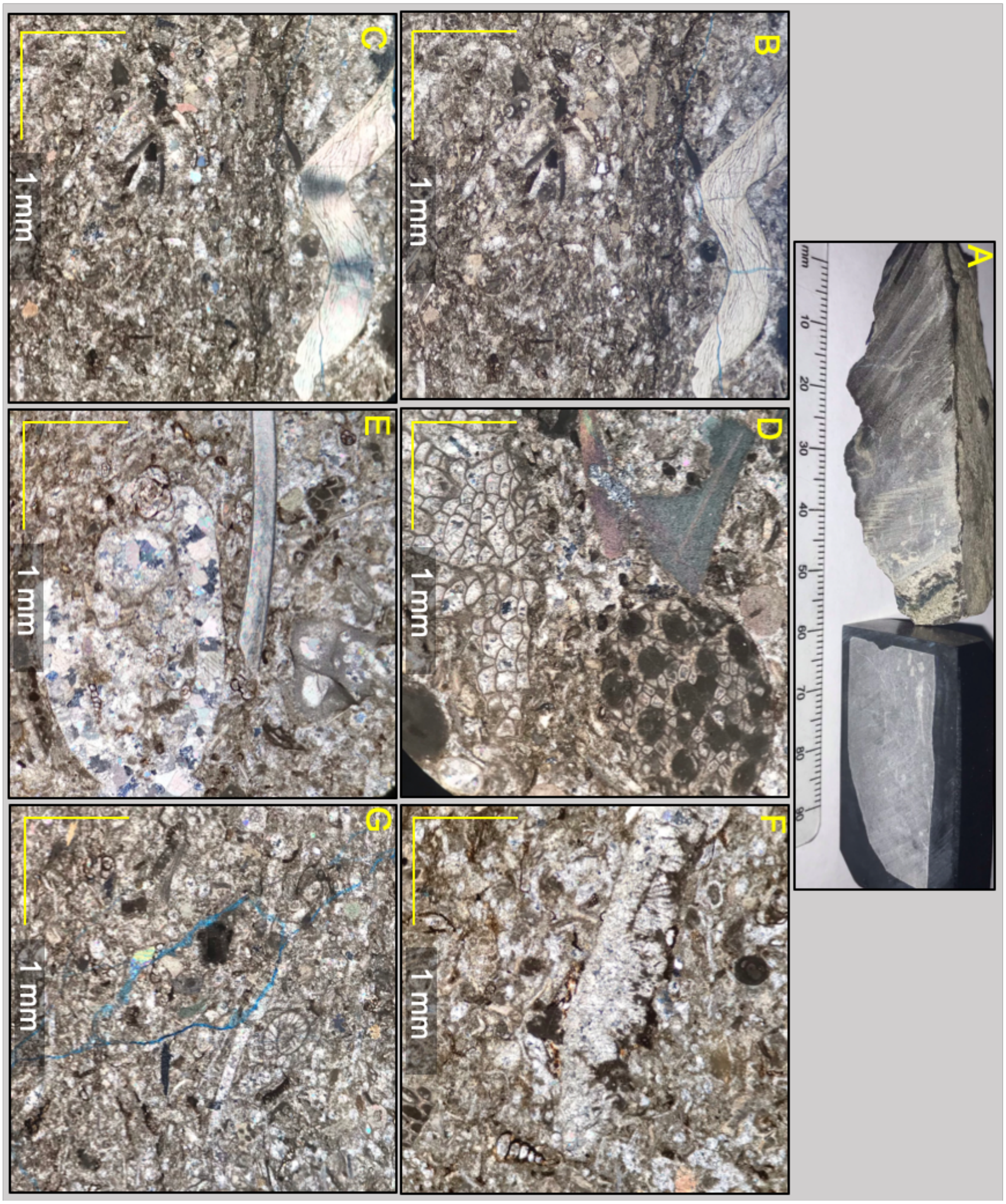

Figure 45. Petrographic analyses of sample taken at point 2B2. A) Hand sample. B) Thin section micro photograph taken in plane polarized light at 4X power. C) Thin section micro photograph B taken in cross polarized light at 4X power. D) Thin section micro photograph taken in cross polarized light at 4X power. E) Thin section micro photograph taken in cross polarized light at 4X power. F) Thin section micro photograph taken in cross polarized light at 4X power. G) Thin section micro photograph taken in cross polarized light at 4X power.

Sample 2B2 is a massive, black limestone with light grey bioclasts, very fine-grained, moderately to poorly sorted, and fractured. It is a packstone to a grainstone and has a crystalline calcite matrix, and its bioclasts range from very fine-grained to pebble size. There is a very high level of bioclastic fragments that can be identified as deriving from bryozoans, echinoderms, brachiopods, bivalves, trilobites, foraminifera, fusulinids, gastropods, and potentially some corals, a few spicules and little to no radiolaria. These range from partially preserved to completely replaced by calcite spar. There is a low to moderate amount of intraclasts, organic matter, styolites, and natural fractures and throughout the rock. Some of the fractures are through-going such as the one in Figure 45 G, or just intragranular, as seen in the large trilobite fragment in Figure 45 B and C. The organic matter can be found surrounding bioclast moulds, within styolites, or scattered through the rock, as seen in Figure 45 B, C, and F. There are very few to no detrital silica grains, pyrite, ooids, or dolomite present in the sample.

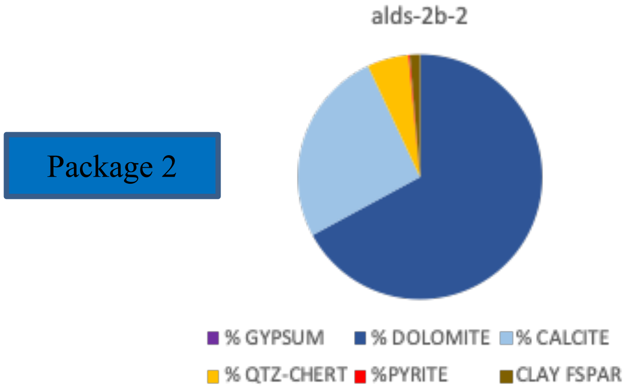

Figure 46. XRF-derived minerology and chemostratigraphic package for sample 2B-2.

5.4.3 Geochemical Proxy Results 2A-2B

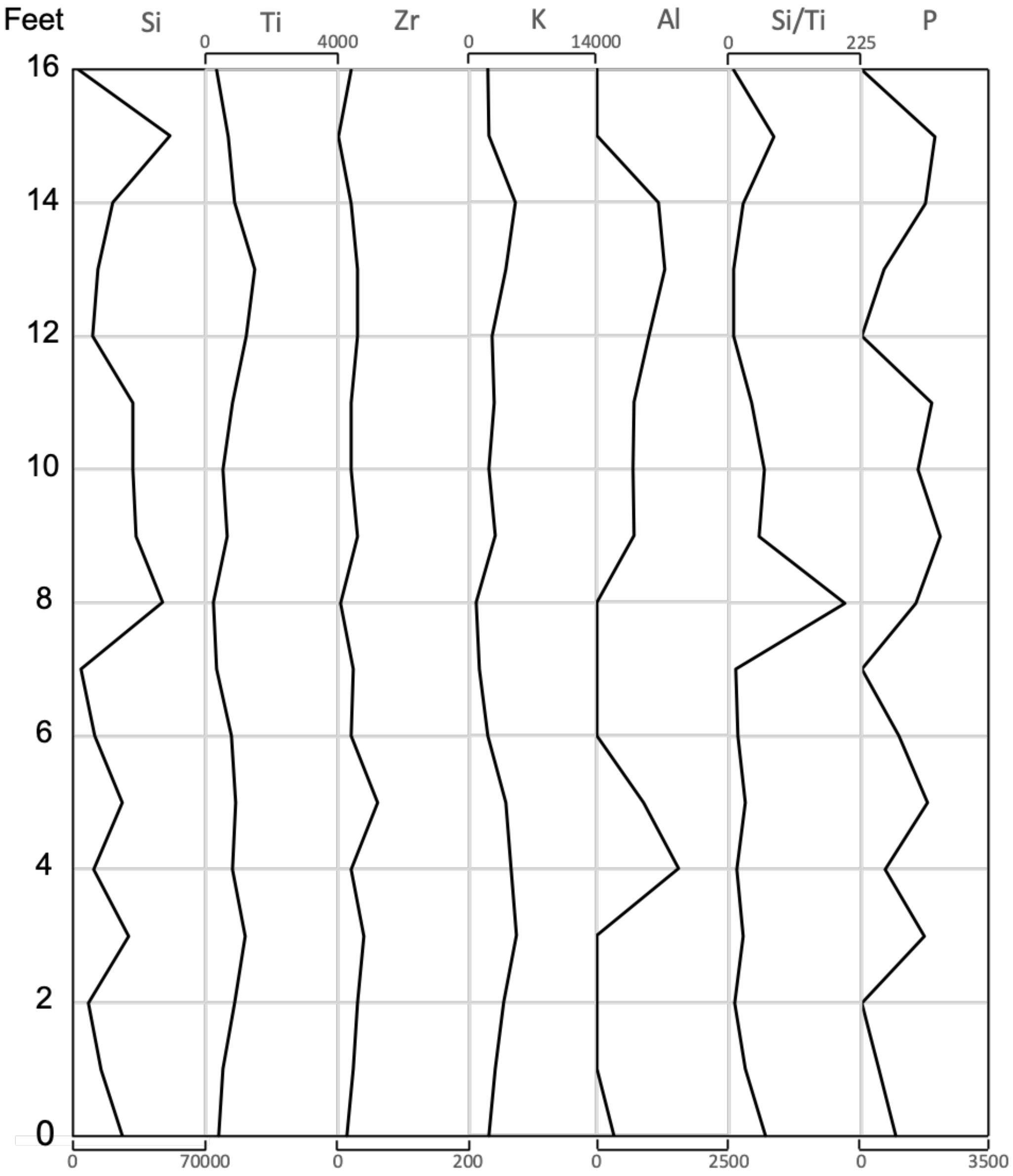

Figure 47. Siliciclastic elemental suite (ppm) for measured sections 2A-2B.

As displayed in Figure 47, Si, P, and where conditions are right Si/Ti, shows good covariation, indicating that trends in silica must be interpreted with caution due to the large abundance of biogenic, siliceous cherts in this section. Ti, Zr, K, Al show decent covariation and will serve as the main indicator of terrigenous material (Sands, silt, and clay). Most spikes in Si can be attributed to biogenic chert; however, as thin section evidence has shown, some units show zones of partial silicification to varying degrees, in either non-structured zones or along bedding planes. This can be seen in data points where there are both medium levels in silica and calcite, or with low to medium Si/Ti spikes.

There is a subtle increase in terrigenous proxies (Ti, Zr, K, and Al) from about Zero feet to about four feet, followed by a decrease up until eight feet. This terrigenous signal is followed by another increase up until about 14 feet, then a decrease through the rest of the section. Siliciclastic proxies remain relatively low to the median in this section and do not show significant relative swings in either direction. These levels of terrigenous proxies indicate potential sea level highstand with some possible sediment bypassing for terrigenous material to be delivered from the intracratonic environment. However, in knowing that the depositional mechanisms in this section are in large part owing to slumping and similar mass transport deposits, it is possible to have a mixing of disturbed sediments from other areas.

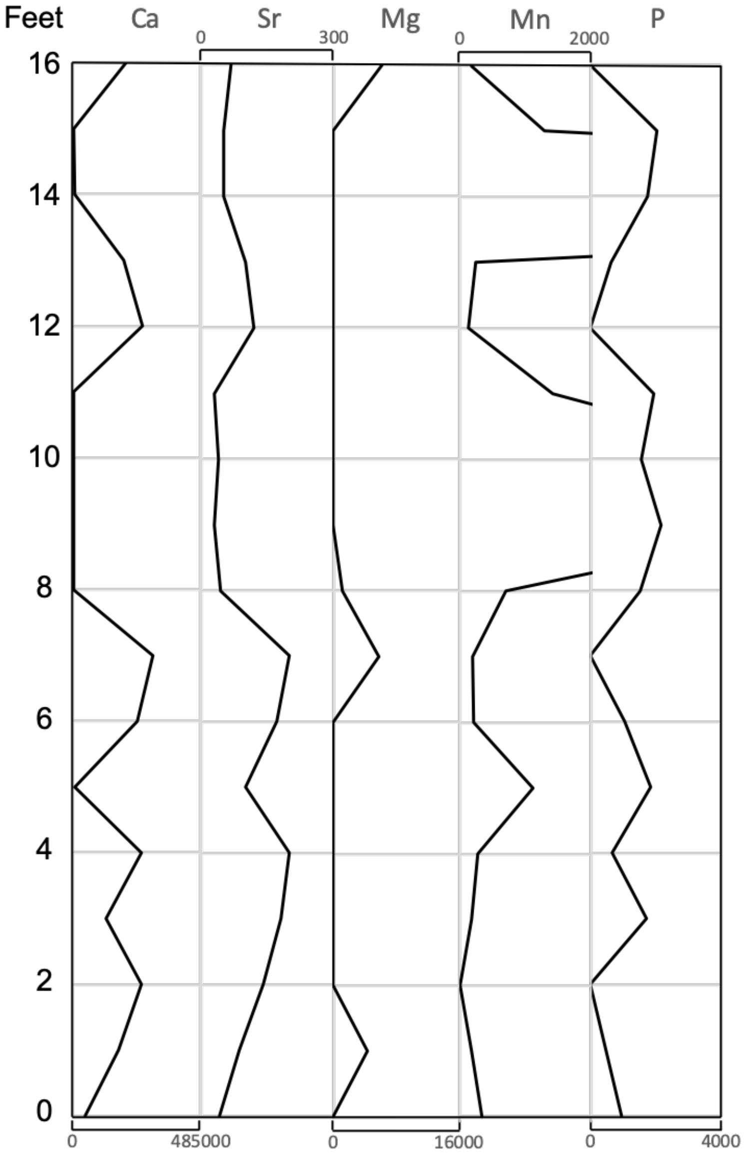

Figure 48. Carbonate elemental suite (ppm) for measured sections 2A-2B.

In section 2A to 2B there is good covariation between Ca and Sr, no covariation with Mg, and slight covariation between Mn and P, as shown in Figure 48 above. Mg most likely shows little covariation owing to its extremely light atomic weight and difficulties in outcrop-based detection. P and in some cases Mn can be used as identification of biogenic silicification with caution. Since Mn is not associated with carbonates, it is most likely representative of paleoproductivity and ocean oxygenation conditions owing to its sensitivity to redox environments.

Peaks in Ca and Sr show a very subtle increase and eventually leveling out from zero feet to seven feet, and then a subtle decrease from 12 feet to 16 feet. This is somewhat inverse of the general siliciclastic trends, but with some overlap. Overall, these relatively median carbonate proxies in this section do not show significant relative swings in either direction. These levels of terrigenous proxies indicate potential sea level highstand with some possible sediment bypassing for terrigenous material to be delivered from the intracratonic environment. However, this compositional mixing also supports the idea that there is mixing and resettling of sediments disturbed from chaotic slumping or other forms of up-slope mass transport.

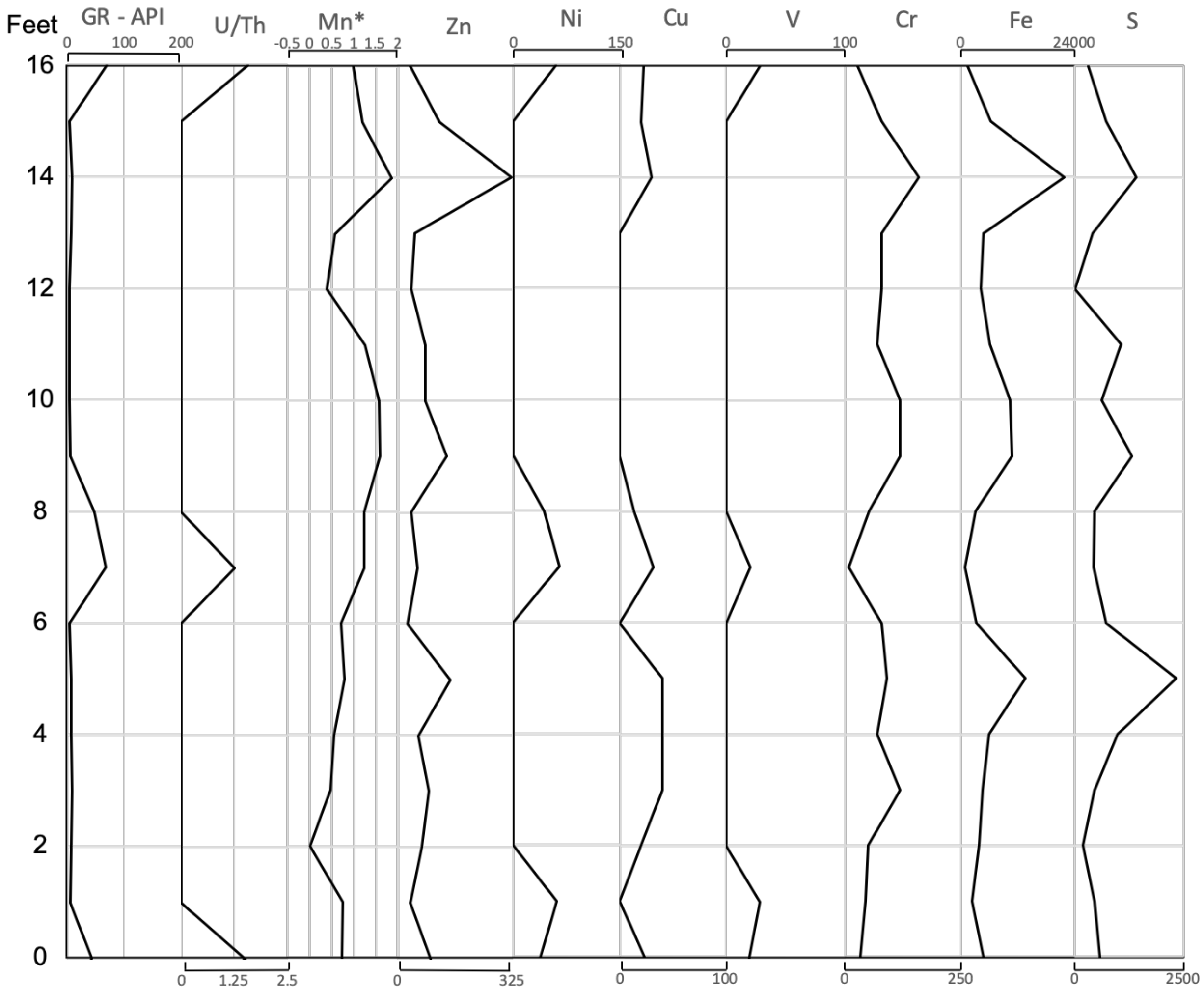

Figure 49. Redox ratios and paleoenvironmental indicators for measured sections 2A-2B. Individual elements plotted in ppm.

Figure 49 above shows the redox profile of section 2A to 2B, displaying good covariation between Fe, S, Cr, and Zn. There is also minor covariation between Cu, Ni, V. The first group (Fe, S, Cr, and Zn) shows a low but increasing profile from zero feet until the large spike at five feet. The trends are then generally low throughout the section except for the elevated levels from about nine to 11 feet and again at 14 feet. The second group (Cu, Ni, and V) mostly shows similarities at zero, seven to eight, and 16 feet. Ni and V are nearly identical throughout the whole section, while copper contains slightly more data at one to five feet and at 14 to 15 feet.

Mn* does not show significant covariation except at a few points. There is a generally increasing trend from zero to ten feet from about zero to 1.5, followed by a drop back to around 0.3 from 10 to 12 feet. It increases through the rest of the section, with a large spike at 14 feet.

The pseudo gamma values that contain U and Th throughout this section are generally between 50 to 85 API. U/Th ratios at zero and 16 feet are slightly above 1.25, and just at 1.25 at seven feet, which is indicative of a sub-oxic to possibly anoxic environment. The inconsistent and low levels of Zn, Ni, and Cu suggests low to medium levels of organic matter input, except for large spikes at seven and fourteen feet. There are consistent levels of Fe and S suggesting pyrite, which can be confirmed in the thin section and is described in the previous section, but it is sparse.

5.5 XRF-Derived Lithology

5.5.1 XRF-Derived Lithology – South Wall

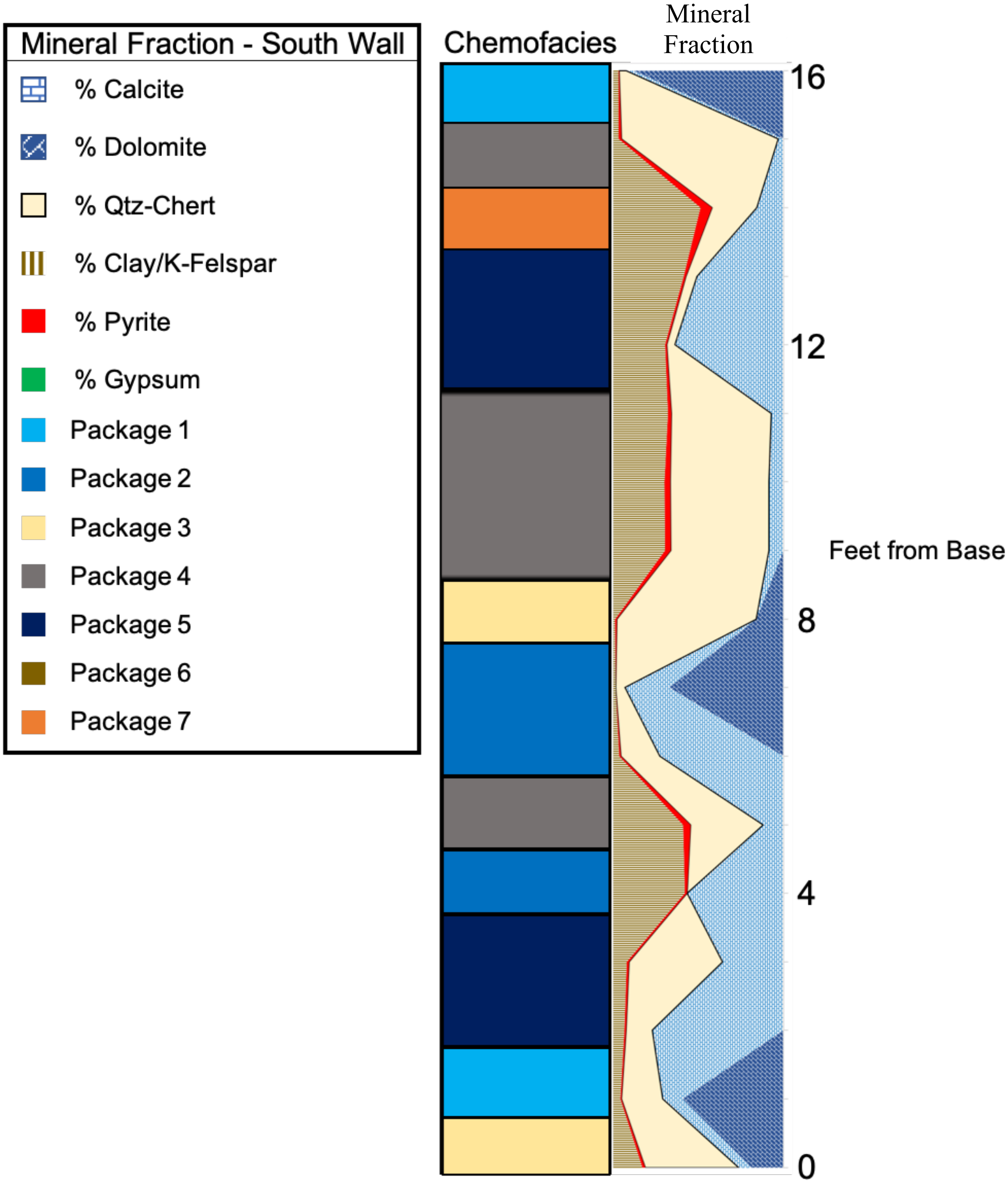

Figure 50. This figure shows the XRF derived minerology curve on the right compared to the chemofacies on the left of the combined measured sections 2A to 2B of the South Wall, as shown in Figure 7. The legend on the far left shows which colors correspond to which mineral or chemofacies package.

Figure 50 shows the results from the cluster analyses on the left and the results for the major mineralogy percentages on the right under lithology. This displays a more chaotic stratigraphic section than what is seen in section one. There is still a similar consistent pairing of packages one and two with clean, high percentage calcite (clean carbonate), and package five shows a correlation with mixed calcite, silicates, and clays. Package six shows a strong association with high clay mineralogy with mixed siliceous and calcite material, and packages three, four, and seven correlates with very high silicates representing cherts.

5.6 Chemofacies Characterization

5.6.1 Characterization by Package

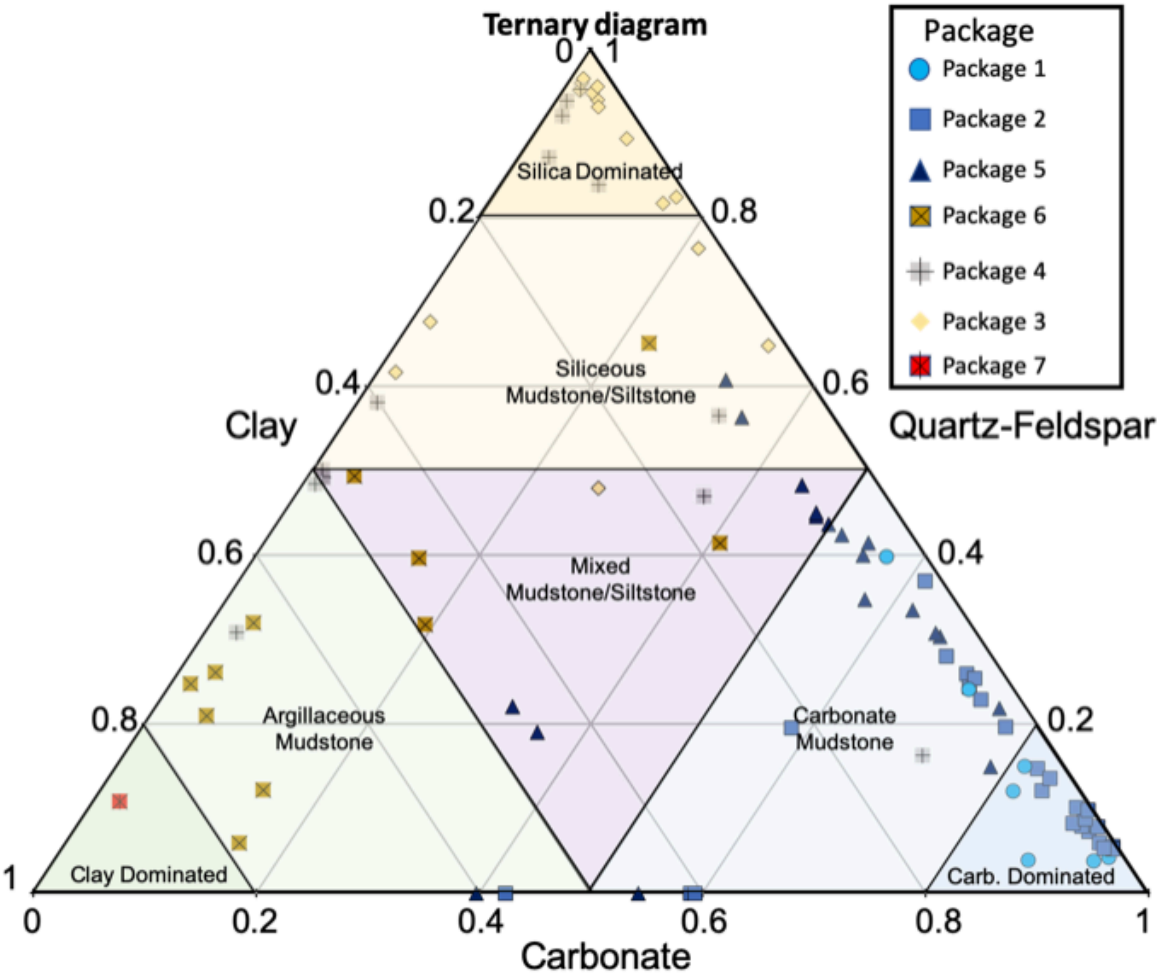

Figure 51. Ternary diagram of quartz-feldspar (right side), clay (left side), and carbonate (bottom). The legend on the upper right-hand side shows the symbols which represent each package.

Plotting each sample in a ternary diagram between percent quartz-feldspar, percent clay, and percent carbonate and marking each by its respective chemostratigraphic package can reveal a lot of insight to the lithologic composition about both the samples and each package. Figure 51 shows the close grouping of packages one, two, and five, all with zero to 60 percent quartz-feldspar, 35 to 98 percent carbonate, and zero to 60 percent clay. However, package five tends to have lower levels of carbonate and higher levels of quartz-feldspar than packages one and two and can be seen distinctively grouped accordingly higher in the diagram. Lastly, packages six and seven have about 50 to 90 percent clay (except two outliers at about 18 percent clay), two to 25 percent carbonate, and five to 55 percent quartz-feldspar.

Packages three and four represent cherts and heavily silicified units and show very high levels of quartz-feldspar and variable levels of carbonate and clay. Package four shows a much higher variation in these categories and therefore may not always be pure chert, but rather a heavily silicified unit. The higher the position on the ternary diagram (the higher quartz-feldspar values), the higher the degree of silicification that took place. There are three main clusters of group four, one located closer to the carbonates, one located closer to the clays, and one located with the purer quartz-feldspars. It is assumed that each clusters location is representative of the original lithology before silicification took place, except for the group in the high quartz-feldspar zone, where a petrographic analysis would be necessary to discern original lithology.

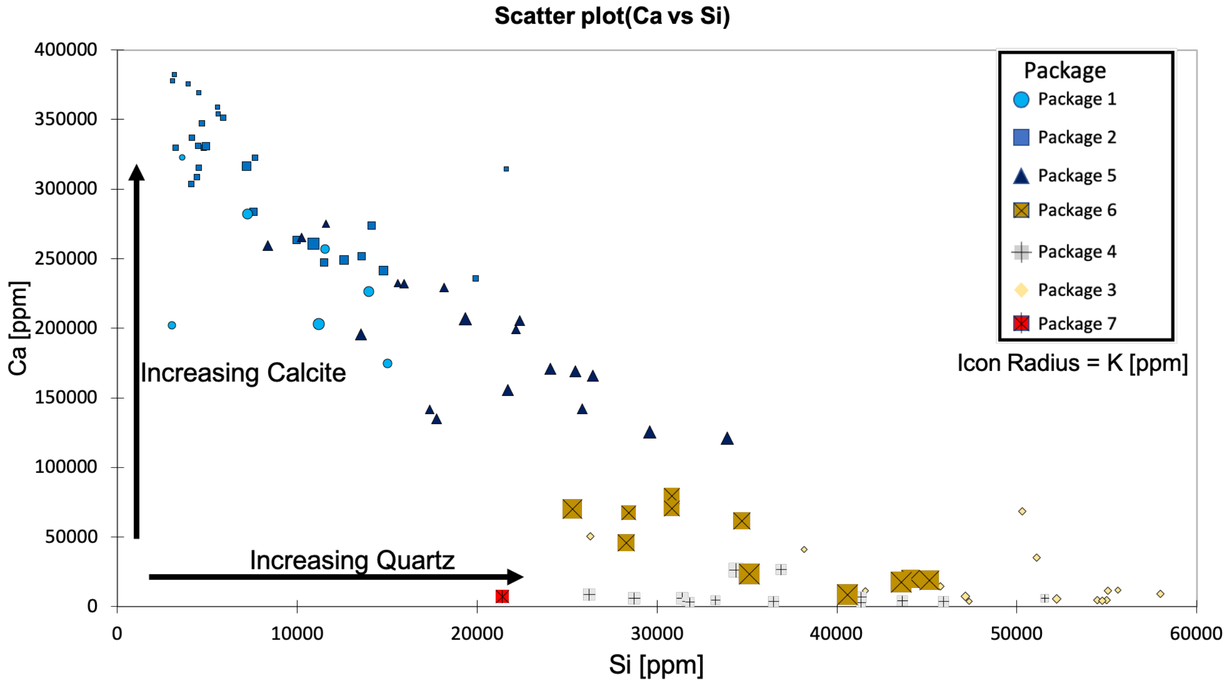

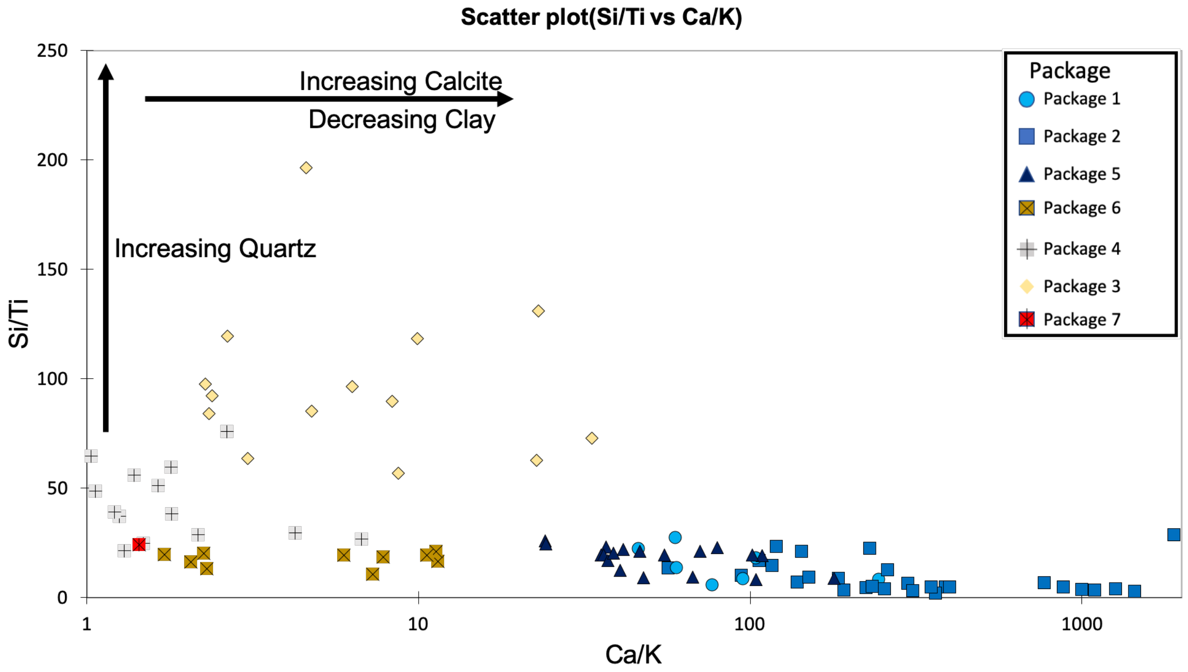

Figure 52. A) Scatter-plot of calcite (vertical axis), silica (horizontal axis), and potassium (icon radius). The legend on the upper right-hand side shows the symbols which represent each package. B) Scatter-plot of silica/titanium (vertical axis) and calcite/potassium (horizontal axis). The legend on the upper right-hand side shows the symbols which represent each package.

The two charts above shown in Figure 52 help us to further visualize and understand the variations in lithology and serve to supplement and confirm observations made from the ternary diagram. The top chart, chart A, shows an excellent negative correlation between Si and Ca. In addition to these two parameters, K has been plotted along the z-axis and is proportional to the size of the icon radius. This shows a nice relationship between decreasing calcite and increasing silica with increasing K, which is representative of the clay fraction. This is true for all packages except for packages three and four, the cherts and heavily silicified units. Although, it is clear that package four contains higher levels of K and lower levels of Si than package three.

Chart B relays similar information to that displayed in chart A, however, the terrigenous representative, Ti, is included, by plotting the Si/Ti ratio versus the Ca/K ratio. Therefore, as calcite increases to the right, K (or clay) decreases. As for the y-axis, moving upwards means a higher Si/Ti ratio, and therefore the more biogenic its origin. The converse is also true, and moving downward means lower Si/Ti ratio, and therefore more terrigenous in origin. This plot displays the transition of package 2 as the most calcite and least clay-rich to packages one and eventually five moving to the left. To the farthest left is the most clay-rich and the most terrigenous influenced package six. The cherts of package four can be seen just above this, while the most biogenic cherts of package three lies above all.

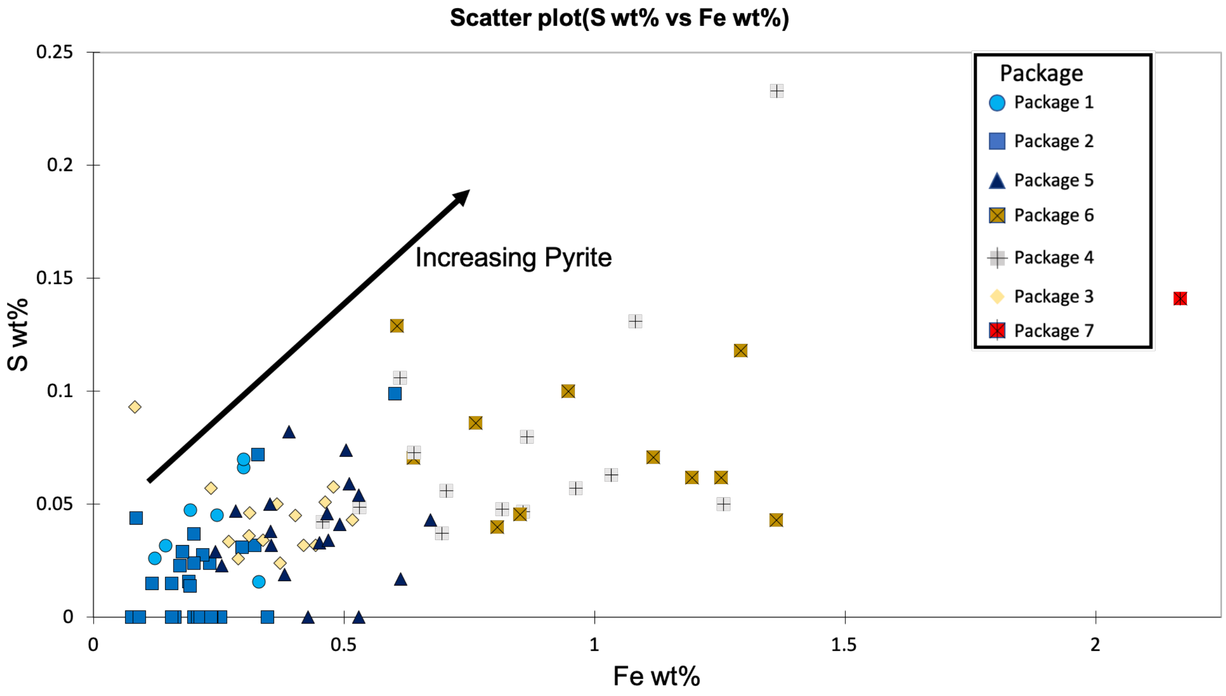

Figure 53. Scatter-plot of sulfur weight percentage (vertical axis) and iron weight percentage (horizontal axis). The legend on the upper right-hand side shows the symbols which represent each package.

This graph (Figure 53) helps to visualize the degree of pyritization within each chemostratigraphic package by plotting the sulfur weight percentage and the Fe weight percentage. Goldberg and Humayn (2016) were able to show that in general, the number of pyrite increases as both S and Fe increase, as long as it is at or below the pyrite/gypsum line, which is at y = 1.15x. Above this line, the mineralogy is representative of gypsum rather than pyrite. This line is not plotted since the data lie well beneath this marker and are all interpreted to represent pyritization, so the line shown simply represents the direction of increasing pyrite (Goldberg and Humayn, 2016).

As the graph shows, the lowest levels of pyritization are seen in packages one and two. This is followed by packages three and five, then four and six, and lastly package seven. This suggests that the calcareous siltstone and the various, heavily silicified units represented by package four were deposited in an environment that most favors the precipitation of pyrite compared to the others. It is worth noting that pyrite was found in most samples, however, it is difficult to quantify without thin section point counting, which can be extremely tedious and difficult owing to the optic qualities of pyrite.

Chapter 6: Interpretations

6.1 Sequence Stratigraphy

Sequence stratigraphy refers to the analyses of genetically related strata bound by unconformities and their correlative conformities within a time-stratigraphic framework (Van Wagoner, 1995). In order to understand the stratigraphy within Shumard Canyon, it is useful to understand depositional system tracts and resulting depositional facies, along with their sequence boundaries and bed-set termination style.

Sequence Stratigraphy of the Bone Spring Formation can provide vital information for a detailed understanding of the formation as a petroleum system. This is in part owing to reciprocal sedimentation and the strong tie between lithology and system tract, for example, increased carbonate content represents higher sea levels, while increased siliciclastic input represents lower sea level conditions (Silver and Todd, 1969; Mullins and Cook, 1986; Nance and Rowe, 2015). Ultimately, it is useful to reconstruct the basin-fill history from the impact of relative sea level change and for stratigraphic prediction.

6.1.1 Sequence Stratigraphic Framework

Several recent studies have investigated the high-frequency cycles within Leonardian and Guadeloupian units in the Guadalupe Mountains (Borer and Harris, 1991a; 1991b; Kerans and Harris, 1993; Borer and Harris, 1995; Tinker, 1998; Osleger and Tinker, 1999; Kerans, 2000; Hurd et al., 2018). The primarily accepted sequence-stratigraphic framework was established by Tinker (1998). Kerans and Fitchen (1995) and later Kerans and Kempter (2002) integrated Tinker’s work and conducted a hierarchical stratigraphic analysis on all present formations for the Guadalupe Mountains. Their schemes subdivided stratigraphic sections into composite sequences (CS), which are essentially third-order sequences. These are further subdivided into high-frequency sequences (HFS), or fourth-order sets, and are composed of system tract cycles and HFS cycle sets. A single HFS cycle represents a fifth-order parasequence and represents a sea level rise and fall.

The upper Bone Spring Formation and time equivalent Victorio Peak and Yeso Formations are found within composite sequence eight (CS-8). In Shumard Canyon, these exposed upper Leonardian units are within HFS Leonardian 5 and Leonardian 6 (L5 and L6), consisting of mostly slope to basinal facies of the lowstand system tract (LST) of CS-8. The L5 HFS corresponds to a sea level transgression while the L6 corresponds to a sea level highstand. This study was conducted within the L5 HFS transgression.

In this investigation, the high-resolution sequence stratigraphic model used for this mixed siliciclastic-carbonate slope systems represented in upper Leonardian outcrops is adapted from Pigott et al. (2012). In this four systems tracts model, the regressive system tract (RST), lowstand system tract (LST), transgressive system tract (TST), and high stand system tract (HST) were defined by the attribution of relative sea level change in a complete cycle.

6.1.2 Chemostratigraphy

Chemostratigraphic analyses shows variations of elements within sedimentary sequences and have been used for stratigraphic correlation, paleoenvironmental analyses, reservoir characterization, and many more various geologic analyses across all fields (Tribovillard et al., 2005). In this study, chemostratigraphy is the main approach used to link stratigraphic units to provenance, paleoredox conditions, and relative sea level. The chemostratigraphic analysis defines seven chemostratigraphic packages in total, and each stratigraphic package is defined in terms of elemental variations in each proxy group along the XRF profile (Figure 54, Figure 55). The characters for each chemostratigraphic package are listed in Table 1 and Table 2.

The detailed elemental variations for different formations are discussed in Chapter 4 and Chapter 5. To link stratigraphic packages and systems tracts deposited during different stages of sea level alteration, the provenance-responded siliciclastic proxies, and carbonate proxies were firstly used to analyze the shoreline trajectory. After applying the hierarchical cluster analysis discussed in Chapter 4, selected siliciclastic proxies (such as Ti, Zr, K) and carbonate proxies (Ca, Sr) are expected to be significantly associated with marine transgression and regression (Turner, 2016).

As the siliciclastic proxies increase and carbonate proxies decrease in concentration, the relative sea level drops and the shoreline moves basinward. During this stage, the pre-existing shelf margin is likely subaerially exposed and detrital sediments can bypass the platform rim. At the same time, the carbonate sediments decrease as a result of the termination of the shelfal carbonate factory. When the siliciclastic proxies decrease and carbonate proxies increase in concentration, it implies the relative sea level is rising and the shoreline moves landward with an increase in carbonate platform productivity. Consequently, carbonate deposits accumulate on the foreslope and fewer siliciclastics are deposited.

Redox proxies were employed to analyze the bottom water circulation within the different systems tracts. The relatively high values are linked to suboxic to anoxic environments, and moderate to low values are linked to oxic to suboxic environments. The interpreted characteristics of these packages and associated sequence events are listed in Table 3.

System Tracts	Start Time	End Time	Elemental Characters			Packages
			Siliciclastic Proxies	Carbonate Proxies	Redox Proxies	
HST	End of transgression	End of HST stasis	Low	High	Low to Moderate	1, 2, 3, 4, 5
RST	End of HST stasis	End of Base-level fall	Moderate to High	Low to Moderate	Moderate to High	4, 5, 6
LST	End of base-level fall	End of LST stasis	Moderate to High	Low	High	4, 6
TST	End of LST stasis	End of transgression	Moderate	Moderate to High	Moderate to High	1, 2, 3, 4, 5

Table 3: The start and end times of systems tracts and associated proxy variations in this study (modified from Xu, 2018).

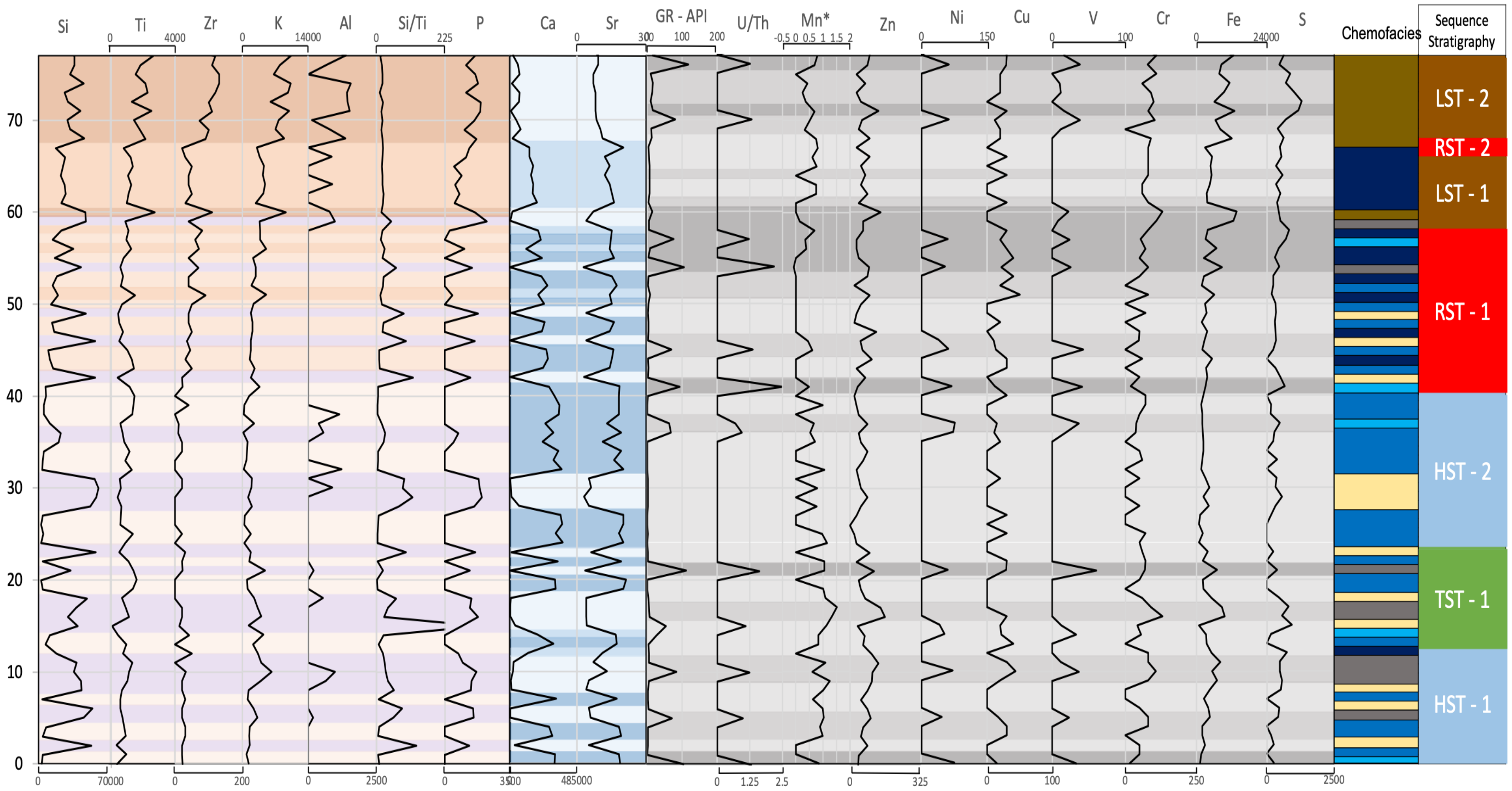

Figure 54. This figure shows elemental proxies for clastic and carbonate deposition as well as paleo-redox indicators for measured sections 1A to 1D of the North Wall as shown in Figure 7, plotted against the chemo-package and sequence stratigraphic interpretations. The higher the proxy magnitudes the darker the window. Note biogenic silica is delineated by purple.

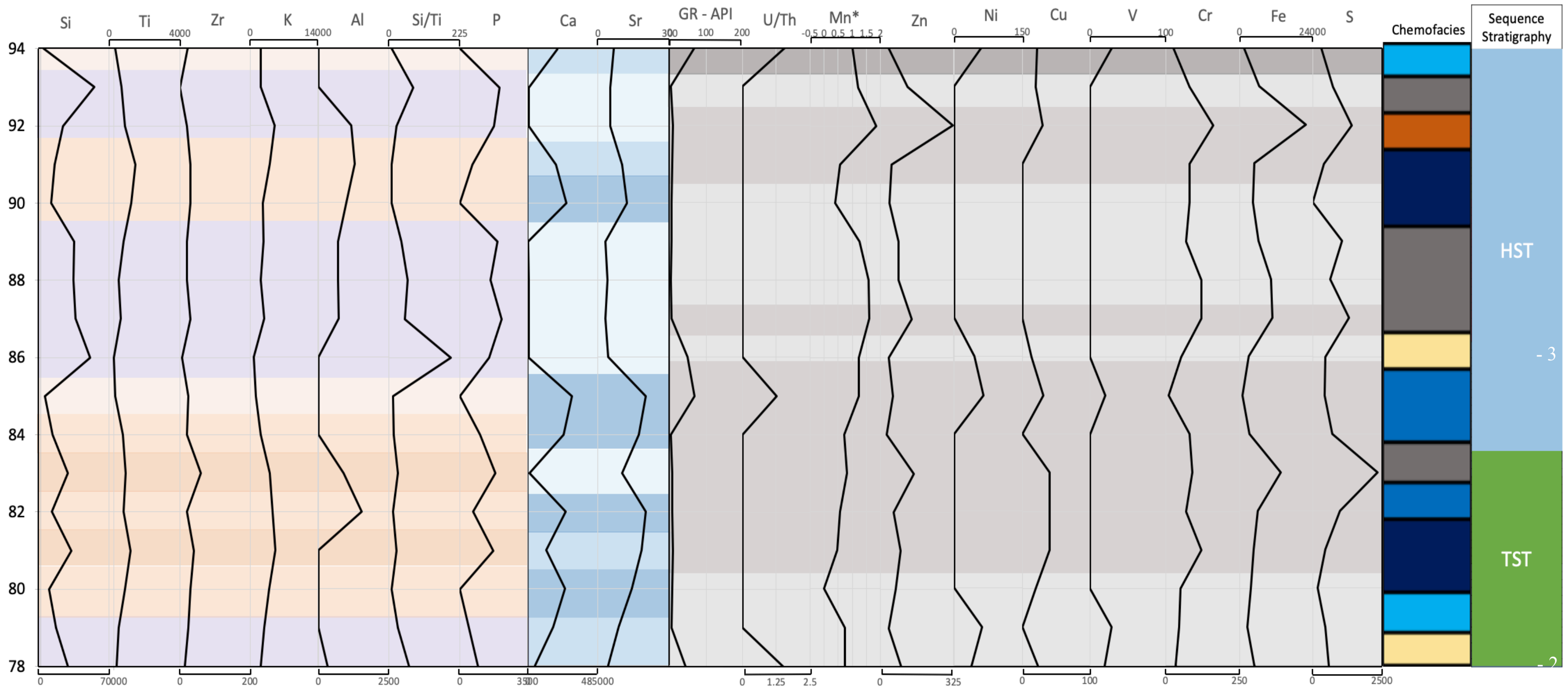

Figure 55. This figure shows elemental proxies for clastic and carbonate deposition as well as paleo-redox indicators for measured sections 2A to 2B, plotted against the chemo-package and sequence stratigraphic interpretations. The higher the proxy magnitudes the darker the window. Note biogenic silica is delineated by purple.

This study further subdivides the L5 HFS into system tracts based on outcrop observation and XRF derived elemental proxy response, shown in Figure 54 and Figure 55. These subdivisions are named by the interpreted system tract and numbered from the base. However, it is worth noting that since the base of the formations is deep into the subsurface, the numbering is only chronologically representative of what is exposed in the canyon. There are nine total sequence systems identified, with seven in section one and two in section two.

6.2 Depositional setting

In this mixed siliciclastic-carbonate slope system, variations in relative sea level are significant factors affecting depositional settings in terms of sediment supply and depositional locations. Based on the sediment provenance analysis discussed in Chapter 5 associated with sea level interpretations discussed in the previous section the different depositional settings of a complete sequence within different systems tracts are summarized below.

TST: The rate of relative sea level rise is greater than the sedimentation rate and transgression occurs. Carbonate reefs grow in an attempt to keep up with sea level, while the shelf carbonate mud factory remains inactive. Siliciclastic input is constrained by the reef barriers on the shelf margin. Coarse-grained, matrix-poor sediments caused by slope failures form the thick and steeply dipping beds at the foreslope and pinch out with downlapping terminations on gently dipping toe-of-slope sections (Figure 56).

HST: Relative sea level is at its highest and about to drop, and the shelves are flooded. The siliciclastic sediments during this stage are negligible. Fine-grained, mud- dominated carbonates exhibit aggradation and progradation on foreslope and toe-of-slope sections. The deposits develop onlapping terminations against the preexisted beds. The shoreline begins to move basinward during this stage, and the reef boundstone debris is deposited at the forslope, forming downlap termination (Figure 57).

RST: Relative sea level drops and the shelf margin is subaerially exposed. Forced regression occurs within this system tract. Siliciclastics are transported across the shelf and bypass or incise foreslope valleys and are accumulated at foreslope, toe-of-slope, and basinal environments. With the rapid relative sea level fall, reef growth ceases and the carbonate mud factory on the shelf is shut down. Coarse-grained, matrix poor mixed siliciclastic-carbonate sediments are deposited along the slope (Figure 58).

LST: Sedimentation rates are greater than rates of relative sea level rise. Normal regression occurs within this system tract. The aggradation of mostly siliciclastics with small amounts of coarse carbonates from the toe-of-slope sections to the basin is the most common strata stacking pattern (Figure 59). The fine-grained siliciclastics are transported from the shelf or winds.

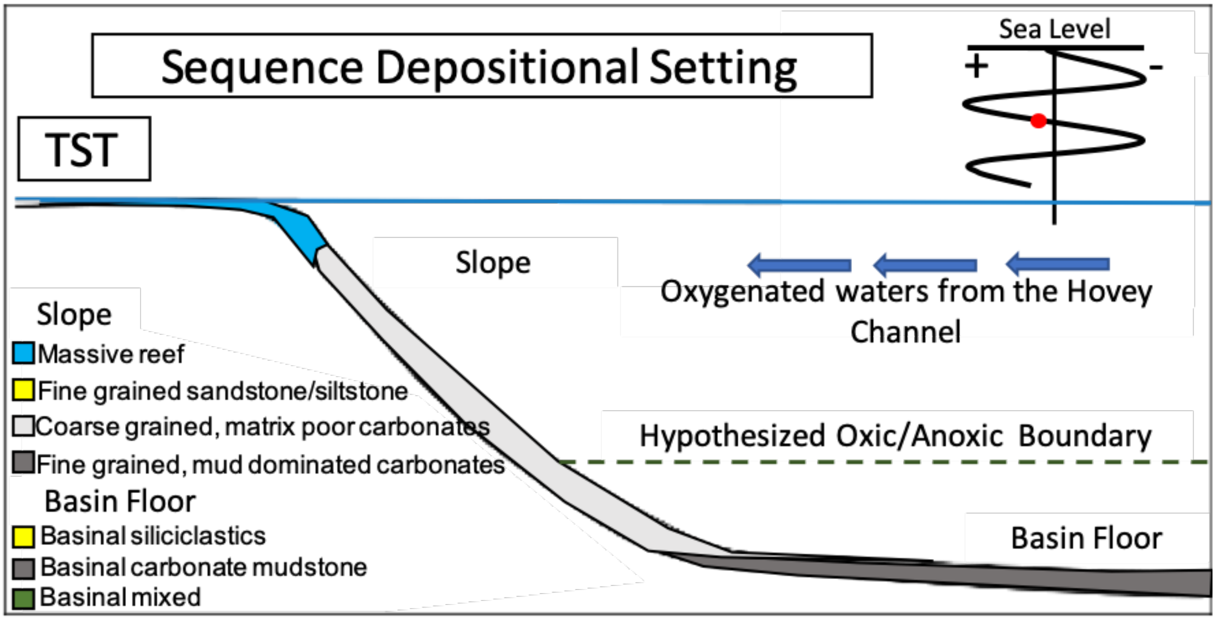

Figure 56: Slope developments during TST stage. Note that if reef growth keeps up with sea level rise, channels can potentially become or remain restricted, not allowing for water oxygen renewal (figure modified from Xu, 2018).

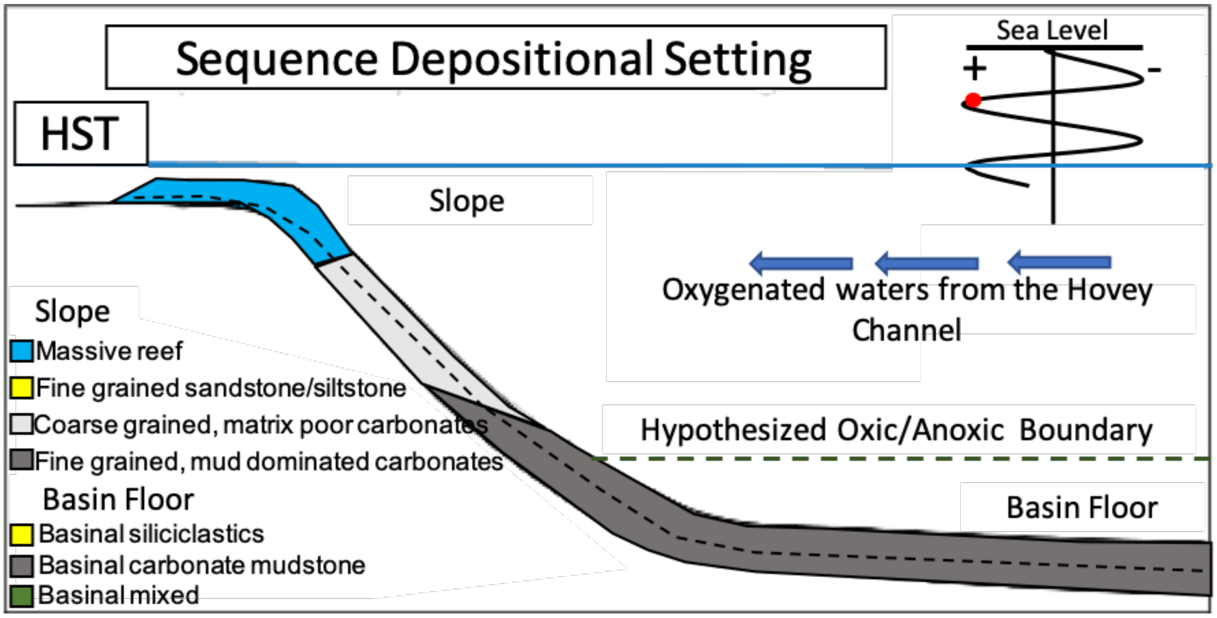

Figure 57: Slope developments during HST stage. Again, it is important to note that when reef growth catches up with sea level, channels can potentially become restricted, not allowing for water oxygen renewal (figure modified from Xu, 2018).

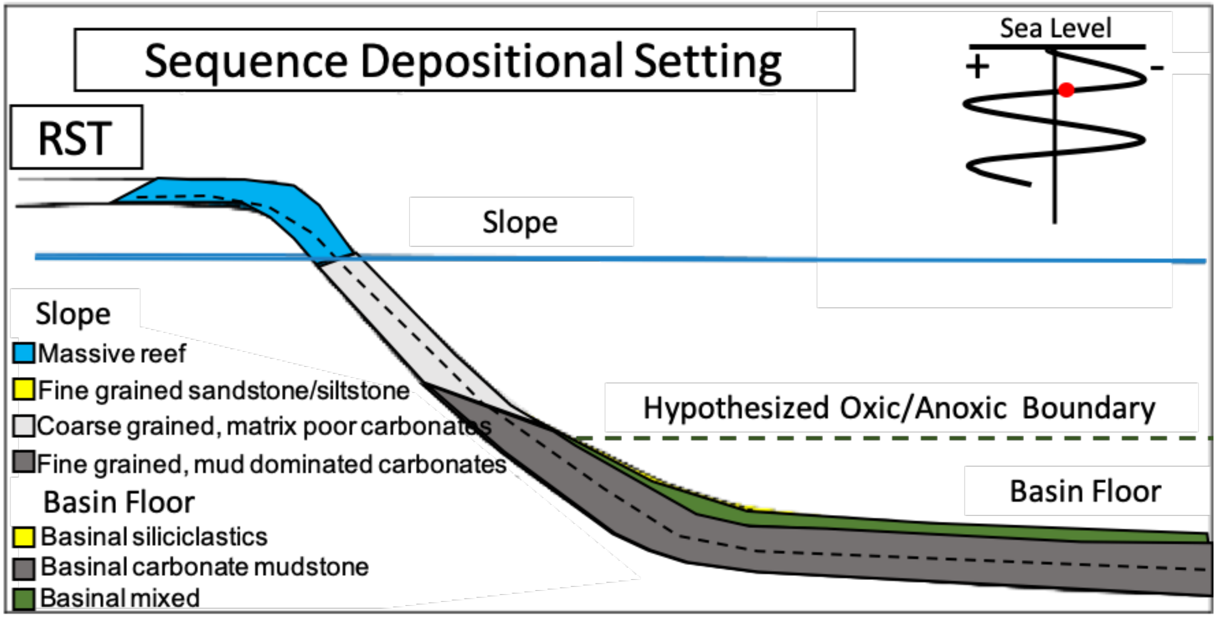

Figure 58: Slope developments during RST stage. Sea level drops and water restriction begins, raising the oxic/anoxic boundary (figure modified from Xu, 2018).

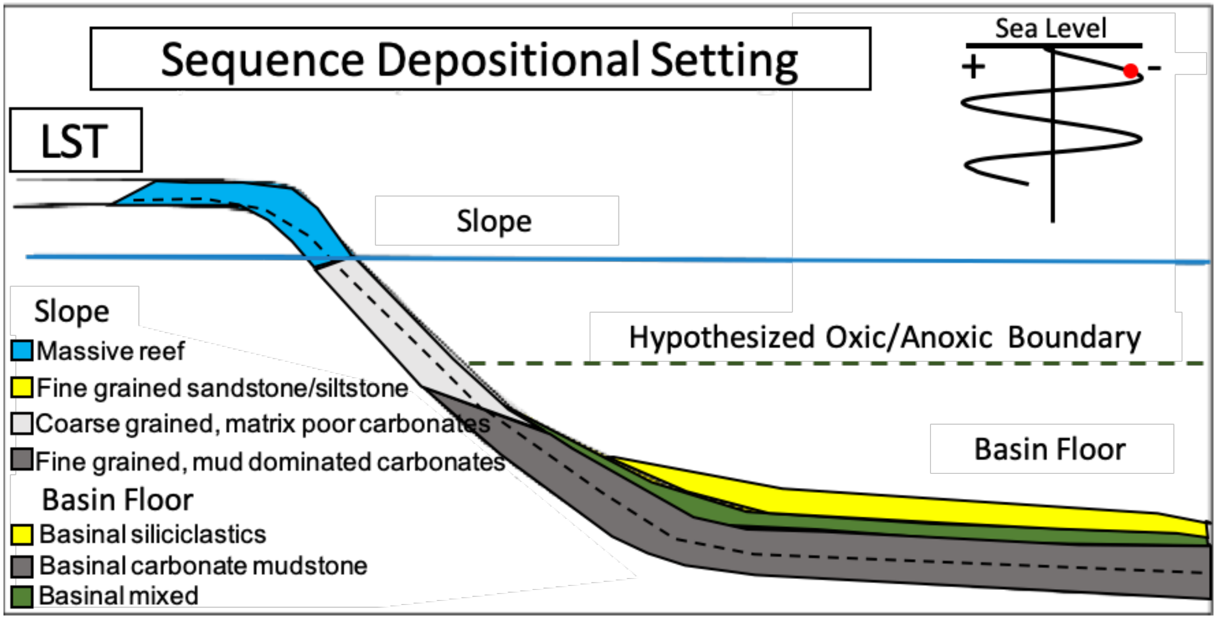

Figure 59: Slope developments during LST stage. Sea level is low and stagnant due to lack of connection with Panthalassa Ocean from the Hovey Channel, raising the oxic/anoxic boundary. Shallow waters may remain oxygenated (figure modified from Xu, 2018).

6.4 Geomechanical Interpretations

Mechano-facies	Stats	Q Mean Value	R	E (Gpa)	UCS (Mpa)	ρ (kg m^-3)	Vp (m/s)	B.I.
BLUE	MIN	22.45	13.10	0.36	5.31	490.59	3488.10	0.00
4	MAX	31.15	21.95	1.79	9.61	1166.37	3967.33	0.93
	AVG	26.83	17.55	1.05	7.43	836.58	3729.09	0.30
LIGHT BLUE	MIN	38.65	29.59	4.50	16.03	1556.81	4380.47	0.08
3	MAX	57.25	48.53	20.76	57.02	2203.88	5405.04	0.97
	AVG	50.09	41.24	13.34	37.51	1976.68	5010.61	0.42
GREEN	MIN	58.2	49.50	22.06	60.84	2229.69	5457.37	0.06
1	MAX	66.95	58.41	36.80	110.52	2446.18	5939.36	0.93
	AVG	63.0	54.39	29.77	85.90	2351.21	5721.95	0.42
ORANGE	MIN	68.5	59.98	39.96	122.85	2481.06	6024.75	0.00
2	MAX	72.7	64.26	49.44	163.61	2571.14	6256.10	0.99
	AVG	70.47	61.99	44.30	141.05	2523.85	6133.37	0.39
RED	MIN	73.45	65.02	51.27	172.19	2586.59	6297.41	0.00
5	MAX	81.7	73.42	74.64	302.31	2745.50	6751.86	0.97
	AVG	76.73	68.36	60.15	218.97	2651.00	6477.82	0.44

Table 4. This table shows basic statistics compared to its mechanical package for Q and R, and has been ordered by weakest to strongest. The variables are the empirically derived values for R, Youngs Modulus (E), uniaxial compressive strength (UCS), density (ρ) (Katz et al, 2000), and p-wave velocity (Vp) (Altindang et al, 2005). The packages are ordered by strength and assigned a heat map color based on intensity.

As stated in Chapter 3, the SilverSchmidt rebound hammer was used to acquire geomechanical data after each XRF measurement. The Q value obtained from these measurements is a function of the overall strength of the rock, which is affected by various factors such as lithology, fracture density and orientations, and bed thickness. Empirical equations were then used in order to convert Q to R value, and then R to Young's Modulus (E), Uniaxial compressive strength (UCS), Density (ρ), and finally p-wave velocity (Vp), as mentioned in Chapter 3.

The same AHC program that was run to generate chemofacies clusters has been used with this data in order to help visualize the data acquired by the SilverSchmidt rebound hammer. Since all of the variables above were derived from the original Q values using empirical formulas, the clusters were essentially organized by similar amplitudes, as the chart shows. This allowed for each data point to be put into its cluster group to generate the heat map, displayed below in Figure 60.

In order to visualize the potential relationship between composition and mechanical properties, a simple mineralogical based brittleness index proposed by Jarvie et al. (2007) was calculated based upon the mineral weight percent abundance of quartz divided by the weight percent of the sum of quartz, calcite, and clay. This index works since quartz is generally one of the more abundant stiff (high Young's Modulus) minerals, and is being compared to the bulk matrix volume. It is also worth noting that this makes it a decent lithologic indicator.

The mechanical property heat map is displayed below alongside the Jarvie brittleness index, lithology, chemofacies, and Ni (ppm), Cu (ppm), and Zn (ppm). Ni, Cu, and Zn are included since they are proxies for high organic content environments as previously discussed, which will theoretically deform under elastic deformation. Altogether, this suite of logs can serve as a platform to identify potential sweet spots for oil and gas production by looking for more brittle zones with potentially high organic content.

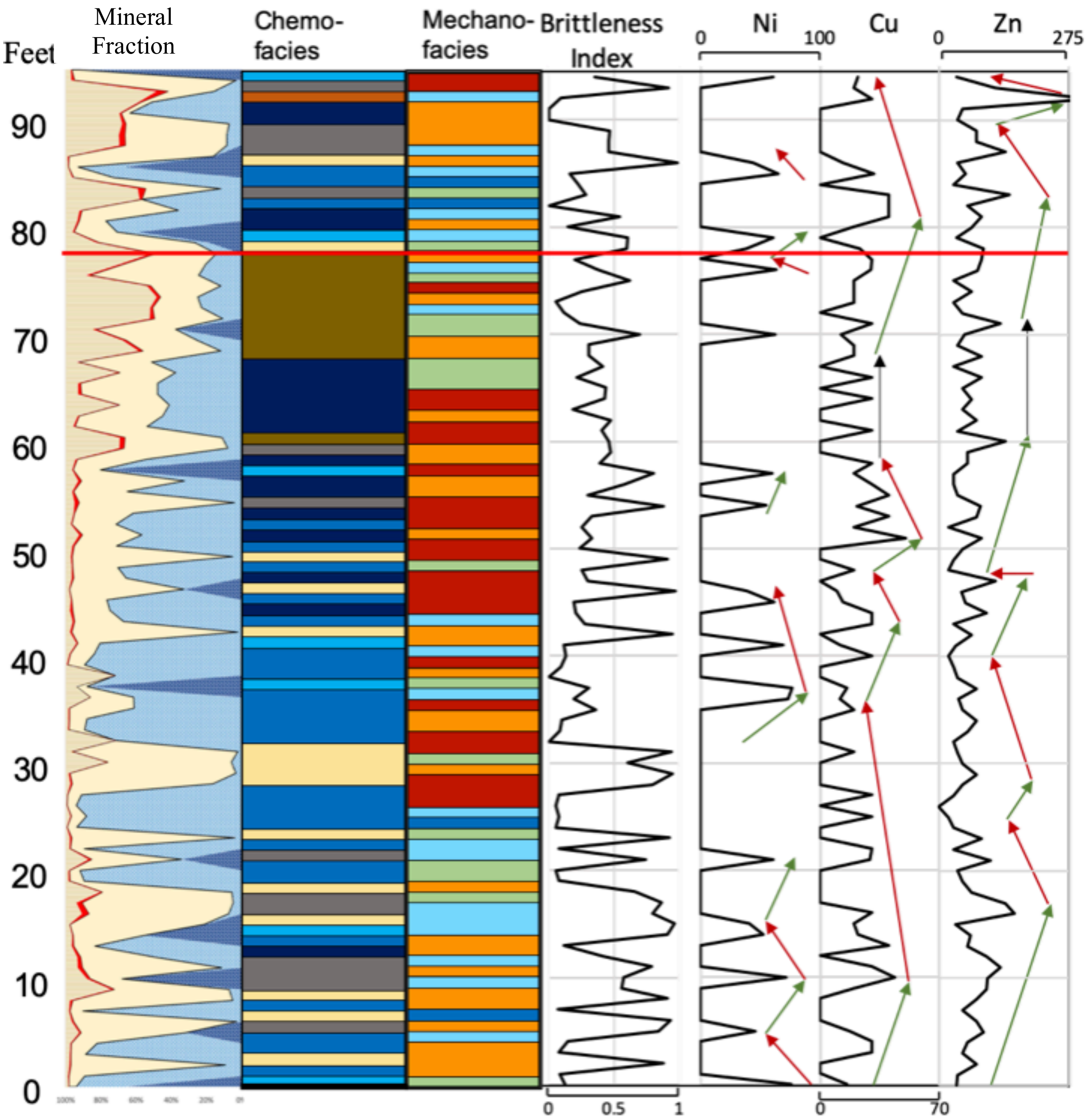

Figure 60. Lithology, elemental packages, mechanic packages, brittleness index, Ni (ppm), Cu (ppm), and Zn (ppm) plotted against one another. Green and red arrows in nickel and copper show relative increases and decreases, respectively. The red line marks the end of section one and the beginning of section two.

Sweet spot optimization is an important step in planning unconventional wells. Optimization is done by identifying where anoxic preservation of organic matter and maximum brittleness overlap. This method can be done using the data presented in Figure 60. From about zero to 40 feet, there is an extremely high amount of chert layered within the high carbonate percentage units deposited during highstand seas. Although there may be in-situ organic matter present, and the cherts are very brittle, this will not make for a good unconventional target. Since redox proxies were low, organic matter accumulation must occur by the organic matter rain rates being higher than decomposition rates, while at the same time organic matter preservation must occur by rapid burial to reach anoxia in the sediment column. The cherts are mostly impermeable (high ratio of healed fractures to open fractures), and the crystalline carbonate matrix has closed off most microporosity.

From 40-60 feet, there is a rise in background silica. As show by the thin section analysis, this rise in silica has been attributed to a steady increase in silt. This has resulted in an increase in brittleness by the brittleness index and also with an increase in hardness in the mechanical heat map. However, it is worth noting that this section has thicker deposits in general, also resulting in higher Schmidt Hammer response. This section has been interpreted as a series of RST deposits as Si, Zr, and Ti are constantly increasing, and are paired with medium levels of redox proxies which rise to high levels near the end of the section. It is worth noting that there is no associated increase in clays along with the increase in silica, however, chert beds are still present. The thin section analysis also shows that there is still a crystalline carbonate matrix present in the rocks, however there is also a notable increase in micro-porosity and organic matter. This increase in microporosity is paired with spikes and large jumps in Ni, Cu, and Zn, further supporting the idea that there was an increase in organic matter rain at the time of deposition. Altogether, this section makes for a good sweet spot for unconventional targets.

From 60-78 feet there are two main sharp increases in silica followed by stasis. There is also a large increase in clay content, which is also followed by stasis. This has been interpreted to be two LSTs with a small RST in between. The brittleness index shows a slight decline here owing to the presence of clay minerals, in addition to the presence of thin beds. The heat map reflects this increase in ductility; however, it is still somewhat brittle. There is lower but steady Ni, Cu, and Zn, which is paired with medium levels of redox proxies, indicating that organic matter is present and has some potential for preservation. The thin section analysis confirms the presence of organic matter and also reveals increased micro-porosity along with a decrease in total volume of crystalline carbonate matrix. In addition, only about half of the siltstone was included in the detailed section as the other half was too high and inaccessible. Therefore, instead of about ten feet, there are about twenty feet of this unit present in the outcrop, which would be located just before the red line in the Figure indicating the jump to section two. Altogether, this section (thirty feet in actuality) makes for a good sweet spot for unconventional targets.

Section two, or from about 78-94 feet, marks the final measured section in this study. The first six feet – section 1A, consisted of parallel beds and topped with a large erosive surface, and show increasing calcite throughout. This sectuib has been interpreted to be a TST and is followed by the large, highly deformed, coarse-grained carbonate slump with steady calcite levels in section 2B, which is interpreted as an HST. There is also a lot of chert in both sections. The XRF analysis reveals that there are low to medium levels of redox proxies, and medium levels of organic matter proxies. The thin section analyses confirm that there is little organic matter still present and that there is little to no micro-porosity. Altogether, this section does not present a sweet spot for unconventional drilling.

Chapter 7: Conclusions

7.1 Conclusions

The Bone Spring Formation was a mixed carbonate and siliciclastic slope to basin deposit. Its depositional history is marked by shelf instability. From the study of four outcrop locations using classical field methods, thin section analysis, XRF, and Schmidt Hammer the following conclusions are drawn:

- Spicules, Radiolarians, Forams, Bryozoans, Corals, Trilobites, Echinoderms, Brachiopods, Bivalves, Fusilinids, and Gastropods show deep to increasingly shallow allochem supply. Lack of ooids, pisolites, and fenestrae fabrics indicate that the restricted marine back reef environment was not affected by slope failure. Radiolarians and Sponge Spicules are the dominant suppliers of silica for silicification and chert formation. This biologic assemblage is representative of the updip Victorio Peak shelf margin carbonate reef.
- Differences in lithological composition and lack of correlation observed in geochemical proxy profiles indicate deposition of sediment in different facies.
- Grain flows and high-density turbidite flows are the dominant mechanisms responsible for transporting skeletal and non-skeletal sediment deposits observed in the slope and basinal Bone Spring. The large disfigured member of section 2B is a massive slump feature consisting of course-grained carbonate material derived from with Victorio Peak reef, indicating basinward migration of the shoreline.
- Hummocky cross-bedding observed in the canyon is interpreted to be high energy deposits, either deep water calciturbidites or possibly tsunamites. Similar slope failures,

such as the one which generated the large slump feature, are most likely the cause of the driving forces responsible for the deposition of such beds downslope and in the basin.

- A high-resolution sequence stratigraphic framework along two measured sections on the slope in Shumard Canyon of the Guadalupe Mountains is established. Nine high frequency system tracts within the L5 HFS are identified based on outcrop observations and XRF data.
- Seven chemostratigraphic packages are defined based on the variations of elemental proxies determined from hierarchical cluster analysis. The changes of elemental proxies are interpreted to be significantly influenced by the sea level changes.
- Redox conditions are attributed to restricted water renewal via the Hovey Channel from the Panthalassa Ocean caused by relative sea level fall. The oxic and suboxic conditions were attributed to increased water renewal from the Panthalassa Ocean as sea level increased.
- A sequence depositional model is established to reflect sedimentation changes from sea level fluctuations. During relatively low sea level, fine-grained siliciclastic deposition increased. During relatively high sea level, mostly mud-dominated carbonates and fewer siliciclastics were deposited. Mixing of siliciclastics and carbonates occurred at all phases, but was highest in transitional phases of sea level.
- The TST and HST deposits identified in this study (Figures 54 and 55) show lower overall hardness values than the LST and RST deposits. This decrease in hardness is due to the high levels of carbonate material and lower amount of silica being transported into the basin, and results in a more ductile lithology. There are, however, higher amounts of

chert present in the TST and HST deposits, which show very high hardness values and are very brittle due to the high silica content.

- The LST deposits identified in this study show mid-range hardness values. This mechanical response is owing to the increased levels of silica and decreased levels of carbonate paired with increased clay content. However, the RST deposits (Figure 54) show the highest overall bulk hardness values as shown in the heat map in Figure 60. This mechanical response is attributed to the increased deposition of siliciclastic silts without an increase in clay or carbonate material, resulting in more brittle lithology. The higher brittleness is paired with spikes Ni, Cu, and Zn, supporting the idea that there was an increase in organic matter rain at the time of deposition. These properties, in addition to other petrographic properties such as increased micro-porosity, make these RST deposits good sweet spots for unconventional targets.

References

Adams, J.E., M.G. Cheney, R.K. DeFord, R.I. Dickey, C.O. Dunbar, J.M. Hills, R.E. King, E.R. Lloy, A. K. Miller, and C. E. Needham, 1939, Standard Permian Section of North America: AAPG Bulletin, v. 23, p. 1673-1681.

Adams, J.E., 1965, Stratigraphic-Tectonic Development of Delaware Basin: Bulletin of the American Association of Petroleum Geologists, v. 49.11, p. 2140-2148.

Adams, J.E., 1944, Upper Permian Ochoa Series of Delaware Basin, West Texas and Southeastern New Mexico: Bulletin of the American Association of Petroleum Geologists, v. 28.11, p. 1596-1625.

Algeo, T.J., and H. Rowe, 2012, Paleoceanographic Applications of Trace-metal Concentration Data: Chemical Geology, v. 324-325, p. 6-18.

Algeo, T.J. and N. Tribovillard, 2009, Environmental Analysis of Paleoceanographic Systems Based on Molybdenum–uranium Co-variation: Chemical Geology, v. 268.3-4, p. 211-225.

Algeo, T.J., and J.B. Maynard, 2008, Trace-metal Co-variation as a Guide to Water-mass Conditions in Ancient Anoxic Marine Environments: Geosphere, v. 4.5, p. 872-887.

Algeo, T.J., T.W. Lyons, R.C. Blakey, and D.J. Over, 2007, Hydrographic Conditions of the Devono–Carboniferous North American Seaway Inferred from Sedimentary Mo–TOC Relationships: Palaeogeography, Palaeoclimatology, Palaeoecology, v. 256.3-4, p. 204-230.

Altindag, R., Yavus, H., Sarac, S., 2005, Evaluation of the Relationship between Schmidt Hammer Rebound Number and Other (Engineering) Properties of Rocks: International Mining Congress and Fair of Turkey, v. 19, p. 83 – 89.

Bachmann, Joseph, Philip Stuart, Brian Corales, Blake Fernandez, Peter Kissel, Holly Stewart, David Amoss, Blaise Angelico, Alonso Guerra-Garcia, K. Blake Hancock, Richard Roberts, and Bill Sanchez, 2014, The "New" Horizontal Permian Basin. <http://www.howardweil.com/docs/Reports/OtherReports/PermianBasin01-27-14.pdf>.

Barker, C.E. and R.B. Halley, 1986, Fluid Inclusion, Stable Isotope, and Vitrinite Reflectance; Evidence for the Thermal History of the Bone Spring Limestone, Southern Guadalupe Mountains, Texas: SEPM Special Publications, v. 38, p. 189-203.

Barron, E. J., and P. J. Fawcett. 1995, The Climate of Pangea: A Review of Climate Model Simulations of the Permian in P.A. Scholle, T.M. Peryt, and D.S. Ulmer-Scholle, eds., The Permian of Northern Pangea, Berlin: Springer-Verlag, v. 1, p. 37-52.

Bassiouni, Zaki, 1994, Theory, Measurement, and Interpretation of Well Logs: Society of Petroleum Engineers, Richardson, TX, 93-328.

Bassett, D. A., 2012, Evaluation of Chemostratigraphy in Interpreting Stratigraphic Architecture of the Bone Spring Formation in the Delaware Basin, Eddy County, New Mexico: Master's thesis. Oklahoma State University, 2012, Stillwater, Oklahoma, 260 p.

Beaubouef, R.T., 1999, Deep-water Sandstones, Brushy Canyon Formation, West Texas: Field Guide for AAPG Hedberg field research conference.

Blakey, R., 2013, Global Paleogeography, Northern Arizona University. <http://www2.nau.edu/rcb7/nam.html>.

Brown, A., and Davies, R., 2016, Using X-Ray Flourescence to Quantify Clay Content in Mudrock and Sandstone Outcrops: AAPG Annual Convention and Exhibition 2013, Search and Discovery Article #41773

Brumsack, H.J., 2006, The trace metal content of recent organic carbon-rich sediments: Implications for Cretaceous black shale formation: Paleogeography, Paleoclimatology, Paleoecology, v. 232, p. 344-361.

Budzik, P., 2014, Energy Information Administration (EIA): Six Formations Are Responsible for Surge in Permian Basin Crude Oil Production. <www.eia.gov> Accessed April 2014.

Catuneanu, O., W.E. Galloway, C.G.St.C Kendall, A.D. Miall, H.W. Posamentier, A. Strasser, and M.E. Tucker, 2011, Sequence Stratigraphy: Methodology and Nomenclature: Newletters on Stratigraphy, v. 44/3, p. 173-245.

Catuneanu, O., V. Abreu, J.P. Bhattacharya, M.D. Blum, R.W. Dalrymple, P.G. Eriksson, C.R. Fielding, W.L. Fisher, W.E. Galloway, M.R. Gibling, K.A. Giles, J.M. Holbrook, R. Jordan, C.G.St.C. Kendall, B. Macurda, O.J. Martinsen, A.D. Miall, J.E. Neal, D. Nummedal, L. Pomar, H.W. Posamentier, B.R. Pratt, J.F. Sarg, K.W. Shanley, R.J. Steel, A. Strasser, M.E. Tucker, and C. Winker, 2009, Towards the Standardization of Sequence Stratigraphy: Earth-Science Reviews, v. 92.1-2, p. 1-33.

Crosby, C.B., 2015, Depositional History and High Resolution Sequence Stratigraphy of the Leonardian Bone Spring Formation, Northern Delaware Basin, Eddy and Lea Counties, New Mexico: Master's thesis, University of Oklahoma, p. 1-230.

Dolan, J.F., 1989, Eustatic and Tectonic Controls on Deposition of Hybrid Siliciclastic/Carbonate Basinal Cycles: Discussion with Examples: AAPG Bulletin, v. 73.10, p. 1233-1246.

Dutton, S.P., E.K. Kim, R.F. Broadhead, W.D. Raatz, C.L. Breton, S.C. Ruppel, and C. Kerans, 2005, Play Analysis and Leading-edge Oil-reservoir Development Methods in the

Permian Basin: Increased Recovery through Advanced Technologies: AAPG Bulletin, v. 89.5, p. 553-576.

EIA, 2014, U.S. Crude Oil and Natural Gas Proved Reserves, 2013: <http://www.eia.gov/naturalgas/crudeoilreserves/?src=home-b1> Accessed February 12, 2015.

Ekwunife, I., 2017, Assessing Mudrock Characteristics, High-Resolution Chemostratigraphy, and Sequence Stratigraphy of the Woodford Shale in the McAlister Cemetery Quarry, Ardmore Basin, Oklahoma: Master's thesis, University of Oklahoma, 2017, Norman, Oklahoma, 152 p.

Enderlin, M., Alsleben, H., and Breyer, J., 2011, Predicting Fracability in Shale Reservoirs: AAPG Search and Discovery Article #40783

Fitchen, W.M., Starcher, M.A., Buffler, R. T., and Wilde, G. L., 1995, Sequence stratigraphic framework and facies models of the early Permian platform margins, Sierra Diablo, West Texas, in Garber, R. A. and R.F. Lindsay, eds., Wolfcampian-Leonardian shelf margin facies of the Sierra Diablo—seismic scale models for subsurface exploration: West Texas Geological Society Publication No. 95-9, p. 23-66.

Galloway, W.E.. 1989, Genetic Stratigraphic Sequences in Basin Analysis I: Architecture and Genesis of Flooding-Surface Bounded Depositional Units: AAPG Bulletin, v. 73.2, p. 125-142.

Glenister, B. F., Boyd, D. W., Fumish, W. M., Grant, R. E., Harris, M. T., Kozur, H., Lambert, L. L., Nassichuk, W. W., Newell, N. D., Pray, L. C., Spinosa, C., Wardlaw, B. R., Wilde, G. and Yancey, T. E., 1992, The Guadalupian: Proposed international standard for a Middle Permian Series: International Geology Review, v. 34, p. 857-888.

Goldberg, K., and Humayun, M., 2016, Geochemical Paleoredox Indicators in Organic Rich Shales of the Irati Formation, Permian of the Parana Basin, Southern Brazil: Brazilian Journal of Geology, v46, p. 377-393

Gregory, D.D., Large, R.R., Halpin, J.A., Baturina, E.L., Lyons, T.W., Wu, S., Danyushevsky, L., Sack, P.J., Chappaz, A., Maslennikov, V.V., and Bull, S.W., 2015, Trace element content of sedimentary pyrite in black shales: Economic Geology, v. 110, p. 1389-1410.

Handford, C. R., 1993, Chapter 1: Carbonate Depositional Sequences and Systems Tracts - Responses of Carbonate Platforms to Relative Sea-Level Changes, in R.G. Loucks, eds., Carbonate Sequence Stratigraphy: AAPG Memoir, Tulsa: AAPG, v. 57, p. 3-41.

Haq, B. U., and S. R. Schutter, 2008, A Chronology of Paleozoic Sea-Level Changes: Science, v. 322, p. 64-68.

Hardage, B. A., J. L. Simmons, V. M. Pendleton, B. A. Stubbs, and B. J. Uszynski, 1998, 3-D Seismic Imaging and Interpretation of Brushy Canyon Slope and Basin Thin-bed Teservoirs: Geophysics, v. 63.5, p. 1507.

Harris, N.B., C.A. Mnich, D. Shelby, and D. Korn, 2013, Minor and trace element and Re-Os chemistry of the Upper Devonian Woodford Shale, Permian Basin, west Texas: Insights into metal abundance and basin processes: Chemical Geology, v. 356, p. 76-93.

Hart, B.S., 1997, New Targets in the Bone Spring Formation, Permian Basin: Oil & Gas Journal, p. 85-88.

Hart, B.S., 1998, New Insights on the Stratigraphy and Production Characteristics of the Bone Spring Formation: West Texas Geological Society Publication, v. 98-105, p. 119-126.

Henderson, C. M., V. I. Davydov, B. R. Wardlaw, and O. M. Hammer, 2012, Chapter 24: The Permian Period, in F.M. Gradstein, ed., The Geologic Time Scale 2012: 1st ed. Oxford: Elsevier, 2012. P. 654-677

Herron, S. L., and M. M. Herron, 1996, Quantitative Lithology: An Application for Open and Cased Hole Spectroscopy: SPWLA 37th Annual Logging Symposium, 1996.

Hill, C.A., 1996, Geology of the Delaware Basin, Guadalupe, Apache, and Glass Mountains, New Mexico and West Texas: Society for Sedimentary Geology, Albuquerque, New Mexico, v. 96-39.

Hills, J.M., 1984, Sedimentation, Tectonism, and Hydrocarbon Generation in Delaware Basin, West Texas and Southeastern New Mexico: AAPG Bulletin, v. 68.3, p. 250-267.

Horak, R.L., 1985, Trans-Pecos Tectonism and its Effect on the Permian Basin, in: Dickerson, P.W., and Muehlburger, W.R., (eds.), Structure and Tectonics of Trans-Pecos Texas: West Texas Geological Society Publication 85-81, p. 81-87

Hornbuckle, J.S., 2017, Process Sedimentology of the Guadeloupian Rader Limestone, Delaware Basin: Master's thesis, University of Oklahoma, 2017, Norman, Oklahoma, 187 p.

Huerta-Diaz, M.A., Morse, J.W., 1990. A quantitative method for determination of trace metal concentrations in sedimentary pyrite. Marine Chemistry. 29, 119-144.

Jarvie, D. M., Hill, R. J., Ruble, T. E., and Pollastro, R. M., 2007, Unconventional shale-gas systems: the Mississippian Barnett Shale of North-Central Texas as one model for thermogenic shale-gas assessment: AAPG Bulletin, v. 91, pp. 475 – 499

Katz, O., Reches, Z., Roegiers, J.C., 1999, Evaluation of Mechanical Rock Properties Using a Schmidt Hammer: International Journal of Rock Mechanics and Mining Sciences, v. 37, p. 723-728.

Keller, G.R., J.M. Hills, and R. Djeddi, 1980, A Regional Geological and Geophysical Study of the Delaware Basin, New Mexico and West Texas: New Mexico Geological Society Guidebook, p. 105-111.

Kerans, C., & Kempter, K., 2002, Hierarchical stratigraphic analysis of a carbonate platform. Permian of the Guadalupe Mountains [CD-ROM]: AAPG (American Association of Petroleum Geologists)/Datapages Discovery Series, 5.

Kerans, C., & Tinker, S. W., 1997, Sequence stratigraphy and characterization of carbonate reservoirs (Vol. 40): SEPM.

King, P.B., Geology of the Southern Guadalupe Mountains, Texas: Washington U.S. Govt. Off. 1948.

Kocurek, G. and B.L. Kirkland, 1998, Getting to the Source: Aaeolian Influx to the Permian Delaware Basin Region: Sedimentary Geology, v. 117.3-4, p. 143-149.

Jones, B., and Manning, D., 1994, Comparison of Geochemical Indicators used for the Interpretation of Paleoredox Conditions in Ancient Mudstones: Chemical Geology, p. 111-129

Large, R.R., Bull, S.W., and Maslennikov, V.V., 2011, A carbonaceous sedimentary source-rock model for Carlin-type and orogenic gold deposits: Economic Geology, v. 106, p. 331-358.

Lew C. L., Baharuddin, S. B., and Pigott, J.D., 2013. Deepwater Basin Model for the Permian Basin:Delaware Basin example, The international Petroleum Technology Conference in Bejing, China.

London, S., B. Wall, M. Thompson, N. Turner, Robert Ready, Chip Minty, and Kyle Rose, 2014, The Imperishable Permian Basin, Independent Petroleum Association of America. <http://oilindependents.org/the-imperishable-permian-basin/>.

Luning, S. and S. Kolonic, 2003, Uranium Spectral Gamma-Ray Response As A Proxy For Organic Richness In Black Shales: Applicability And Limitations: Journal of Petroleum Geology, v. 26.2, p. 153-174.

Lyons, T.W., Werne, J.P., Hollander, D.J., Murray, R.W., 2003, Contrasting sulfur geochemistry and Fe/Al and Mo/Al ratios across the last oxic-to-anoxic transition in the Cariaco Basin,Venezuela: Chemical Geololgy, 195, 131–157.

Mack, G.H., and P.A. Dinterman, 2002, Depositional Environments and Paleogeography of the Lower Permian (Leonardian) Yeso and Correlative Formations in New Mexico: The Mountain Geologist, v. 39.4, p. 75-88.

Madhavaraju, J. and Y.I. Lee, 2009, Geochemistry of the Dalmiapuram Formation of the Uttatur Group (Early Cretaceous), Cauvery basin, southeastern India: Implications on provenance and paleo-redox conditions: Revista Mexicana de Ciencias Geologicas, v. 26.2, p. 380-394.

Mazzullo, S.J. and A.M. Reid, 1989, Evolution of San Simon Channel, Gaines County, Texas, Northern Midland Basin: AAPG Search and Discovery, #91026.

Mazzullo, S.J., 1995, Permian Stratigraphy and Facies, Permian Basin (Texas-New Mexico) and Adjoining Areas in the Midcontinent United States in P.A. Scholle, T.M. Peryt, and D.S. Ulmer-Scholle, eds., The Permian of Northern Pangea, Berlin: Springer-Verlag, v. 2, p. 41 58.

McDaniel, P.N. and Pray, L.C., 1967, Bank to Basin Transition in the Permian (Leonardian) Carbonates, Guadalupe Mountains, Texas: American Association of Petroleum Geologists Bulletin, v. 51, 474

McLennan, S.M., 2001, Relationship between the Trace Element Composition of Sedimentary Rocks and Upper Continental Crust: Geochemistry Geophysics Geosystems: An Electronic Journal of the Earth Sciences, v. 2, p. 1-24.

Mullins, H.T., and H.E. Cook, 1986, Carbonate Apron Models: Alternatives to the Submarine Fan Model for Paleoenvironmental Analysis and Hydrocarbon Exploration: Sedimentary Geology, v. 48.1-2, p. 37-79.

McManus, J., W.M. Berelson, G.P. Klinkhammer, D.E. Hammond, and C. Holm, 2004, Authigenic uranium: relationship to oxygen penetration depth and organic carbon rain: Geochimica et Cosmochimica Acta, v. 69.1, p. 95-108.

Mccullough, B.J., 2014, Sequence-Stratigraphic Framework and Characterization of the Woodford Shale on the Southern Cherokee Platform of Central Oklahoma: Master's thesis, University of Oklahoma, Norman, Oklahoma, 210 p.

Montgomery, S.L., 1998, The Permian Bone Spring Formation, Delaware Basin: Petroleum Frontiers, v. 14.3, p. 1-89.

Montgomery, S.L., 1997, Permian Bone Spring Formation: Sandstone Play in the Delaware Basin Part I-Slope: AAPG Bulletin, v. 81.8, p. 1239-1258.

Montgomery, S.L., 1997, Permian Bone Spring Formation: Sandstone Play in the Delaware Basin, Part II-Basin: AAPG Bulletin, v. 81.9, p. 1423-1434.

Nance, S. and H.D. Rowe, 2013, Chemostratigraphy of Mudrocks: Bone Spring Formation, Delaware Basin, West Texas: AAPG Search and Discovery #90163.

Nance, H.S. and H.D. Rowe, 2014, Nested Cyclicity in Mudrock Successions: Bone Spring Formation, Delaware Basin, West Texas: AAPG Search and Discovery #90189.

Parra-Galvis, Victor, John D. Pigott, and Kulwadee L. Pigott, 2009, Carbonate Turbidite Platform to Basin Floor Facies Tract of the Jamaican White Limestone, AAPG Denver 2009.

Pearce, T.J., B.M. Besly, D.S. Wray, and D.K. Wright, 1999, Chemostratigraphy: a method to improve interwell correlation in barren sequences – a case study using onshore Duckmantian/Stephanian sequences (West Midlands, U.K.): Sedimentary Geology, v. 124, p. 197-220.

Pigott, J.D., 2013, GEOL 5363: Carbonate Geology. Fall 2013. Unpublished Lecture Notes.

Pigott, J.D. and B.W. Bradley, 2014, Application of Production Decline Curve Analysis to Clastic Reservoir Facies Characterization Within a Sequence Stratigraphic Framework: Example – Frio Formation, South Texas: Gulf Coast Association of Geological Societies, v. 3, p. 111-134.

Pigott, Kulwadee L., Engel, Michael, and Philp, Richard P., 2005, High Resolution Carbon Isotope Stratigraphy:Separating Global Versus Local Effects on a Jurassic Carbonate Ramp of The U.S. Gulf Coast, AAPG International Conference and Exhibition, September 11-14, Paris, France.

Pigott, Kulwadee L., Philp, Richard P., Engel, Michael H., and Weaver, Barry A., 2004, Chemostratigraphy of the Upper Jurassic (Oxfordian) Carbonate Sequence of the Smackover Formation of Southwest Alabama, U.S.A., 32nd International Geological Congress, Florence, Italy.

Pigott, Kulwadee L., Pigott, John D., Engel, Michael H. Engel, and Philp, Richard P., 2007, High resolution chemical stratigraphy in carbonates: Oxfordian Smackover USA ramp proxy, in AAPG International Conference and Exhibition, November 18-21, 2007, Athens, Greece.

Riquier, L., Tribovillard, N., Averbuch, O., Joachimski, M. M., Racki, G., Devleeschouwer, X., & Riboulleau, A., 2005, Productivity and bottom water redox conditions at the Frasnian-Famennian boundary on both sides of the Eovariscan Belt: constraints from trace-element geochemistry Developments in Palaeontology and Stratigraphy (Vol. 20, pp. 199-224): Elsevier.

Roach, E., 2014, Inside Drillinginfos's Map Drawers #1: Permian Basin: <http://info.drillinginfo.com/inside-driliinginfos-map-drawers-1-permian-basin/> Accessed April 16, 2014.

Ross, C.A. and J.R.P. Ross, 1995, Permian Sequence Stratigraphy in P.A. Scholle, T.M. Peryt, and D.S. Ulmer-Scholle, eds., The Permian of Northern Pangea: Berlin: Springer-Verlag, v. 1, p. 98-113.

Ross, C.A. and J.R.P. Ross, 1994, Permian Sequence Stratigraphy and Fossil Zonation: Canadian Society of Petroleum Geologists, v. 17, p. 219-231.

Rowe, H., N. Hughes, and K. Robinson, 2012, The Quantification and Application of Handheld Energy-dispersive X-ray Fluorescence (ED-XRF) in Mudrock Chemostratigraphy and Geochemistry: Chemical Geology, v. 324-325, p. 122-131.

Ruppel, Stephen C., and W. Bruce Ward, 2013, Outcrop-based Characterization of the Leonardian Carbonate Platform in West Texas: Implications for Sequence-stratigraphic Styles in the Lower Permian: AAPG Bulletin, v. 97.2, p. 223-250.

Ruppel, S. C., and Jones, R. H., 2007, Chapter 10. Key role of outcrops and cores in carbonate reservoir characterization and modeling, Lower Permian Fullerton field, Permian Basin, United States, in Harris, P. M., and Weber, L. J., eds., Giant hydrocarbon reservoirs of the world: from rocks to reservoir characterization and modeling: AAPG Memoir/SEPM Special Publication, v.88, p. 355-394.

Sageman, B.B. and T.W. Lyons, 2004, Geochemistry of Fine-Grained Sediments and Sedimentary Rocks: Treatise on Geochemistry, v. 7, p. 115-158.

Saller, A.H., J.W. Barton, and R.E. Barton, 1989, Slope Sedimentation Associated with a Vertically Building Shelf, Bone Spring Formation, Mescalero Escarpe Field, Southeastern New Mexico: SEPM Special Publication, v. 44, p. 275-288.

Sarg, J. F., 1988, Carbonate Sequence Stratigraphy: SEPM Special Publication, v. 42, p. 155-181.

Sarg, J. F., J. R. Markello, and L. J. Weber, 1999, The Second-Order Cycle, Carbonate-Platform Growth, and Reservoir, Source, and Trap Prediction: SEPM Special Publication, v. 63, p. 11-34.

Shumaker, R.C., 1992, Paleozoic Structure of the Central Basin Uplift and Adjacent Delaware Basin, West Texas: AAPG Bulletin, v. 76.11, p. 1804-1824.

Silver, B.A. and R.G. Todd, 1969, Permian Cyclic Strata, Northern Midland and Delaware Basins, West Texas and Southeastern New Mexico: AAPG Bulletin, v. 53.11, p. 2223-2251.

Slatt, R.M., 2013 GEOL 5970: Reservoir Characterization I. Fall 2013. Unpublished Lecture Notes.

Slatt, R. M., 2006, Stratigraphic Reservoir Characterization for Petroleum Geologists, Geophysicists, and Engineers, v. 10, Elsevier.

Slatt, R.M., 1974, Geochemistry of Bottom Sediments, Conception Bay, Southeastern Newfoundland: Canadian Journal of Earth Science, v.11, p. 768-784.

Sloss, L.L., 1963, Sequences in the Cratonic Interior of North America: Geological Society of America Bulletin, v. 74.2, p. 93-113.

Sloss, L.L., 1988, Chapter 3: Tectonic Evolution of the Craton in Phaerozoic Time, in L.L. Sloss, ed., Sedimentary Cover – North American Craton: U.S.: The Geology of North America: The Geological Society of America, p. 25-41.

Smith, C.N., and A. Malicse, 2010, Rapid Handheld X-ray Fluorescence (HHXRF) Analysis of Gas Shales: AAPG Search and Discovery #90108.

Tinker, S.W., 1998, Shelf-to-Basin Facies Distributions and Sequence Stratigraphy of a Steep-Rimmed Carbonate Margin: Capitan Depositional System, McKittrick Canyon, New Mexico and Texas: Journal of Sedimentary Research, v. 68.6, p. 1146-1174.

Treanton, J. A., 2014, Outcrop-derived Chemostratigraphy of the Woodford Shale, Murray County, Oklahoma: Master's thesis, University of Oklahoma, Norman, Oklahoma, 83 p.

Turner, B.W., J.A. Treanton, and R.M. Slatt, 2014, Applying Regional Chemostratigraphic Variability to Refine Sequence Stratigraphic Frameworks within the Woodford Shale, Oklahoma: Houston Geological Society Applied Geoscience Conference (Mudrocks).

Tribovillard, N., T.J. Algeo, T. Lyons, A. Riboulleau, 2006, Trace metals as paleoredox and paleoproductivity proxies: An Update: Chemical Geology, v. 232, p. 12-32.

Van Wagoner, J. C., R. M. Mitchum, K. M. Campion, and V. D. Rahmanian, 1990, Siliciclastic Sequence Stratigraphy in Well Logs, Cores, and Outcrops: Concepts for High-Resolution Correlation of Time and Faceis: AAPG Methods in Exploration Series, v. 7 p. 1-76.

Veevers, J. J., and C.M. Powell, 1987, Late Paleozoic Glacial Episodes in Gondwanaland Reflected in Transgressive-regressive Depositional Sequences in Euramerica: Geological Society of America Bulletin, v. 98.4, p. 475-487.

Wiggins, W.D. and P.M. Harris, 1985, Burial Diagenetic Sequence in Deep-Water Allochthonous Dolomites, Permian Bone Spring Formation, Southeast New Mexico: The Society of Economic Paleontologists and Mineralogists, v. CW 6, p. 140-173.

Winkler, S., and Matthews, J., 2014, Comparison of Electronic and Mechanical Schmidt Hammers in the Context of Exposure-Age Dating: Are Q and R Values Interconvertible?: British Society of Geomorphology v. 39, p. 1128-1136

Xu, C., 2018, High-Resolution XRF-LIDAR Sequence Stratigraphy of the Late Guadeloupian Capitan Slope at McKittrick Canyon, Texas: Process-Response of Oscillating Delaware Basin Sea Level: Master's thesis, University of Oklahoma, Norman, Oklahoma, 88 p.

Yang, K.M. and S.L. Dorobek, 1995, The Permian Basin of West Texas and New Mexico: Tectonic History of a "Composite" Foreland Basin and Its Effects on Stratigraphic Development: SEPM Special Publication, v. 52, p. 149-174

Ye, Q. and C. Kerans, 1996, Reconstructing Permian Eustacy from 2-D Backstripping and its Use in Forward Models; Lower and middle Guadalupian facies, Stratigraphy, and reservoir geometris; San Andres/Grayburg formations, Guadalupe Mountains, New Mexico and Texas. Moore, G. E. and Wilde, G. L. eds.; Sarg, J. F. (leader), Symposium and Guidebook-SEPM, Permian Basin Section 86-25; 69-74.

Yu, G., Hu, W., He, Z., Kui, X., Hu, H., He, L., Wang, T., Li, P., 2015, Complex resistivity characteristics of high TOC marine shale core samples and its applications: SEG Technical Program Expanded Abstracts 2014: p. 2964-2968.

Zhou, Y., 2014, High Resolution Spectral Gamma Ray Sequence Stratigraphy of Shelf Edge to Basin Floor Upper Capitan Permian Carbonates, Guadalupe Mountains, Texas and Delaware Basin, New Mexico: Master's thesis, University of Oklahoma, Norman, Oklahoma, 131 p.

Appendix A: Sloss's Sequences of North America

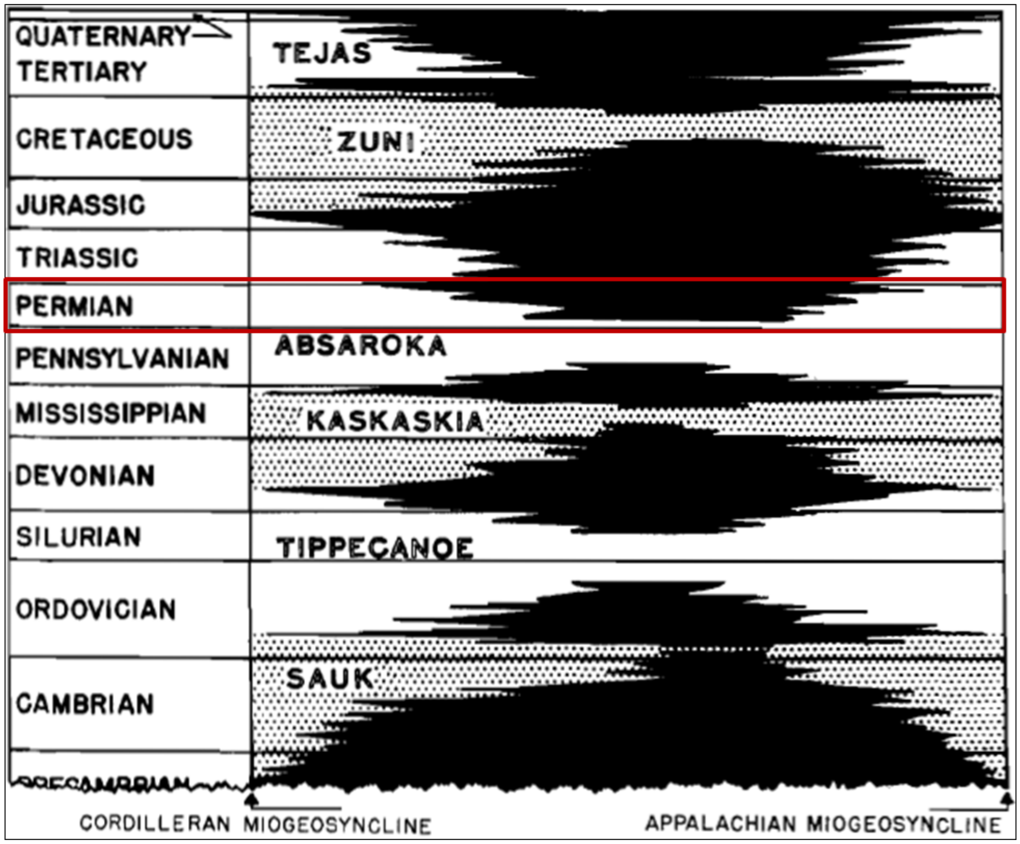

Sloss, 1963